Structures Behind the Spectacle: A Review of Optical Effects in Phenomenal Gemstones and Their Underlying Nanotextures

Shiyun Jin, Nathan D. Renfro, Aaron C. Palke, and James E. Shigley

This article reviews all of the special optical effects of gemstones, including opalescence, chatoyancy, asterism, schiller, and iridescence. The physics of light scattering, reflection, diffraction, and interference is briefly described for qualitative explanations of these optical phenomena. The most up-to-date microscopic investigations of the submicron inclusions and nanotextures in each type of phenomenal stone, along with their mechanistic interpretations, are also summarized. Although the basic principles behind these phenomena are generally understood, quantitative descriptions that directly connect the optical effects and the submicron structures are still lacking for many of these stones. In addition, the formation mechanisms of some of the textures in phenomenal stones are still debated, if not completely elusive.

This article roughly sorts the optical effects by the dimensionality and complexity of their underlying submicron structures and textures. Zero-dimensional nanoparticles in diamond and corundum, though typically not considered phenomenal gemstones, produce milky or opalescent appearances by scattering light randomly; one-dimensional oriented needle-like inclusions in chrysoberyl and garnet create cat's-eye and star effects; two-dimensional platelets and layers in feldspar produce schiller and iridescence by reflection and interference; and three-dimensional photonic crystals in precious opal cause brilliant play-of-color by Laue and Bragg diffraction. The often-confusing past uses of the phenomenal terminology in the literature are also clarified in this article.

A gem lover might think that all gemstones are phenomenal by definition. However, the term *phenomenal gemstones* designates a specific group of gem materials that display special optical phenomena under certain lighting or viewing conditions (Shipley, 1945), such as iridescence, schiller, and asterism (figure 1). These gems exhibit a wide range of visual effects created by different internal structures of various sizes and shapes, from diffuse scattering of light by randomly oriented particles to highly directional light reflection or diffraction from aligned or periodic textures. These phenomena can dramatically increase the value of an already valuable stone or even promote an otherwise common mineral into the gemstone category. Phenomenal gemstones substantially diversify the appearances of gemstones beyond the stereotypical sparkling crystals with attractive colors.

The optical effects of phenomenal gemstones reflect fine-scale structures and textures that interact with visible light in intricate ways, and they have drawn the attention of scientists for centuries. However, despite investigations by renowned scientists including David Brewster, C.V. Raman, and Robert Strutt, there is much that we do not understand about phenomenal gemstones, mainly due to the exceptionally small scales of the textures that create the phenomena. Most structures in phenomenal gemstones are internal (unlike the surface coloring structures in the animal kingdom, such as

See end of article for About the Authors and Acknowledgments.
Gems & Gemology, Vol. 61, No. 2, pp. 110–170,
http://dx.doi.org/10.5741/GEMS.61.2.110

Figure 1. A variety of some of the most common phenomenal gemstones. Top row, left to right: 2.35 ct 12-rayed star sapphire from Sri Lanka, gift of Gordon Bleck, GIA Museum no. 17037; 18.18 ct blue star sapphire, courtesy of Evan Caplan; 18.29 ct star ruby from Myanmar, courtesy of the Natural History Museum of Los Angeles County; 36.76 ct cat's-eye tourmaline from Brazil, courtesy of Pala International. Bottom row, left to right: 7.60 ct moonstone from Sri Lanka; 11.0 ct Oregon sunstone displaying aventurescence over red and green bodycolors; 11.45 ct black opal from Australia displaying vibrant play-of-color; 30.82 ct Finnish labradorite cabochon from GIA's Dr. Edward J. Gübelin collection. Photos by Robert Weldon (six stones on the left) and Orasa Weldon (two stones on the right).

in butterfly wings and bird feathers) and require meticulous sample preparation before they can be studied by advanced imaging techniques such as electron microscopy. In addition, the extremely long geological timescales and complicated crystallization histories that are often required to create these convoluted structures make them challenging, if not impossible, to reproduce through laboratory synthesis.

Fortunately, studies of phenomenal gemstones have dramatically improved in recent decades, mainly due to the development of more advanced analytical techniques with increasing resolution and accessibility (box A). Professional support for these seemingly inconsequential research projects has historically been limited. However, recent studies have proven that the intricate structures are not only exciting to the curious mind, but they also contain important information regarding the geological processes that created them, which is critical to better understand the history of our planet. Moreover, as a flexible, durable, and environmentally friendly alternative to traditional pigments, colors caused by structural interference have attracted a lot of interest in photonics and material sciences due to their wide range of applications in paints, cosmetics, fabrics, color sensors, wearable electronics, and anti-counterfeiting technologies. A better understanding of the

In Brief

- Nanoscale textures and structures in gemstones can create special optical effects that significantly affect their appearances and appeal.
- The dimensionality of the nanotextures in gemstones can range from zero (nanoparticles) to three (photonic crystals), resulting in drastically different optical phenomena.
- The nanotextures can form by many different mechanisms, reflecting the extreme range of thermodynamic conditions exhibited by geological processes.

BOX A: ANALYTICAL TECHNIQUES FOR STUDYING PHENOMENAL GEMS

Some analytical techniques commonly used to study the structure of phenomenal stones will be repeatedly mentioned in this article, and it is not possible to fully explain how each one works. For simplicity, the abbreviations used in this article are listed here in order of relevance, along with a brief description of the information each method can provide regarding the analyzed material.

XRD: X-ray diffraction. Mainly used to identify crystalline phases by matching the measured diffraction pattern with known structures in a database. Can be used to refine the details of the crystal structure to reveal the atomic ordering state and the chemical composition of the studied mineral. Also can be used to directly determine the crystal structure of an unknown or new material.

SEM: Scanning electron microscopy. Can image submicron textures that cannot be resolved by an optical microscope, typically on a polished surface of a material. Image contrast reflects the chemical variations in the material. May also reveal textural contrasts on an etched or freshly broken surface.

TEM: Transmission electron microscopy. Can resolve nanoscale textures and even atomic-scale structures. Requires special sample preparation that slices the analyzed material into a very thin foil of less than 100 nm in thickness. Also can create an electron diffraction pattern that can be used to identify the phase and its crystallographic orientation.

EDS: Energy-dispersive X-ray spectroscopy (sometimes abbreviated as EDX). An instrumental component of SEM or TEM that collects the X-ray spectrum excited by a high-energy electron beam, which can be used to map the chemical composition of the material. Quantitative analysis is possible only using well-characterized reference materials.

EPMA: Electron probe microanalysis. Employs the excited X-ray spectrum as in EDS, but with much better precision for quantitative chemical analysis. Well-characterized standard materials are required for quantification.

EBSD: Electron backscatter diffraction. An instrumental component of SEM that collects electron diffraction patterns in the backscattered direction, which can be used to identify the crystalline phases and their relative crystallographic orientations. Has much lower resolution compared to the electron diffraction in TEM but can be used to map a much larger area of a sample for statistical analysis. A database of known material structures is required to match the data for phase identification and orientation determination.

AFM: Atomic force microscopy. Can resolve the surface texture of a material at the nanoscale by scanning the surface with a tiny mechanical probe. The image may look similar to an SEM image, but it contains quantitative information of the surface height, which cannot be acquired from SEM.

APT: Atom probe tomography. A method that can create three-dimensional elemental maps with nanometer resolution, revealing the size, shape, and distribution of tiny clusters, precipitates, or lamellar textures that are smaller than 100 nm. Often used as a complement to TEM.

FIB: Focused ion beam. A method that probes the sample using a high-energy beam of atomic ions (most commonly gallium ions). One of the most important applications of FIB is to prepare TEM and APT samples due to its ability to precisely cut the exact region of interest from the analyzed specimen. The secondary electrons created by FIB can also be used for imaging (similar to SEM), while the secondary ions can be analyzed by mass spectrometry.

submicron structures of minerals may help push the design and manufacture of these colorful materials beyond biomimicry.

Because of the sophistication of these recent studies, the knowledge gap between the gemology world and mineralogy and physics research is widening faster than ever. It is challenging for gemologists and gem consumers to stay current with the latest updates in the scientific literature, which may be filled with jargon and target only a few experts in their respective fields. Certain inaccurate descriptions and incorrect explanations of phenomenal gemstones from outdated publications are sometimes still cited in recent gemological literature. The new studies cannot be blindly trusted either, as many of them have not yet stood the test of time. Speculation without sufficient supporting evidence is another source of misinformation and confusion, with researchers still struggling to draw solid conclusions. Even experts sometimes fall victim to misinformation, and it is not uncommon to find mislabeled specimens of phenomenal gemstones in famous gem and mineral museums. Misinterpretation of data acquired using advanced techniques is also quite common, as they often exist in abstract and potentially misleading formats that require

Box B: Glossary

The terms used to describe the optical effects of gemstones are defined below, with the relationships among some of them illustrated in figure B-1. Note that the definitions provided here are closely linked to the underlying textures that create these effects, which is why they may seem different from the definitions found in other sources. Many of the previous definitions of these phenomenal terms are subjective descriptions of their appearances, which often lead to misusage and confusion.

Iridescence: Structural color(s) created by interference of reflected or diffracted light by submicron structures. Primarily used for prismatic colors but can be expanded to desaturated or even whitish colors to emphasize their interference origin (e.g., iridescence of moonstone). The term *iridescent color(s)* is used only for more saturated prismatic-colored iridescence.

Play-of-color: Iridescent colors created by diffraction that change (typically in the sequence of prismatic colors) when the stone is rotated relative to the light source or observing eye.

Schiller: A sudden strong reflection of light from within a crystal as it rotates relative to the light source and observing eye, caused by oriented platy inclusions or lamellar textures. Sometimes accompanied by iridescence from thin-film or multilayer interference.

Sheen: Similar to schiller but much less frequently used. Sheen may describe a schiller that is slightly diffuse or originates close to the surface.

Adularescence: Iridescent sheen of alkali feldspar (i.e., moonstone). Occurs primarily as a desaturated blue but sometimes light yellow or white, with a billowy, floating appearance resembling moonlight. This term is misleading as adularescence is not observed in adularia (a variety of potassium-rich feldspar).

Labradorescence: Iridescent schiller seen in plagioclase feldspar labradorite from plutonic rocks.

Peristerescence: Iridescent schiller of peristerite (sodium-rich plagioclase feldspar).

Aventurescence: Specular reflection from isolated, visually discernible flat interfaces (platy or thin-film inclusions, fractures, or facets of euhedral crystal inclusions) inside transparent minerals. Originally called "aventurization," a now obsolete term. Most aventurescence is caused by oriented inclusions and appears as a schiller effect.

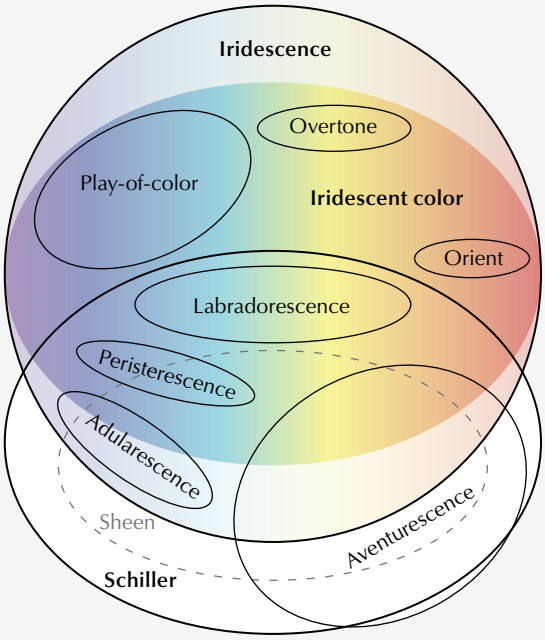

Figure B-1. Venn diagram showing the complicated relationships among the terms describing reflection- and interference-related optical phenomena in gemstones. Note that the overlaps among different terms indicate that they are not exclusive from one another, which means the same phenomena can often be described by several different terms.

Opalescence: Milky or hazy appearance of a mineral or gem material created by diffuse scattering of light by nanoparticles, such as that observed in common opal. This term is sometimes used colloquially to refer to the play-of-color of precious opal.

Chatoyancy/"Cat's-eye": A narrow band or thin line of reflected light on a cabochon-cut gemstone that moves as the stone rotates relative to the light source, created by parallel needle inclusions or fibrous textures. The term is named for the effect's resemblance to the slit-shaped pupil of a cat's eye.

Asterism/"Star": Two or more chatoyant bands on a cabochon-cut gemstone that intersect at a single point to create a star-like shape, created by parallel needle inclusions along different directions. The number of rays of the star can range from 4 to 12.

Overtone: Single-color iridescence over the bodycolor of a nacreous pearl.

Orient: Multicolor iridescence over the bodycolor of a nacreous pearl.

The definitions of some terms related to crystal intergrowth of minerals are listed below. Many of these terms have a long history in mineralogy, but are not always clearly defined. Therefore, it is useful, even for experts familiar with the field, to clarify some of the subtleties and ambiguities of the terms before they are repeatedly used in this article.

Inclusion: A foreign material enclosed within a host mineral. Can be of any size or shape. Common types include mineral inclusions (crystals of different minerals), fluid inclusions (liquid and gaseous), and melt inclusions (solidified magmatic melt). Can be materials trapped during crystal growth of the host mineral (primary inclusions) or formed after the crystal stopped growing (secondary inclusions).

Exsolution: Unmixing of an initially homogeneous solid solution into two or more separated phases. If the crystal structures of the exsolved phases are similar, the intergrowth often has a lamellar texture, sometimes periodic or quasiperiodic, known as exsolution lamellae. Some argue that by definition, exsolution should be restricted to a chemically closed system, which means it can be caused only by temperature or pressure change. Nonetheless, phase separation due to change in oxidation state is often referred to as exsolution as well.

Precipitation: A special case of exsolution in which the minor phase, formed through nucleation and growth, makes up only a small fraction of the system, resulting in a suspension (or colloid) of small inclusions sprinkled in a continuous matrix of the dominant phase. The term is borrowed from the similar processes in aqueous chemistry and metallurgy, but the liquid solutions are replaced by mineral solid solutions. The inclusions created by precipitation are called precipitates, which are typically simple oxides or native elements.

Epitaxy: Growth of one mineral on the crystal face (or cleavage plane) of another mineral in an orderly manner, such that certain crystallographic directions of the two minerals are aligned at the interface. Requires the two minerals to have similar atomic arrangements on the two-dimensional plane they share (low degree of lattice mismatch). The interface for epitactic[1] growth is either coherent (the lattices of the two minerals perfectly match one another) or semi-coherent (the lattices mostly match but with periodic dislocations).

Crystallographic orientation relation (COR): When two crystals grow next to each other, they are often oriented in a special way relative to one another, usually due to coherency constraints at the interface. This relative orientation is described by the crystallographic orientation relation (COR).[2] Depending on the symmetry of the two phases, there may be more than one way to describe the COR. Exsolution and epitactic growth can both create special CORs between two different phases.

Twinning: Two single crystals of the same phase growing into one another following a special COR. The specific COR describing a twinning intergrowth is known as a twin law. Twin laws are often named after the locality they were originally reported from (e.g., Brazil law, Carlsbad law) or the minerals that most commonly display them (e.g., Albite law, Spinel law). Note that the name of a twin law is always capitalized to avoid confusion (e.g., Albite-twinned anorthite, Spinel-twinned magnetite). Also note that a twin law always describes the relation between two single crystals in direct contact with each other. However, one single crystal may have twin relations with multiple other single crystals, resulting in repetitive twinning within the same specimen, such as polysynthetic (parallel boundaries) or cyclic (nonparallel boundaries) twins.

[1] "Epitactic" (or "epitaxic") is the accepted adjective in the mineralogy field (Bailey, 1977), even though "epitaxial" appears to be more commonly used in other fields.

[2] COR is typically described in the form $\{h_1k_1l_1\}_\alpha /\!/ \{h_2k_2l_2\}_\beta + \langle u_1v_1w_1\rangle_\alpha /\!/ \langle u_2v_2w_2\rangle_\beta$, where $h_1k_1l_1$ and $h_2k_2l_2$ are the lattice planes of the two crystals at the interface and $u_1v_1w_1$ and $u_2v_2w_2$ are matching lattice directions within the $h_1k_1l_1$ and $h_2k_2l_2$ lattice planes, respectively.

special expertise for proper processing and interpretation. Finally, the situation is further complicated by often subjective descriptions of the phenomena in gemstones, resulting in poorly defined terminology that is often misused. Different optical effects sometimes look similar, and the same effect may appear dissimilar in different specimens. Multiple phenomena can also occur in the same gemstone, sometimes at different orientations or on different surfaces. A glossary of optical phenomena in gemstones, along with some terms related to crystal intergrowth, is provided in box B in an attempt to clarify the often-confusing terminology.

With this comprehensive review of the status of scientific investigations into optical processes and submicron textures in phenomenal gemstones, the

BOX C: INTERACTION BETWEEN LIGHT AND SMALL PARTICLES

Visible light contains electromagnetic waves with wavelengths between approximately 400 and 700 nm. When light is intercepted by an object, it may be reflected, refracted, and/or absorbed. These interactions can modulate the intensity of specific wavelengths and redirect them to our eyes, allowing us to see the colorful world around us. The interaction between light and macroscopic objects can be described by relatively simple mathematical equations such as Snell's law and the Fresnel equations, using only the refractive indices of the materials involved. However, when an object is smaller than the wavelength of the light, the laws of reflection and refraction in geometrical optics stop working, as the light behaves more like a coherent wave instead of independent rays. In order to accurately compute the optical effects of small particles, light must be described using the more fundamental Maxwell's equations.

The process of light randomly bouncing off small particles is generally called "scattering." Unlike reflection or refraction, in which the direction of light is fixed by the incident direction relative to the interface (incident angle), light scattering is a more random process that can only be described by a probability distribution. In the simplest case, light scattering is modeled by particles that are spherical (the highest possible symmetry in three-dimensional space), as was solved analytically by Gustav Mie (1908) more than a century ago. For particle sizes (with diameter d) much smaller than the wavelength (λ) of light, Mie scattering can be approximated by the Rayleigh scattering equation (Bohren and Huffman, 1998):

$$I = I_0 \frac{1+\cos^2\theta}{2R^2} \left(\frac{2\pi}{\lambda}\right)^4 \left(\frac{n^2-1}{n^2+2}\right)^2 \left(\frac{d}{2}\right)^6 \quad \text{(C-1)}$$

where I is the intensity of the scattered radiation, I_0 is the intensity before interaction with the particle, R is the distance to the particle, θ is the scattering angle, and n is the refractive index (RI) of the scattering particle relative to the surrounding medium. Note that the Rayleigh approximation applies only to very small particles ($d/\lambda<0.1$), and the larger the particle size, the larger the error of the approximation. It also applies only to non-absorbing particles, of which the relative RI is a real number (because the RI of an absorbing/opaque material is a complex number). The equation shows that the further n (relative RI) deviates from 1 (the larger the RI difference between the scattering particle and the surrounding matrix), the stronger the scattering intensity. The scattering intensity is proportional to the sixth power of the particle diameter (d^6 in equation C-1), which means that larger particles are much more efficient at scattering light than smaller particles. For instance, the scattering intensity from a 20 nm particle is 64 times that of a 10 nm particle, even though the volume is only 8 times larger. The scattering intensity is also proportional to $1/\lambda^4$, meaning that blue and violet light with shorter wavelengths is scattered much more intensely than red and orange light with longer wavelengths. The blue color of the sky is created by Rayleigh scattering from molecules in Earth's atmosphere. It is speculated that Rayleigh scattering from small particles in gemstones can contribute to blue hues, but there has been no direct experimental evidence suggesting that this effect is observable at such small scales.

A dispersion system containing evenly distributed particles smaller than a few hundred nanometers is called a colloid, so nanoparticles are sometimes called colloidal particles. Because colloidal particles scatter visible light randomly, they cannot be directly observed using even the best optical microscope. However, the scattering effect from these small particles, called the Tyndall effect, creates a hazy translucent appearance that distinguishes a colloid from a solution. Nanoparticle inclusions can sometimes be found in minerals and gemstones, and they can create a unique aesthetic different from that of gemstones with high clarity. These colloid gemstones are typically not considered phenomenal gemstones, but the special optical effects they display justify their inclusion in this article. This also sets a foundation for understanding some of the most complicated optical phenomena. The study of optical properties of colloid systems has been a very important subject in physics for over a century, mainly due to their significant applications in chemistry, biology, material optics, atmospheric and environmental science, oceanography, remote sensing, and astronomy. Related developments in optical theory and computational methods have allowed us to better understand the optical effects of some mineral colloids and colloid gemstones.

authors hope to clear up some of the confusion and misinformation. This article may also offer guidance for future investigations into optical phenomena in gemstones by providing a summary of what we understand so far and what is still unknown. In this review, the optical processes are only qualitatively explained, with a few necessary mathematical equations, which should be sufficient for a basic understanding. Although some rudimentary knowledge of crystallography and thermodynamics of solid solutions may be required to fully understand every detail, we hope the general concepts are still accessible to anyone who is

Figure 2. A: Green, yellow, brown, and white Brazilian opals; courtesy of Cody Opal. B: Mexican opals showing ranges of color and clarity. C: Faceted fire opals with red (13.51 ct, Mexico), orange (3.14 ct, Mexico), and yellow (8.80 ct, United States) colors. D: Pink and blue Peruvian opal; courtesy of Hussain Rezayee, Rare Gem Co. E: Purple Mexican opals colored by fluorite inclusions (116 and 130 g rough pieces with 13.98 and 15.24 ct cabochons). F: A 10.22 ct prase opal cabochon from Central Tanzania; gift of Lithos Africa. Photos by Robert Weldon (A, C, and D), Tino Hammid (B), and C.D. Mengason (E and F).

interested in this subject. This review is also intended as a starting point for those who seek to expand their knowledge of the topic, as most of the relevant literature is referenced in this article.

This article is structured by roughly sorting the different phenomenal gemstones by the increasing dimensionality and complexity of their underlying submicron structures and textures, as outlined by the physical principles explained in boxes C–F. However, we resisted the temptation to firmly separate the phenomenal gemstones into distinct categories because the boundaries between different effects are not as distinct as most would expect (e.g., chatoyancy versus aventurescence). Moreover, many of the descriptions of optical phenomena are qualitative at best, if not outright ambiguous. This article's order is intended to optimize the logical flow for the reader. For example, the iridescence of pearl and shell is produced primarily by multilayer interference similar to that in labradorite, yet they are discussed last, along with other gemstones that exhibit effects based on diffraction, because the concept of diffraction must be explained first for the reader to appreciate the historical debates regarding the role of diffraction gratings on the surfaces of shells. Also, common opal and precious opal have similar submicron structures but are discussed separately (at the beginning and near the end, respectively) due to their dramatically different visual appearances and optical effects.

COMMON OPAL

Opal (Opl: $SiO_2 \cdot nH_2O$) is a silica mineral containing a variable amount of water. Although it is considered a valid mineral name by the International Mineralogical Association (IMA) for historical reasons, opal does not fit the technical definition of a mineral and is commonly described as a mineraloid because it is not ordered at the atomic scale. As determined by X-ray diffraction (XRD) patterns, opals are generally classified into three groups of increasing order: opal-A (amorphous silica), opal-CT (poorly ordered intergrowths of cristobalite and tridymite with amorphous silica), and opal-C (poorly ordered cristobalite with amorphous silica), with many samples showing transitional characteristics between these end members (Curtis et al., 2019). Opal-A can be further divided into opal-AG (amorphous gel, composed of amorphous silica spheres) and opal-AN (amorphous network, also known as hyalite) based on their submicron textures. In general, opals form when meteoric and ground waters dissolve silica from igneous or sedimentary rocks and reprecipitate it within fissures of host rocks (Gaillou et al., 2008). The detailed processes controlling the texture and crystallinity of opal are still not fully understood (Gaillou, 2015), although different models have been proposed and tested (Brown, 2005). A recent study synthesized a material with similar composition and grain sizes to natural opal-AG under geologically relevant conditions (Gouzy et al., 2024). Because opal typically forms at low temperatures, kinetics rather than thermodynamics controls the precipitation process, and opals from different localities can have dramatically variable appearances as a result of diverse chemistries and nanostructures. Opals with no play-of-color are generally called "common opals," which may also serve as gemstones due to their unique milky appearance (box C) and vibrant colors (figure 2).

Common opals may be considered the paradigm of colloid gemstones, as they consist almost entirely of nano-size silica spheres (figure 3; Gaillou et al., 2008), with the exception of opal-AN. The scattering of light from the randomly arranged nanospheres

Figure 3. SEM images showing the silica spheres in common opal. Instead of solid concentric spheres (A and B), opal-CT and opal-C may contain lepispheres (spherical aggregates of blades, C). The spheres in common opal scatter light completely randomly due to the irregular arrangement, creating the typical milky appearance. The sizes of the silica spheres in common opal may cover a wide range (A) or be very similar to each other (B and C). Image A from Gaillou (2015) and B and C from Gaillou et al. (2008).

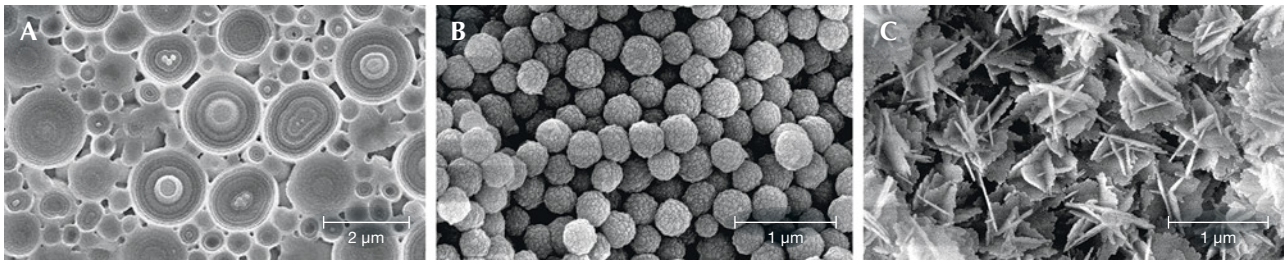

gives common opal a hazy appearance (figure 2). In fact, the word *opalescent* is sometimes used to describe the hazy or milky appearance found in other gemstones containing nano-inclusions, such as fancy white diamonds (Eaton-Magaña et al., 2019).

The bodycolor of common opal is mainly controlled by the species of nano-inclusions. For instance, hematite inclusions create yellow, orange, or brown colors; fluorite inclusions can produce purple; and green opals may contain nickel-rich inclusions. The sky-blue color in some opals may be created by scattering, as they appear orange in strong transmitted light (Gaillou, 2015). It is highly debatable, however, whether this is Rayleigh scattering, because most of the nanospheres in opal are too large to scatter visible light (box C). Careful quantitative analysis of the scattered and transmitted spectrum will be necessary to accurately describe the effect (Kinoshita, 2008). Photoluminescence created by uranium (green), unsaturated silica frameworks (blue), or organic compounds (orange) may also affect the apparent color of opal under sunlight, if it is not quenched by high concentrations of iron (Gaillou, 2015).

FANCY WHITE AND FANCY BLACK DIAMOND

Among all milky and cloudy gemstones, fancy white and fancy black diamonds are perhaps the most valuable (figure 4). Although it is debated whether white and black are considered colors or not, these special diamonds are graded and reported similarly to other fancy-color diamonds. Therefore, they are generally not considered phenomenal gems even though their "colors" are caused by special optical effects. The gemological properties of both natural fancy white and fancy black diamonds are best summarized by Eaton-Magaña et al. (2019).

Fancy white diamonds owe their hazy or cloudy appearance to dislocation loops and nano-inclusions (Gu and Wang, 2018; Gu et al., 2019). A dislocation is a linear crystallographic defect within the crystal structure where the atomic arrangement changes abruptly. Dislocations in diamond almost always exist as self-enclosed loops due to their localization and lower energy. Experiments at very high temperatures have shown that dislocation loops can form from platelet defects (planar or film defects containing aggregated nitrogen) in type IaB diamonds (Evans et al., 1995; Speich et al., 2017), and a similar process is believed to be responsible for dislocation loops in untreated natural diamonds. Because dislocations are one-dimensional misalignments of atoms in the crystal structure, they fall well below the imaging resolution of an optical microscope (figure 5A). However, they can still scatter light to create the hazy appearance due to the disrupted crystal lattice as well as the strain field around it.

The nano-inclusions found in fancy white diamonds are octahedral-shaped negative crystals, known as voidites, which are approximately 30 to 200 nm in size and contain nitrogen (Barry et al., 1987). These voidites are believed to have formed

Figure 4. Faceted fancy white and fancy black diamonds with different degrees of transparency. Photos by GIA staff.

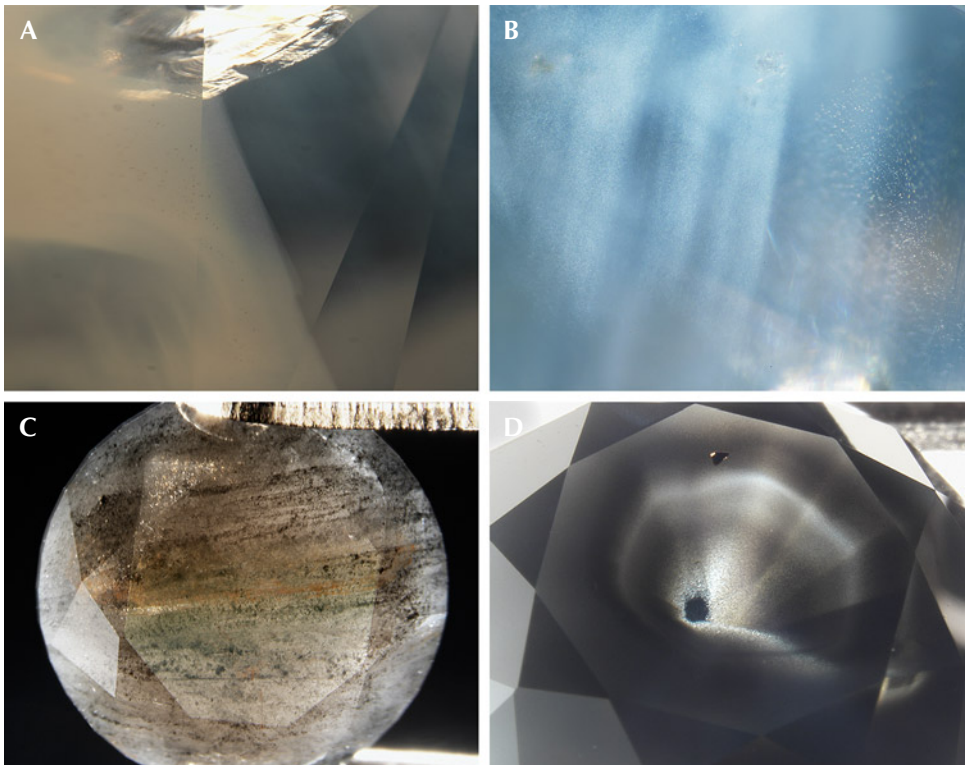

Figure 5. Cloudy regions in fancy white diamonds (top) and dark-colored particle and cloud inclusions in fancy black diamonds (bottom). Photomicrographs by Garrett McElhenny (A) and GIA staff (B–D); fields of view 2.3 mm (A), 1.6 mm (B), 6.7 mm (C), and 6.9 mm (D).

by the exsolution of excess nitrogen from the diamond lattice (Kiflawi and Bruley, 2000), and they contain mostly solid molecular nitrogen (cubic δ-N_2) (Navon et al., 2017; Sobolev et al., 2019; Tschauner et al., 2022). A recent study also showed that oxygen atoms dissolved within the diamond lattice can also exsolve to form voidites filled with CO_2 (Shiryaev et al., 2023). Unlike dislocation loops, voidite inclusions are three-dimensional particles, which can be seen as "pinpoints" under high magnification using an optical microscope (the size falls below the resolution of the optical microscope, so they appear as dots) (figure 5B).

Nitrogen defects in diamond crystals start as isolated single nitrogen atoms substituting for carbon atoms (C centers), which can coalesce into pairs (A centers) and eventually four-nitrogen clusters (B centers) over geological time (Boyd et al., 1995). Both dislocation loops and voidites in fancy white diamonds are strongly related to the aggregated nitrogen defects, which are produced by high concentrations of nitrogen impurities and prolonged annealing at high temperature. Therefore, fancy white diamonds are predominantly type IaB (diamonds old enough to contain only B centers), and they originate from Earth's transition zone or the lower mantle. Because these aggregates form by annealing, no thermal treatment to mimic or enhance the cloudy or hazy appearance of fancy white diamonds has been reported.

The cause of color in natural fancy black diamonds is more complicated, involving dark-colored inclusions such as graphite or iron oxide (hematite and magnetite), radiation stains, or a high density of absorption defects. Most inclusions in fancy black diamonds are much larger than the voidites in fancy white diamonds and are likely incorporated during rapid growth of the diamond crystal (figure 5, C and D). Unlike fancy white diamonds, the fancy black color can be created in diamonds by several different treatment methods, including heating at high temperatures under vacuum or heavy irradiation treatment. In fact, more than one-third of the black diamonds examined by GIA have been treated.

COPPER-COLORED PLAGIOCLASE FELDSPAR

The U.S. state of Oregon is the only confirmed source of natural copper-colored gem feldspar. Ethiopia has been reported as a newer source, which is likely valid given the stones' consistently different chemistry from that of the Oregon material (Kiefert et al., 2019; Sun et al., 2020), but international gemological researchers have not yet visited the deposit to verify its authenticity. All the gem basaltic feldspars

from Oregon are sold as "Oregon sunstone" in the gem market, even though not all show aventurescence (figure 6).

Spherical colloidal copper is known to imbue a host material with hues of red, a technique used for centuries to make red glass (Durán et al., 1984; Freestone, 1987; Freestone et al., 2007). The less common green color of Oregon sunstone, however, has long remained an enigma to mineralogists. Metallic copper is electrically conductive and interacts with light quite differently compared to dielectric (insulating) particles, and therefore the interaction cannot be simply approximated with Rayleigh scattering. The free electrons in a copper nanoparticle could resonate with light of certain wavelengths and absorb its energy. These oscillating charges also create a strong electric field on the particle surface and enhance its scattering power. These complicated processes make the color of copper-bearing feldspars unique in the mineral world and challenging to study. Jin et al. (2022a) computed the absorption and scattering properties of spheroidal copper particles of various sizes and shapes embedded in feldspar, which validated the speculation by Hofmeister and Rossman (1983) that an anisotropic colloid is the cause of the strong pleochroism often observed in green-blue Oregon sunstone. The computation shows that the colloidal copper particles are strong and selective absorbers of visible light, and only a few parts per million by weight are sufficient to produce saturated colors in mostly transparent crystals.

The orientation of the copper particles in an Oregon sunstone from the Sunstone Butte mine, evidently controlled by the feldspar structure, has also been characterized in detail using polarized absorption spectroscopy (Jin et al., 2023). Interestingly, the transmission electron microscopy (TEM) analysis by Wang et al. (2025) revealed copper particles elongated along the [001] direction in a dichroic crystal from the same mine, instead of the [100] direction as shown by optical analysis (Jin et al., 2023), suggesting that the feldspar structure may not be the only factor determining the particle shape and orientation. Note that optical analysis reveals the average orientation of all the copper particles collectively, whereas TEM can show only the projection of individual particles one at a time. Wang et al. (2025) oriented the samples crystallographically instead of optically and thus missed the opportunity to correlate the two types of analyses in the same study. More correlated TEM and optical studies are needed to better understand the relationship between the particle shapes and the feldspar structure.

The low (triclinic) symmetry of feldspar leaves its optical orientation unconstrained by its crystallography, resulting in complicated interactions between the highly directional absorption and scattering effects of the copper particles and the anisotropic feldspar optics (Jin et al., 2023). This creates a wide range of possible appearances that are heavily dependent on lighting and viewing directions, presenting more challenges and opportunities for faceting Oregon sunstone than for any other pleochroic gem. Depending on the aspect ratio of the copper particles, Oregon sunstone could be the most pleochroic gem material of all, often showing drastically contrasting colors on different facets of the same stone.

Copper diffusion treatments have been shown to create red and green colors in otherwise colorless feldspar crystals (Emmett and Douthit, 2009; Zhou et al., 2021, 2022), a discovery made after a large amount of red feldspar, purportedly from Asia or Africa, flooded the gem market more than a decade ago, creating controversy in the gem trade regarding the origin and authenticity of these gemstones (Abduriyim, 2009; Abduriyim et al., 2011; Rossman, 2011). The treatment process proves that the particles form by precipitation of copper dissolved in the feldspar lattice. Diffused feldspars generally contain much higher copper concentrations than natural Oregon sunstone (Sun et al., 2020; Jin et al., 2023).

Figure 6. Rough Oregon sunstone from the Sunstone Butte mine showing a wide range of colors. Photo by Robert Weldon.

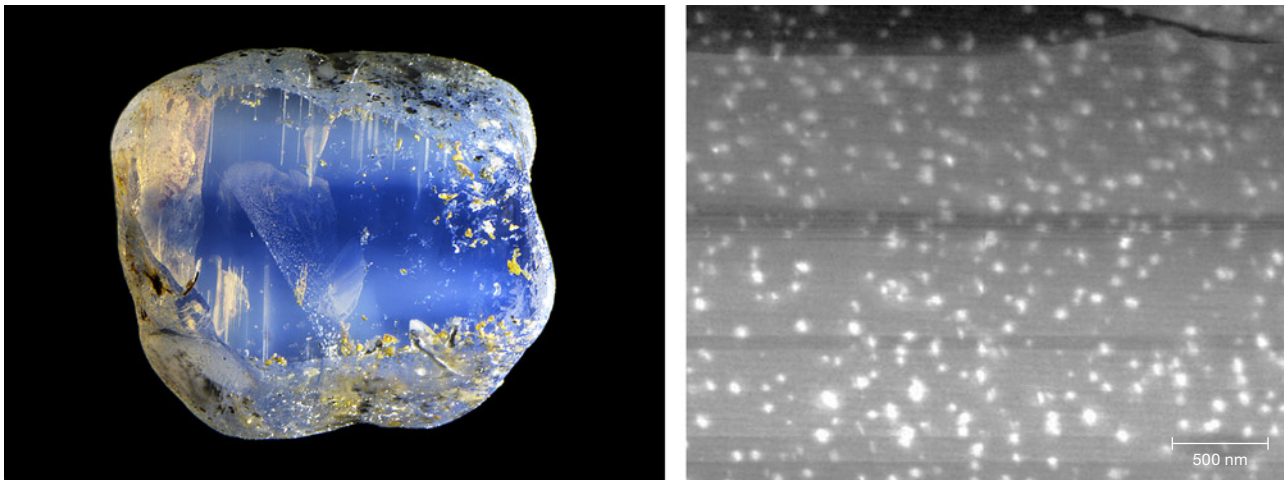

Figure 7. Left: A 1.25 ct sapphire from Ilakaka, Madagascar, containing cloudy areas correlated with higher concentrations of beryllium, niobium, and tantalum. Photo by Nathan Renfro. Right: A scanning TEM (high-angle annular darkfield) image of the cloudy area showing high-density titanium-rich nanoparticles with the riesite structure. The titanium oxide nanoparticles appear brighter than the corundum matrix. The horizontal stripes in the image are artifacts from sample preparation. Image from Shen (2011).

The size, shape, density, and zonation of the copper particles also appear noticeably different from diffused and untreated copper-colored feldspars as a result of different thermal histories (Jin et al., 2023). Natural Oregon sunstones typically show much stronger pleochroism than artificially diffused feldspars, likely due to the prolonged cooling in basaltic lava flows compared to the fast heating and cooling processes used in the laboratory.

MILKY SAPPHIRE AND RUBY

Corundum (Crn: α-Al_2O_3) is another gem mineral that can show a milky or cloudy appearance due to nanoscale particle inclusions. Although translucence generally does not increase the attractiveness or value of sapphire or ruby crystals, which ideally are transparent, internal light scattering is often used as a special characteristic to help determine provenance (Palke et al., 2019a,b). Thin milky bands that do not impair the transparency can create an admirable sleepy, velvety appearance, which is best shown in Kashmir sapphires. Some sapphires with a homogeneous milky appearance are marketed as "opalescent sapphires," which have increased in attraction and popularity in recent years. Most milky sapphires and rubies would display weak asterism if cut into cabochons, but they are more often faceted to enhance their visual transparency. Therefore, they are discussed separately from the star sapphires and rubies in this article due to their special appearance and mineralogy.

The included milky regions in natural corundum show a positive correlation with the titanium concentration, indicating that the nano-inclusions are most likely titanium-bearing phases. He et al. (2011) systematically studied the evolution of TiO_2 precipitates in synthetic titanium-doped sapphire, and their work supports several previous studies of synthetic or heated natural titanium-bearing corundum (Phillips et al., 1980; Jayaram, 1988; Moon and Phillips, 1991; Xiao et al., 1997). Titanium in sapphire would exsolve directly as rutile (Rt: α-TiO_2) at 1350°C or higher, yet riesite[1] is the initial precipitated phase when annealed at 1300°C or lower, transforming eventually to rutile as the precipitates grow larger.

Unfortunately, studies of nano- and micro-inclusions in natural corundum are relatively limited. Shen and Wirth (2012) confirmed the presence of natural riesite precipitates (20–40 nm long and 5–10 nm wide) in the cloudy region of a sapphire from Ilakaka, Madagascar (figure 7). Baldwin et al. (2017) observed high-density nanoparticles (~10–20 nm long) enriched in high field strength elements (HFSEs) in the cloudy brown region of a basaltic sapphire crystal from Petersberg, Germany. Contrary to the authors'

[1]Riesite is a high-pressure polymorph of TiO_2 with the scrutinyite (α-PbO_2) structure. The mineral name was coined only recently (Tschauner et al., 2020), even though the phase had already been known for decades; thus the nomenclature in the literature is often confusing. It has been referred to as srilankite (Ti, Zr oxide with the same structure), TiO_2-II, α-PbO_2-type TiO_2, and even α-TiO_2, the last of which is incorrect because α-TiO_2 is rutile.

interpretation, the preferred orientations and coherent boundaries shown in the TEM images of these nanoparticles are consistent with solid-state exsolution of HFSEs as riesite precipitates (Jin et al., 2024). Rutile inclusions in corundum crystals have been observed only with much larger sizes (at least 200 nm long) (Phillips et al., 1980; Moon and Phillips, 1991; Xiao et al., 1997; He et al., 2011). A recent atom probe tomography (APT) and TEM study reported an unknown phase of secondary beryllium-bearing nanoparticles (~10 nm) occurring together with riesite precipitates (~5 nm) in a Nigerian sapphire crystal containing high concentrations of heavy HFSEs and beryllium (Jin et al., 2024). A similar study of a Madagascar sapphire containing less beryllium showed only riesite precipitates (~20 nm), with beryllium concentrated at the boundary between the nanoparticles and the corundum matrix (Emori et al., 2024). Riesite is stable at pressures above 6 GPa (Olsen et al., 1999), which is much greater than the pressures associated with the growth conditions of most gem corundum (Giuliani et al., 2014). This suggests that all the riesite nano-inclusions in corundum form through solid-state exsolution, stabilized by the immense strain induced by the coherent boundary between riesite and corundum (Xiao et al., 1997; He et al., 2011).

Most (if not all) of these nano-inclusions in natural corundum contain titanium, which would dissolve into the corundum lattice under high-temperature heat treatment, turning the stones bluer due to the newly formed titanium-iron pairs. In fact, the milky or cloudy appearance is commonly used by gem miners and traders to determine whether natural corundum may be color enhanced by heat treatment, with the geuda-type sapphire from Sri Lanka the best-known example (Gunaratne, 1981; Ediriweera et al., 1989; Perera et al., 1991).

Submicron and nanoscale inclusions are quite common in natural materials, as suggested by the few studies on sapphire and feldspar. Even though most of the nano-inclusions are optically invisible and may not affect the appearance of minerals and gemstones, they are of great importance for geological research, as they contain detailed information about the mineral's geological history that cannot be retrieved otherwise. More careful TEM and APT analysis of natural corundum and other minerals is needed to fully understand the nature of these nano-inclusions. More unknown phases likely are waiting to be discovered as new mineral species in these nano-inclusions.

STAR SAPPHIRE AND RUBY

Star sapphire and ruby are certainly the most popular asteriated gemstones (box D) and probably the best-known of all phenomenal gemstones. The asterism in star sapphire and ruby is created by thin needle-shaped inclusions known as "silk" in the corundum host (figure 8). It has long been speculated that these silk inclusions are rutile needles. However, prior to

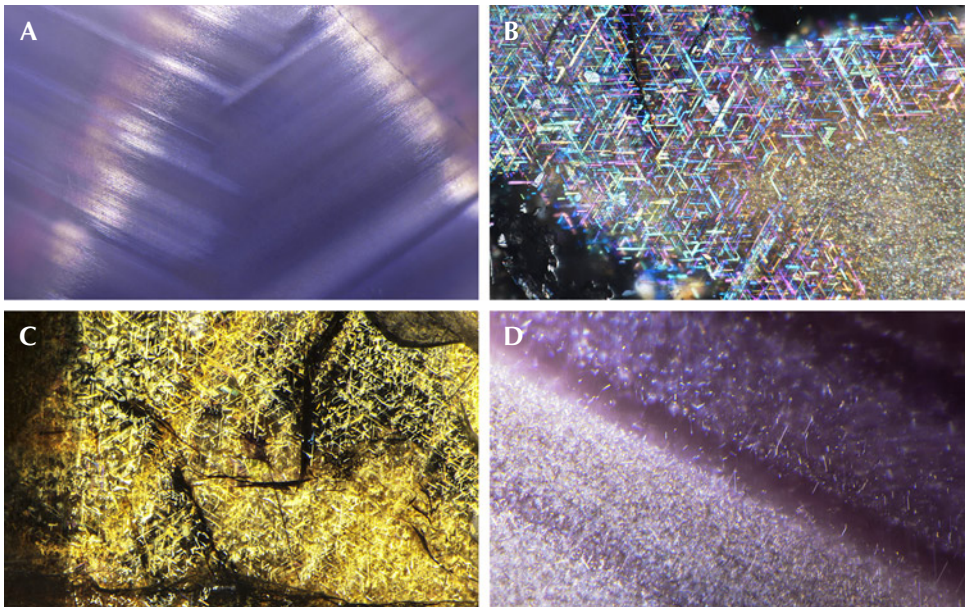

Figure 8. A: Fine rutile silk in a star sapphire. B: Rutile needles in a Burmese sapphire. C: Dense hematite and/or ilmenite needles in a sapphire from Kenya. D: Needle inclusions in a 12-rayed star sapphire. Photomicrographs by Nathan Renfro (A, C, and D) and Victoria Liliane Raynaud-Flattot (B); fields of view 4.62 mm (A), 0.97 mm (B), 2.44 mm (C), and 0.91 mm (D).

Box D: Scattering and Diffraction of Light by Acicular Particles

Chatoyancy ("cat's-eyes") and asterism ("stars") are optical phenomena that have been observed in gemstones for centuries. Their correlation with the minute needle-shaped inclusions in chatoyant and asteriated stones has been known since not long after the invention of the optical microscope. Surprisingly, the first qualitative explanation of the effect was not proposed until the early 1980s (Weibel et al., 1980; Wüthrich and Weibel, 1981; Wüthrich et al., 1983). When a beam of light intersects with a needle-shaped particle, the scattered light forms a cone with the needle as its axis (figure D-1A). The cabochon-cut surface of the stone acts as a convex lens, which focuses the scattered light from multitudes of needles inside the crystal into a bright line above the stone (figure D-1C) that can be observed by our eyes. Moon and Phillips (1984a and 1985) later described the phenomenon more quantitatively using Fraunhofer diffraction, which explains why thinner needle inclusions create sharper bright lines, as well as how the cat's-eye or star can be sharpened by reducing the spherical aberration from the cabochon surface.

The redirection of light around an obstacle (or an aperture) is called diffraction, a phenomenon exhibited by all forms of waves (e.g., sound waves, water waves). Basically, all optical phenomena in gemstones are created by light diffracting off the inclusions or textures with variable sizes and shapes. Note that the terms *scattering* and *diffraction* are often used to describe the same effect or physical process, with "scattering" emphasizing the random particle-like behavior of light, while "diffraction" stresses a wavelike nature that is more directional and predictable.

Because the bright line of scattered light is perpendicular to the needle direction (figure D-1), the number of bright lines (sometimes called branches or rays) in asterism and chatoyancy is dependent on the number of different orientations of the needle inclusions. The orientations of the needles are typically controlled by the crystallographic relation between them (the included phase) and the host mineral. Therefore, the distribution of the needles mostly follows the symmetry of the host mineral. This is why chatoyancy and 4-rayed stars are often observed in minerals of lower symmetry such as chrysoberyl (orthorhombic) and diopside (monoclinic), whereas 6-rayed and 12-rayed stars are mostly found in trigonal and hexagonal minerals such as corundum, quartz, and emerald.

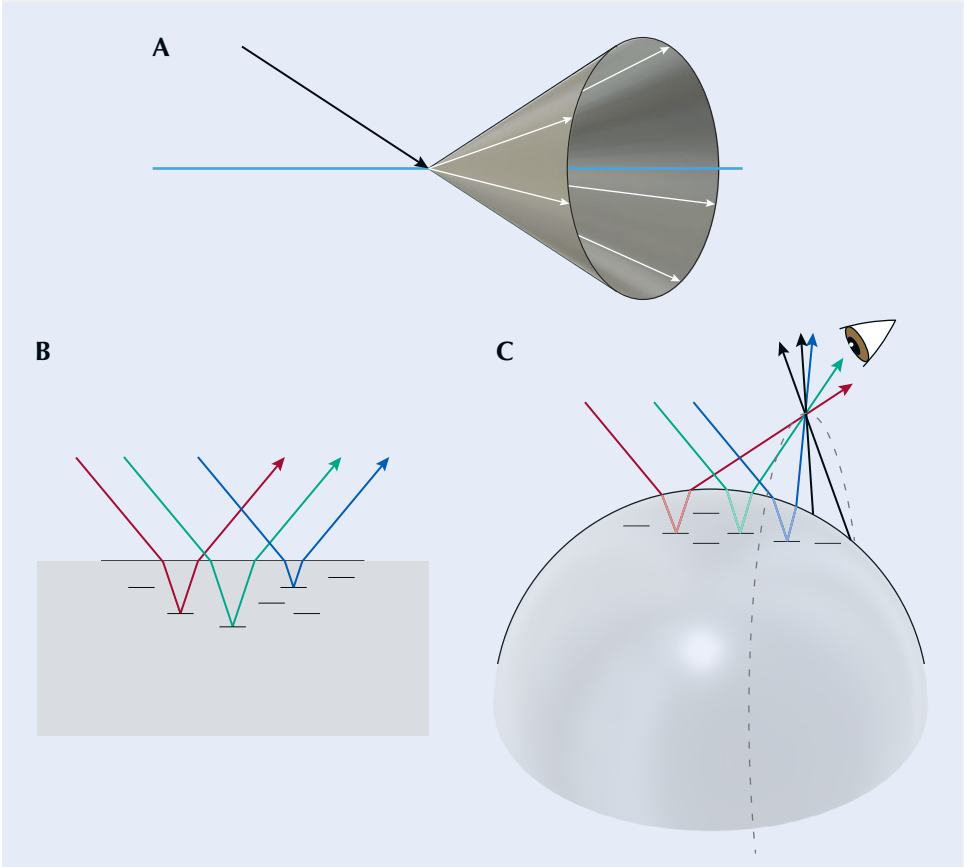

Figure D-1. A: Schematic diagram illustrating light scattered off a fine needle. The directions of the scattered light form a cone around the needle. B: If the surface of a stone were flat, the light rays scattered by different needle-like inclusions would be parallel to each other and no phenomenon would be observed. C: The curved surface of a cabochon-cut stone can focus the scattered light into a bright line above the surface.

The bright lines of different orientations intersect at a single point to form a star only when the needle directions lie in the same plane. Any two directions define a plane, and a third direction could be at an angle with the plane defined by the first two. The needles in cubic minerals, such as garnet and spinel, cannot all be coplanar. Moreover, the needles in some star quartz are oriented at an angle with the (001) plane. These non-coplanar needles can create a network of multiple stars connected to one another through their extended rays. Intergrowth between two crystals, such as twinning, can also misalign the needle planes and create double stars that are not connected to each other (figure D-2) (Koivula et al., 1993; McClure, 1998).

The illusion of the cat's-eye or star "floating" above the stone is sometimes described as the stereoscopic effect (Killingback, 2005; Bui et al., 2020), which is most noticeable on larger specimens due to the longer focal lengths of their less curved surfaces. The cat's-eye or star also moves dramatically when the stone is turned, as its position strongly depends on the direction of the incident light (figure D-1). When a chatoyant or asteriated stone is illuminated by multiple light sources, corresponding numbers of cat's-eyes and stars can be seen moving synchronously because each light source shines from a different angle (see video 1 at https://www.gia.edu/gems-gemology/summer-2025-phenomenal-gemstones).

Thanks to the densely distributed needle inclusions, chatoyant and asteriated gems are often semitranslucent with dark bodycolor, which means that only light scattered by needles near the surface makes it out of the stone. The denser the needle inclusions are, the sharper the cat's-eye or star typically is, because the light contributing to the phenomenon is more localized. When chatoyancy is observed in transparent or translucent stones, light is scattered by needles deeper in the stone, creating a special appearance under oblique lighting known as "milk-and-honey" (or "coffee-and-cream"), where the stone appears to be separated by the cat's-eye into a brighter ("cream"/"milk") half and a darker ("coffee"/"honey") half (Killingback, 2015). Some star ruby, sapphire, and quartz are even sufficiently transparent to let light reflect off the base of the cabochon, creating a second star with the same hue as the stone's bodycolor (Schmetzer et al., 2015).

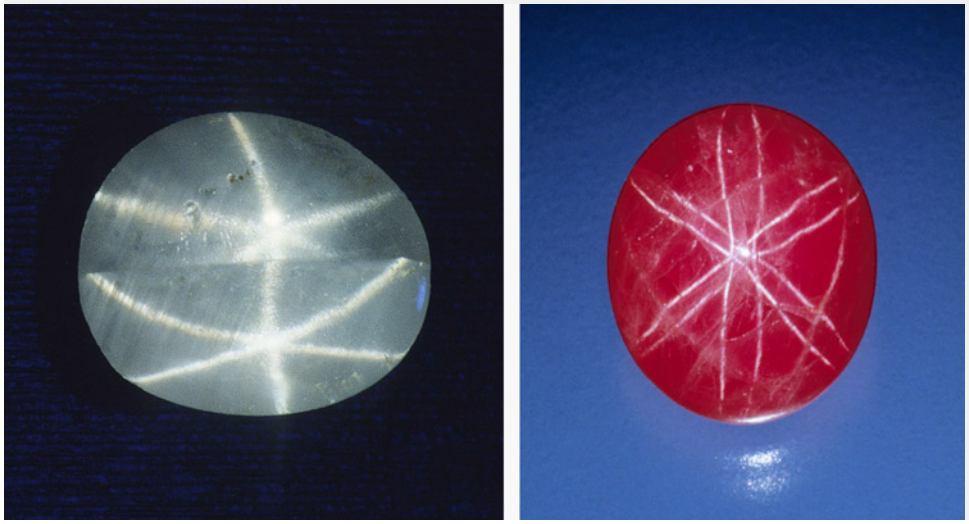

Figure D-2. Sapphire (left, 0.87 ct) and ruby (right, 8.19 ct) with double stars due to twinning. Note that the star sapphire contains only two twin domains, whereas the star ruby is polysynthetically twinned with microscopic twin domains. Photos by Robert Weldon (left) and Shane McClure (right).

TEM or micro-Raman spectroscopy, only circumstantial evidence of rutile could be found, such as the presence of titanium in the bulk composition as well as the high refractive index (RI) and brownish colors. Nassau (1968) suspected that the needles were tialite (Al_2TiO_5) due to the apparently lower symmetry but could not provide any evidence for this identification. Tialite is a synthetic material only stable at temperatures above ~1300°C and is thus unlikely to be found in any natural corundum, which generally forms at lower temperatures (Giuliani et al., 2014). The presence of rutile in synthetic star sapphire was first confirmed by Frondel (1954) by chemical and XRD tests on crushed and centrifugation-separated precipitates. The first direct observation of rutile needles in synthetic sapphire using TEM was done by Phillips et al. (1980) nearly three decades later. Viti and Ferrari (2006) reported a "monoclinic polymorph

of TiO_2" in a Verneuil-grown star sapphire, although the TEM images and the electron diffraction patterns clearly show a twinned rutile structure. The behavior of titanium in synthetic titanium-doped corundum is relatively well understood after the study by He et al. (2011) showed only two types of titanium-containing precipitates, riesite and rutile, depending on the annealing temperature and time.

Similar to nanoprecipitates, needle inclusions in natural corundum are significantly understudied. Moon and Phillips (1984b) first applied TEM to natural black (star) Australian sapphire and surprisingly discovered hematite (Hem: α-Fe_2O_3) and/or ilmenite (Ilm: $FeTiO_3$) as the star-creating needles, instead of rutile, supporting an earlier claim by Weibel and Wessicken (1981) on a Thai black star sapphire with no detectable titanium. The authors also reported that rutile was observed in blue and blue-green stones from Australia but did not publish the data. Needle-shaped hematite/ilmenite inclusions have been reported multiple times as the star-forming silk since the original discovery (Saminpanya, 2001; Izokh et al., 2010; Khamloet et al., 2014; Bui et al., 2015, 2017; Soonthorntantikul et al., 2017; Sorokina et al., 2017; Liu et al., 2022), including almost pure hematite in a titanium-free corundum from Shandong, China (Zhao et al., 2022). On the other hand, despite mounting circumstantial evidence for the rutile needle inclusions in natural corundum, it was not until recently that direct confirmation using electron probe microanalysis (EPMA) and electron backscatter diffraction (EBSD) was first reported (Palke and Breeding, 2017). It appears that ilmenite and/or hematite inclusions are more common than rutile as the star-forming needles in corundum, which makes sense as natural corundum contains much more iron than titanium. However, there could also be a bias caused by rutile needles being generally smaller and harder to identify. As the studies on this subject are very limited, it is not possible to estimate the percentage of each type of inclusion in natural corundum.

TEM analyses show the ilmenite/hematite inclusions are elongated along the ⟨100⟩ direction (ilmenite and hematite have the same crystallographic orientation as corundum as they are isostructural) (Moon and Phillips, 1984b; Zhao et al., 2022), whereas the rutile needles are elongated along $\langle 011\rangle_{Rt} \| \langle 210\rangle_{Crn}$, with $\{100\}_{Rt} \| \{001\}_{Crn}$ (figures 9 and 10) (Phillips et al., 1980; Jayaram, 1988; Moon and Phillips, 1991; Xiao et al., 1997; Viti and Ferrari, 2006; He et al., 2011).

Figure 9. Left: $[001]_{Crn}$ ($[100]_{Rt}$) zone axis darkfield TEM image showing needle-shaped and heart-shaped twinned rutile precipitates in titanium-doped synthetic sapphire annealed at 1300°C for 50 hours. The selected area electron diffraction patterns of the two precipitates are shown as insets. Right: $[210]_{Crn}$ ($[011]_{Rt}$) zone axis high-resolution TEM image showing the $(110)_{Crn} \| (011)_{Rt}$ interface with periodic dislocations (white arrows) to accommodate the lattice mismatch between rutile and corundum crystal structures. Images from He et al. (2011).

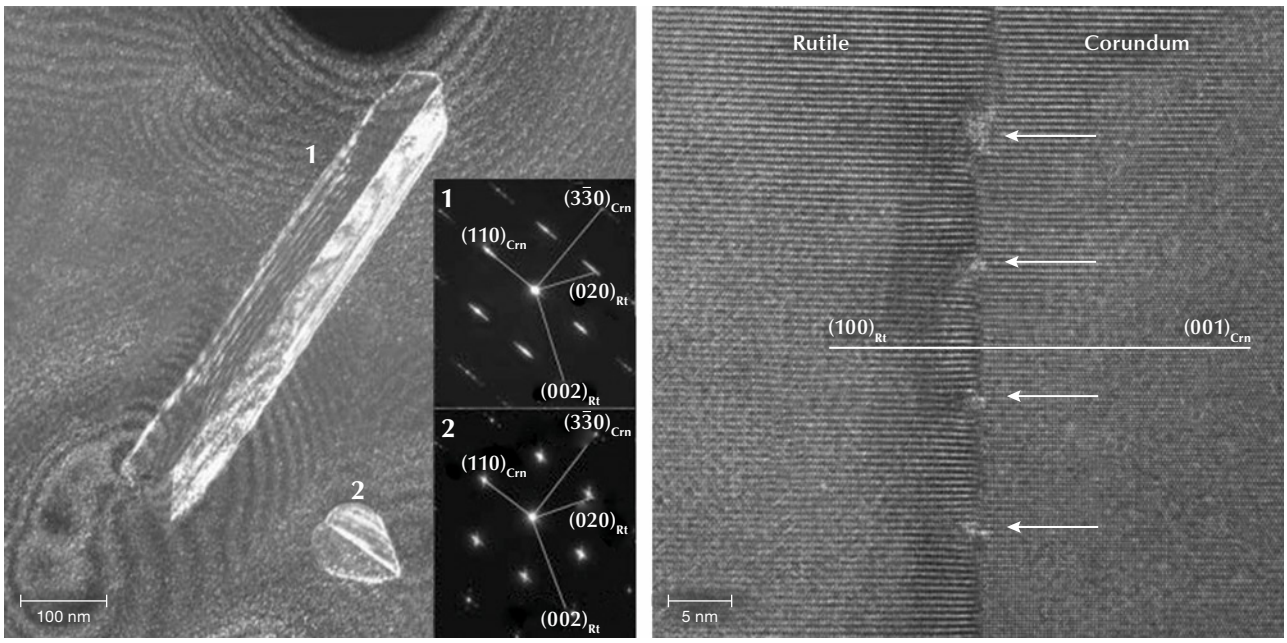

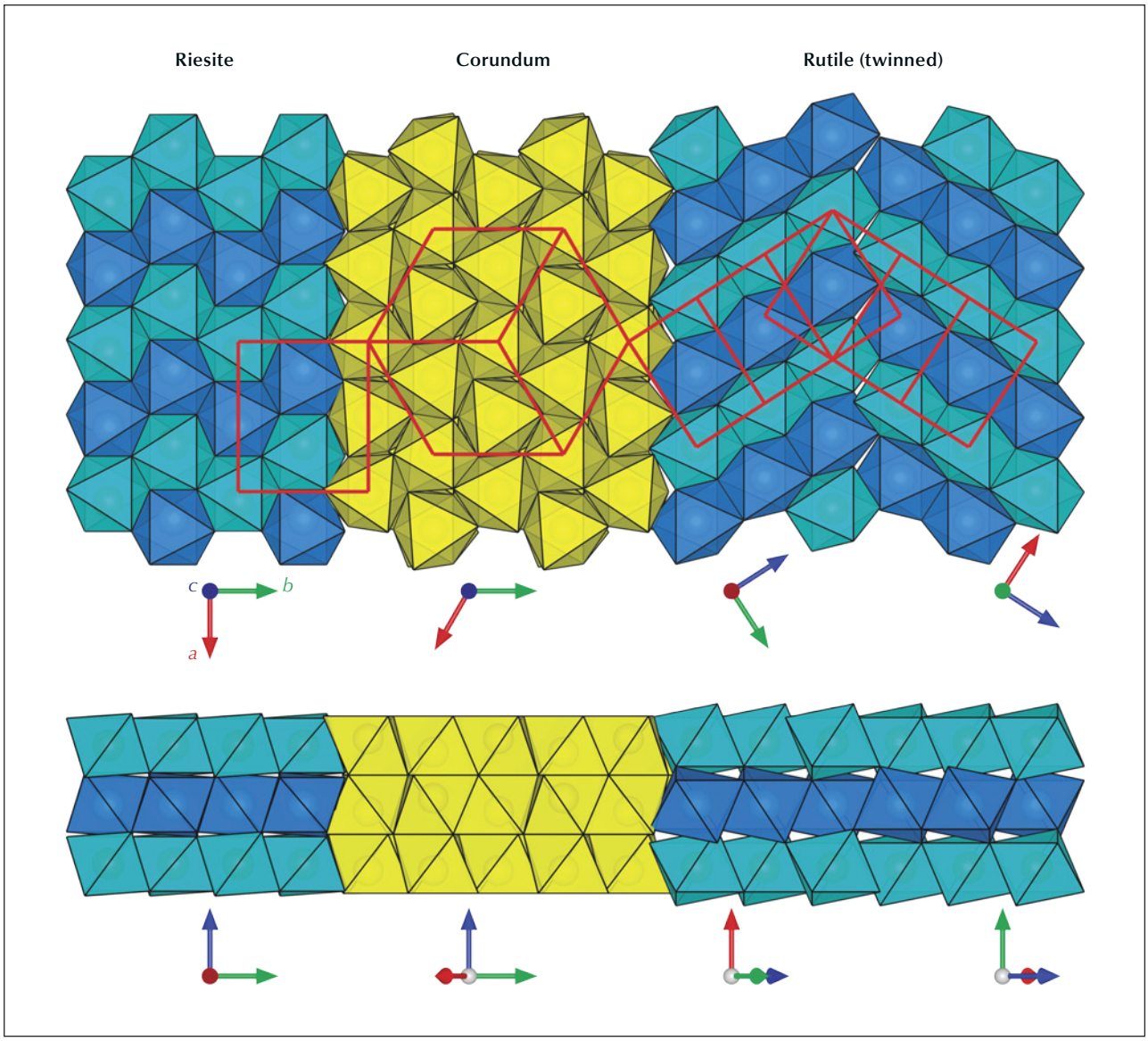

Figure 10. Structural relations between the corundum host and titanium oxide inclusions at the $\{110\}_{Crn}$ interface. The different layers of titanium octahedra are differentiated by two shades of blue. The unit cells of each structure domain are depicted by red boxes to highlight symmetry and orientation. The coherent boundaries between corundum and the needle inclusions determine the specific CORs. Note that the lattice match between corundum and riesite is much better, which is presumably why riesite precipitates first at low temperatures. Rutile, which is more stable at ambient pressure, eventually takes over with larger precipitates (or at higher temperatures), which requires periodic dislocations at the interface and twinning to accommodate the different lattice dimensions.

Therefore, the needles perpendicular to the growth zoning of corundum are ilmenite or hematite, whereas those parallel to the growth zoning are rutile (figure 11). Mayerson (2001) incorrectly claimed that all stars in untreated natural sapphire are parallel to the growth zoning, and thus mistakenly concluded that stars with rays perpendicular to growth zoning can be an indication of titanium-diffused star sapphire. When needles of both orientations are present in the same corundum crystal, a rare 12-rayed star can be observed (again, see figure 1, top left). The two sets of 6 rays in a 12-rayed star may show different colors (Vertriest and Bruce-Lockhart, 2018), as rutile silk mostly appears silver white (figure 8A) and hematite/ilmenite silk can appear golden yellow depending on the iron content (figure 8, C and D). It should be noted that Bui et al. (2017) claimed that only ilmenite inclusions could be found in a 12-rayed

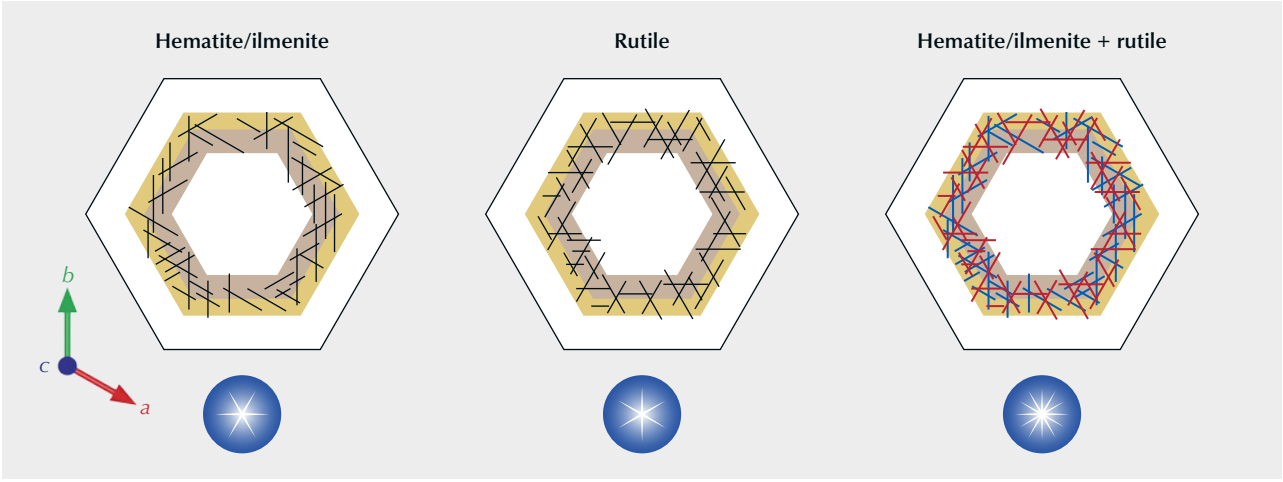

Figure 11. Schematic drawing showing the orientation relation between needle inclusions and growth zoning of corundum. Hematite and ilmenite needles are mostly perpendicular to the growth bands, creating a star with rays parallel to the banding; rutile needles are always parallel to the growth bands, and the rays are perpendicular. If both types of needles are present, a 12-rayed star is created.

star sapphire likely from Sri Lanka, although the Raman spectra presented in their paper do not conclusively exclude the presence of rutile.

Iron and titanium are among the most common trace elements in natural corundum, which is why it is generally believed that these needle inclusions form by solid-state precipitation of iron and/or titanium dissolved in the corundum structure. Natural rutile silk has the same crystallographic orientation relation (COR) as synthetic or titanium-diffused star sapphire, suggesting a similar formation mechanism. Little is known about the formation mechanism of the ilmenite/hematite needles, as heating an iron-rich corundum failed to produce any similar precipitates (Moon and Phillips, 1991). Iron is much more soluble in corundum than titanium and probably would not precipitate unless annealed at significantly lower temperatures for much longer periods than in the study by Moon and Phillips (1991), and exsolution may be achievable only in natural geological settings.

It should be noted that experiments of epitactic growth of rutile (Gao et al., 1992) and hematite (Wang et al., 2002) on a corundum substrate can also create coherent or semi-coherent interfaces similar to those observed for the needles exsolved in the corundum matrix (He et al., 2011; Zhao et al., 2022). Palke and Breeding (2017) first argued for epitactic coprecipitation of the oriented needle rutile inclusions containing heavy HFSEs, based on observations of glassy melt inclusions that indicate fast cooling, as well as the assumption that the heavy HFSEs are strongly incompatible and thus unlikely to be incorporated into the corundum lattice during crystal growth. However, this argument has been invalidated by a recent APT study showing that significant amounts of heavy HFSEs (e.g., tungsten, niobium, and tantalum) can not only be dissolved into the crystal structure of natural corundum but are also likely to be enriched beyond their solubility in corundum due to preferred adsorption on the growth surfaces (Jin et al., 2024). This means that the precipitation of HFSEs could occur when the already supersaturated host corundum is heated above its formation temperature, which would be a much faster process than previously thought.

Moreover, the distribution of rutile silk in natural corundum mostly correlates with fluctuating titanium concentrations associated with the hexagonal {110} growth zoning, yet the basal $\{001\}_{Crn}$//$\{100\}_{Rt}$ interfaces of the needle inclusions are always wider than the vertical $\{110\}_{Crn}$//$\{011\}_{Rt}$ interfaces, as evidenced by the much stronger reflection seen on the $\{001\}_{Crn}$ surface (again, see figure 8, A and B). These observations are hard to reconcile with the epitactic coprecipitation mechanism, because if the epitaxy occurs on the basal $\{001\}_{Crn}$ surface, as suggested by the platy needle shape, its distribution should not correlate with the {110} growth zoning.

The precipitation of rutile (or other iron/titanium oxide) from corundum should result in a rim deprived of titanium (and/or iron) immediately around the precipitation, a texture that in theory could be used to test the formation mechanism of the needle inclusions. Unfortunately, such small variations at the nanometer scale are difficult to detect using current techniques,

and the compositional gradient may have been erased by diffusion in any natural corundum. The nanoscale polysynthetic twinning of rutile needle inclusions (figure 9) (He, 2006; Viti and Ferrari, 2006) is also likely to be exclusive to solid-state exsolution as a mechanism to redistribute the strain, since similar structures have not been reported in epitactically coprecipitated rutiles (Gao et al., 1992). It is not clear, however, how such nanoscopic twinning would be preserved in natural corundum over geological timescales.

CAT'S-EYE AND STAR CHRYSOBERYL

Cat's-eye chrysoberyl is the most recognized and most valuable chatoyant gemstone, especially if it is accompanied by a color change (cat's-eye alexandrite; figure 12A). In fact, the term *cat's-eye* refers to chatoyant chrysoberyl by default if the mineral species is not specified. Chrysoberyl (Cbrl: $BeAl_2O_4$) is a beryllium aluminate mineral that crystallizes in an olivine-type structure, with hexagonal close-packed (HCP) oxygen atoms positioned as in the corundum and hematite structures. The cation arrangement in the chrysoberyl structure, with half of the octahedral sites filled by aluminum and one-eighth of the tetrahedral sites filled by beryllium, results in a pseudohexagonal orthorhombic symmetry. The chrysoberyl structure has been reported in many different crystallographic axis settings, making it difficult to compare the orientation notations across the literature. The *Pmnb* (a = 5.48 Å, b = 9.42 Å, c = 4.43 Å) setting will be used in this article because it intuitively keeps the HCP stacked layers parallel to (001), making it easy to compare different close-packed structures (Drev et al., 2015). The Miller indices cited in the literature using other settings will be translated to the *Pmnb* setting.

Despite its long history as a prominent phenomenal gemstone, there had not been any serious investigation into the details of needle inclusions in chrysoberyl until recently. By using a combination of optical microscopy, scanning electron microscopy equipped with energy-dispersive X-ray spectroscopy (SEM-EDS), and Raman spectroscopy, Schmetzer et al. (2016) conducted a comprehensive survey of included chrysoberyl from different locations and showed that almost all needle inclusions in natural chrysoberyl are rutile, with the only exception of ilmenite needles

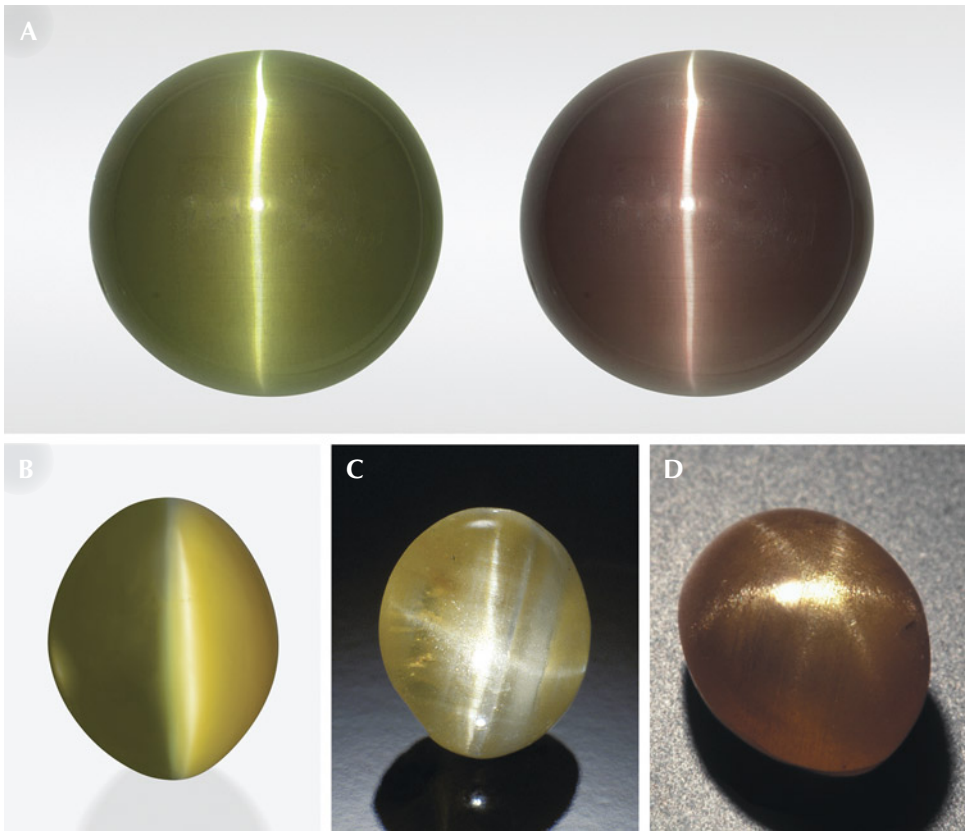

Figure 12. A: A 21.22 ct cat's-eye alexandrite under fluorescent light (left) and incandescent light (right). B: A 5.39 ct cat's-eye chrysoberyl displaying a "milk-and-honey" effect; courtesy of Tim Roark, Inc. C: A 1.54 ct four-rayed star chrysoberyl from Sri Lanka. D: A 2.29 ct natural six-rayed star chrysoberyl. Photos by Shunsuke Nagai (A), Orasa Weldon (B), Robert Weldon (C), and Maha Tannous (D).

found in a four-rayed star chrysoberyl from Sri Lanka. The oriented needle inclusions presumably form by precipitation of titanium originally dissolved in the chrysoberyl structure. Elongated cavities or channels may also exist along the same orientations as the rutile needles.

Three different needle orientations have been observed in chrysoberyl, elongated along the $[100]_{Cbrl}$, $\langle 110\rangle_{Cbrl}$, and $[001]_{Cbrl}$ axes. The $[100]_{Cbrl}$ needles sometimes occur together with $\langle 110\rangle_{Cbrl}$ needles, forming a pseudohexagonal array at a ~60° angle relative to one another. The $\langle 110\rangle_{Cbrl}$ needles are often connected as twinned pairs to form a V shape, a heart shape, or a triangle, depending on needle width. Ilmenite needles are reported to occur only along the $[100]_{Cbrl}$ axis. No TEM analysis has been done on the needle inclusions parallel to the $(001)_{Cbrl}$ plane, but they most likely have an orientation similar to the rutile needles found in star sapphire in light of their similar HCP structures. The only atomic-resolution TEM study of the rutile precipitates in chrysoberyl, conducted on a twinned sample from Bahia, Brazil, showed a COR of $\{013\}_{Rt}$//$\{120\}_{Cbrl}$ + $\langle 100\rangle_{Rt}$||$\langle 001\rangle_{Cbrl}$, which corresponds to the needles and striped plates elongated along the [001] axis of chrysoberyl with L-shaped or zigzag cross sections observed by Schmetzer et al. (2016). It should be noted that these inclusions are quite unusual because they are elongated perpendicular to the stacked oxygen layers in the structure, rather than parallel to them.

Depending on the dominant needle orientation and the cut of the material, chrysoberyl can display chatoyancy or asterism with up to six rays (figure 12). It is not clear what process controls the orientation of the needle inclusions in chrysoberyl, but the temperature at which the titanium oxide starts precipitating out may play an important role. Synthetic cat's-eye and star chrysoberyl can be produced by growing Ti^{3+}-doped crystals in neutral or reducing atmospheres and then annealing in an oxygen atmosphere to precipitate TiO_2. Only needles parallel to the $(001)_{Cbrl}$ plane have been observed in synthetic chrysoberyl (Schmetzer and Hodgkinson, 2011; Schmetzer et al., 2013, 2016). Titanium diffusion, as used to create artificial stars in sapphire, can also create chatoyancy in chrysoberyl. Another method, which uses a floating zone technique to create cat's-eye alexandrite with tubular fluid inclusions, has been patented by the Seiko Epson Corporation in Japan (Schmetzer et al., 2013).

STAR GARNET

Silicate garnet (Grt: $X_3^{2+}Y_2^{3+}[SiO_4]_3$) is a mineral group with one of the highest possible symmetries in three-dimensional space (space group 230, the last space group). The cubic symmetry allows the needle inclusions to be arranged in three dimensions, instead of coplanar as in corundum (figure 13). As a result, the bright lines constructing the asterism cannot all intersect at one point, which means multiple stars

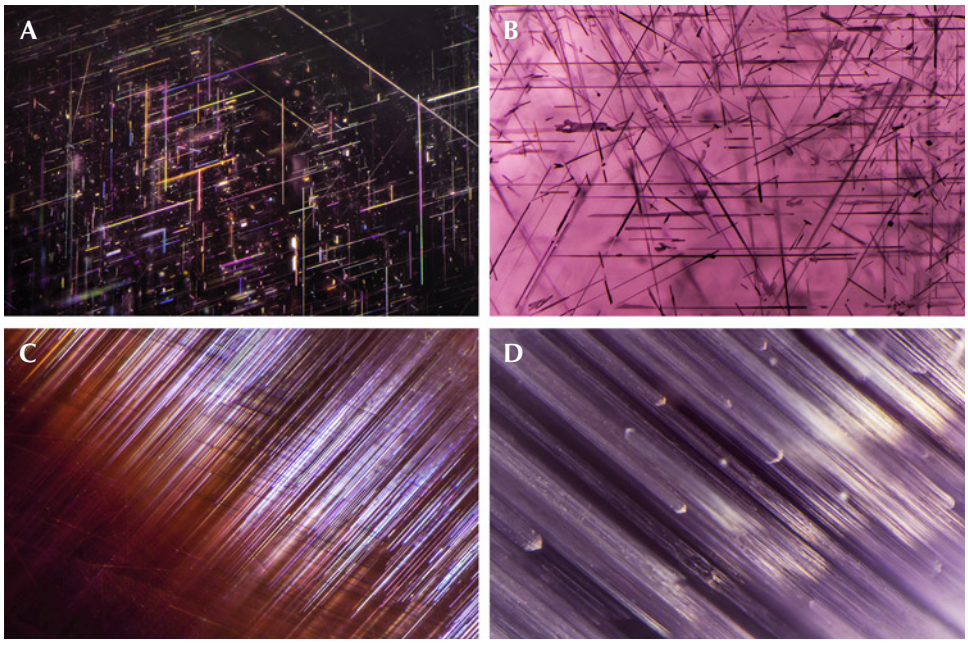

Figure 13. A: Rutile needles in star garnet. B: Needle inclusions in star spinel. C: Needle inclusions in cat's-eye garnet. D: Linear inclusions in cat's-eye spinel. Photomicrographs by Nathan Renfro; fields of view 3.35 mm (A), 3.38 mm (B), 1.95 mm (C), and 3.09 mm (D).

may be seen on a single garnet crystal. The best shape to demonstrate this "star network" is a sphere, as is commonly used when cutting a star garnet. Depending on the orientations of the needle inclusions, different asterism patterns may be observed on a polished spherical garnet crystal (figure 14). Therefore, the angles between the rays of the stars can be used to identify the orientations of the inclusions (Walcott, 1937; Kumaratilake, 1998; Schmetzer and Bernhardt, 2002; Schmetzer et al., 2002). Sometimes two different sets of inclusions can appear in the same garnet crystal, creating more complicated networks of stars (Guinel and Norton, 2006). Similar asterism patterns, although much rarer, can sometimes be observed in spinel crystals, which also belong to the cubic crystal system (Walcott, 1937; Schmetzer, 1988; Kumaratilake, 1998; Schmetzer et al., 2000; Promwongnan et al., 2017; Hughes, 2018).

While rutile is the most common needle inclusion in garnet, other oriented inclusions such as ilmenite, magnetite, corundum, apatite, quartz, mica, olivine, pyroxene, and amphibole have also been observed (van Roermund et al., 2000; Hwang et al., 2010, 2013; Zhang et al., 2011; Ague and Eckert, 2012; Axler and Ague, 2015; Xu and Wu, 2017; Keller and Ague, 2019, 2020). However, the relation between asterism and inclusions other than rutile needles has yet to be confirmed. Most rutile needles are elongated along the ⟨111⟩ directions of garnet, creating four-rayed stars intersecting at ~70°/110° angles

Figure 14. Schematic diagram showing the different needle orientations and their corresponding star networks in star garnet. A: ⟨100⟩ needles create six 4-rayed stars with 90° angles. B: ⟨110⟩ needles create six 4-rayed stars with 90° angles and eight 6-rayed stars with 60° angles. C: ⟨111⟩ needles create twelve 4-rayed stars with ~70°/110° angles. D: Combinations of more than one set of needles can create more complicated networks. Note that almost all 6-rayed stars found in garnet are created by a combination of ⟨100⟩ and ⟨111⟩ needles (yellow and purple lines in D).

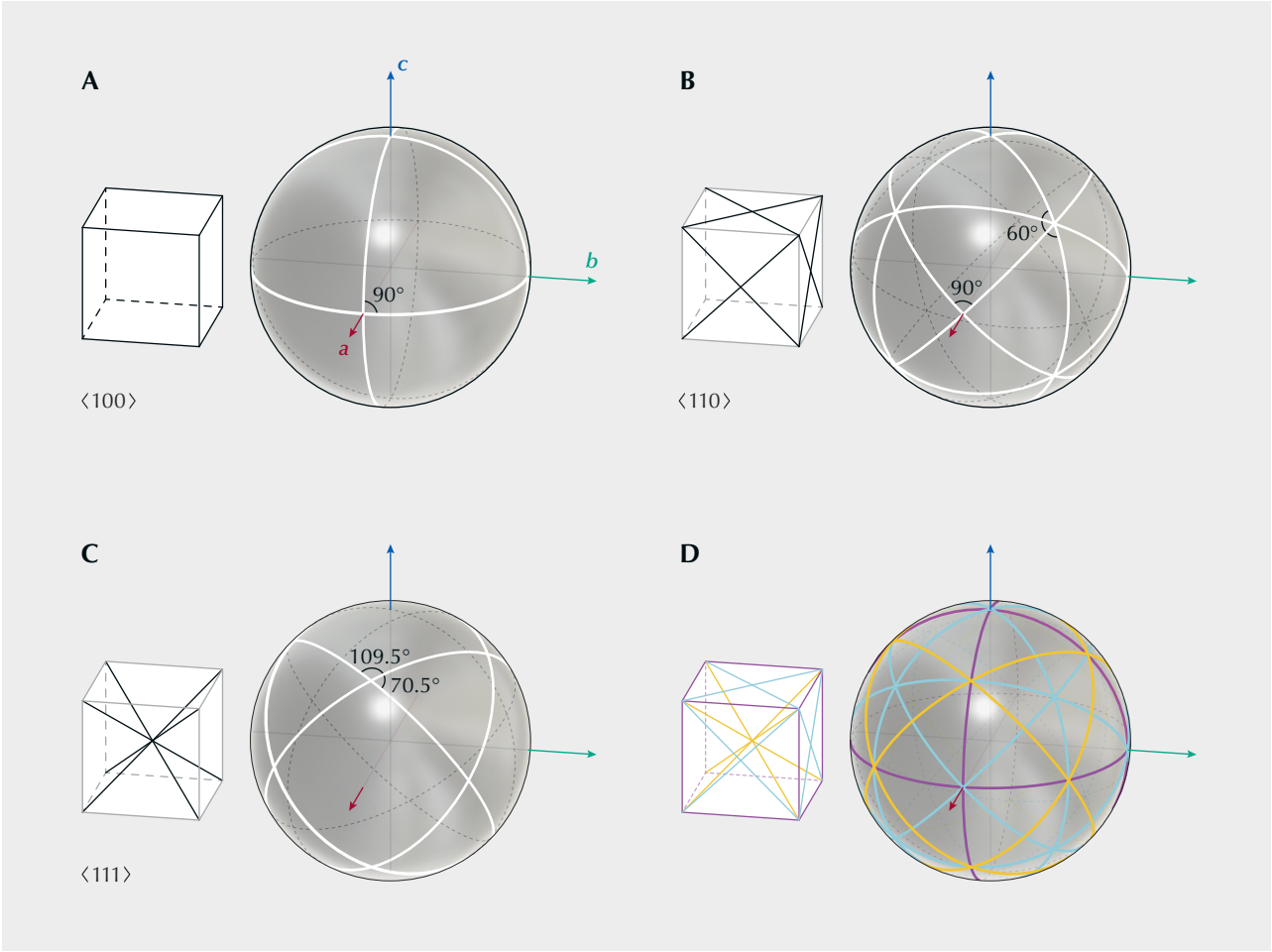

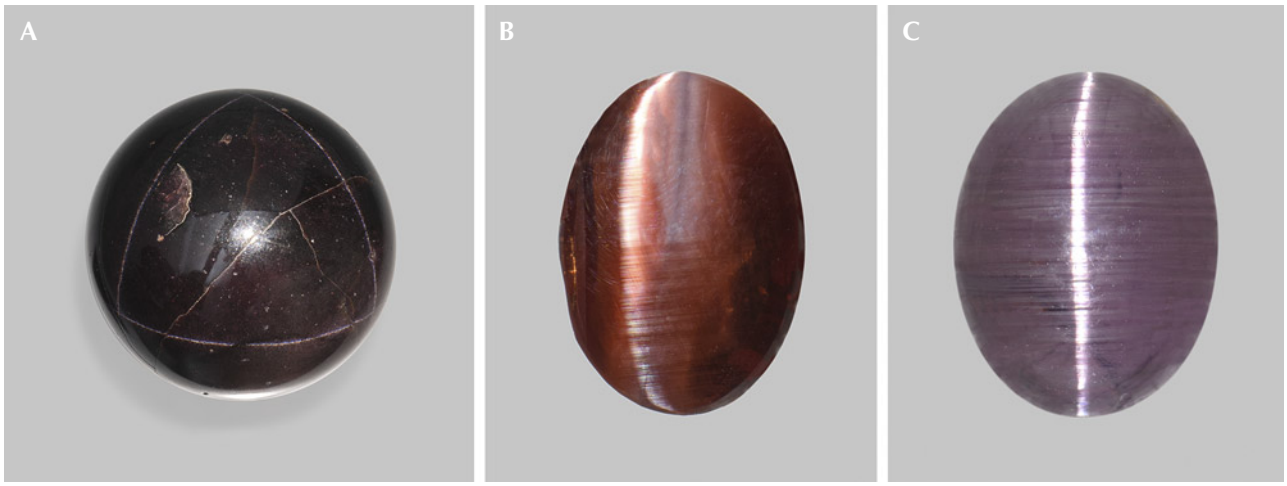

Figure 15. A: A 1,185 ct garnet sphere showing a star network of ⟨111⟩ needle inclusions (see figure 14). The star network under rotation is shown in video 2. Courtesy of GIA Museum, collection no. 4068. B: A 1.47 ct cat's-eye almandine garnet. C: A 9.39 ct cat's-eye spinel from Sri Lanka; courtesy of John I. Koivula. Photos by Emily Lane (A) and Annie Haynes (B and C).

(figures 14C and 15A; video 2). Rutile needles elongated along the $\langle 001 \rangle_{Grt}$ directions have also been reported (Hwang et al., 2015), producing asymmetric six-rayed stars with ~70°/55°/55° angles together with the $\langle 111 \rangle_{Grt}$ needles.[2] Although specific CORs between the rutile needles and the garnet host are commonly observed in TEM and EBSD analyses of star garnet, such as $\{100\}_{Rt} /\!/ \{13\bar{4}\}_{Grt} + \langle 013 \rangle_{Rt} \| \langle 111 \rangle_{Grt}$ or $\{100\}_{Rt} \| \{011\}_{Grt} + \langle 011 \rangle_{Rt} \| \langle 100 \rangle_{Grt}$ (Keller and Ague, 2022), many of the $\langle 111 \rangle_{Grt}$ needles show nonspecific or "statistical" CORs, with $[001]_{Rt}$ falling onto a cone of 28.5°±2.5° around $\langle 111 \rangle_{Grt}$ (Keller and Ague, 2019).

Most star garnets are in the almandine-pyrope-spessartine ($Fe_3Al_2Si_3O_{12}$–$Mg_3Al_2Si_3O_{12}$–$Mn_3Al_2Si_3O_{12}$) solid-solution series that form under high-pressure conditions deep in the earth. Due to its stability over a wide range of temperature and pressure conditions, garnet is an important indicator of evolving metamorphic conditions and underlying tectonic processes, and it has been studied extensively by metamorphic petrologists. Consequently, the formation mechanism of the needle inclusions is essential for the correct interpretation of the garnets' chemical data, which is why the CORs of the needles in garnet have drawn a lot of attention in the past decade. The complex crystal structure and chemistry of garnet, and the accordingly more diverse CORs of the needle inclusions, make this already controversial subject even more convoluted. As a result of the more complicated chemical reactions and structure-matching schemes, many different mechanisms have been proposed to explain the formation process of these needle inclusions, including solid-state precipitation, interface-coupled dissolution-reprecipitation, and epitactic co-growth or overgrowth. Proyer et al. (2013) as well as Keller and Ague (2019) discussed all hypotheses in detail and concluded that (open-system) solid-state precipitation (exsolution) is the only process that withstands scrutiny. Other hypotheses either contradict observations or lack key supporting evidence. This conclusion is further supported by the successful prediction of CORs using an edge-to-edge matching model (Keller and Ague, 2022).

It should be noted that the asymmetrically oriented rutile needles intersecting the growth zones at steep angles (e.g., figure 13, C and D) are harder to explain by solid-state precipitation, which led to the interpretation of epitactic nucleation and co-growth (Griffiths et al., 2020). Precipitation within the crystal should fully observe the symmetry of the host mineral, whereas crystallization is one-dimensional along the growth surface, which reduces the local symmetry. However, as pointed out by Keller and Ague (2019), preexisting crystallographic defects, chemical gradients, as well as varying lattice parameters might also promote preferred precipitations along certain directions. Nonetheless, these parallel needles could create chatoyancy instead of asterism in the occasionally reported cat's-eye garnet (figures 13C and 15B). Similar linear features can also be found in cat's-eye spinel (figures 13D and 15C).

[2]The $\langle 011 \rangle_{Grt}$ needle orientation reported by Guinel and Norton (2006) is an error and should be $\langle 001 \rangle_{Grt}$ instead.

STAR QUARTZ

Although rutile is the most common needle-like inclusion in quartz (Qz: α-SiO_2) and can create poor-quality asterism or chatoyancy with a strange shape (Johnson and McClure, 1997; Schmetzer and Steinbach, 2022, 2023; Gauthier et al., 2023), the high-quality stars observed in quartz are not related to titanium oxide. These star quartzes are only found as turbid massive quartz and never as clear euhedral quartz crystals (Goreva et al., 2001; White, 2015), although there may be a sampling bias because only massive anhedral quartz would be cut into cabochons or spheres to display the asterism. Most star quartz has pink color that varies from bright to pale; thus, it is called rose quartz. This name is sometimes also applied to euhedral pink quartz crystals, the color of which is photochemically unstable and can be bleached away easily with UV light or low heat. The pink color of massive star rose quartz, on the other hand, is stable up to ~575°C, indicating a completely different coloring mechanism.

Sillimanite (Sil: Al_2SiO_5) was first identified using TEM as the needle inclusions in a star quartz from the Ratnapura district, Sri Lanka (Woensdregt et al., 1980), elongated along $\langle 001\rangle_{Sil} \| \langle 100\rangle_{Qz}$, with $\{110\}_{Sil} \| \{001\}_{Qz}$. Dumortierite (Dum: $Al_7Si_3BO_{18}$) was also identified as the fibrous residue observed after rose quartz was dissolved in hydrofluoric acid (Applin and Hicks, 1987; Ignatov et al., 1990; Goreva et al., 2001). Further study revealed that these dumortierite inclusions contain significant amounts of iron and titanium, and they show a superlattice structure likely due to cation ordering (Ma et al., 2002). The pink color of rose quartz turned out to result from the iron-titanium intervalence charge transfer in these nano-inclusions. It should be noted that the earlier reports of rutile nanoneedles in rose quartz (von Vultée, 1955, 1956; Eppler, 1958) were most likely incorrect, as none of the 29 rose quartz samples from different locations analyzed by Goreva et al. (2001) showed any evidence of rutile. Regrettably, the COR between these dumortierite needles

Figure 16. A: A 178 ct 12-rayed star rose quartz sphere in transmitted light; courtesy of Far Arden Essentials. B: An 8.51 ct double polished rose quartz cabochon showing double stars due to reflection from the back surface; courtesy of GIA Museum, collection no. 35214. C: A 31.37 ct star quartz from Sri Lanka shows a complex network of stars with a 12-rayed star in the center; courtesy of Michael Schramm. D: A 44.25 ct star smoky quartz with a network of stars; courtesy of GIA Museum, collection no. 31575. E: A 22 ct multi-star quartz with a strong 6-rayed star in the center. Photos by Lylith Aradia Moon (A), Emily Lane (B and D), Maha Tannous (C), and Andrew Quinlan (E).

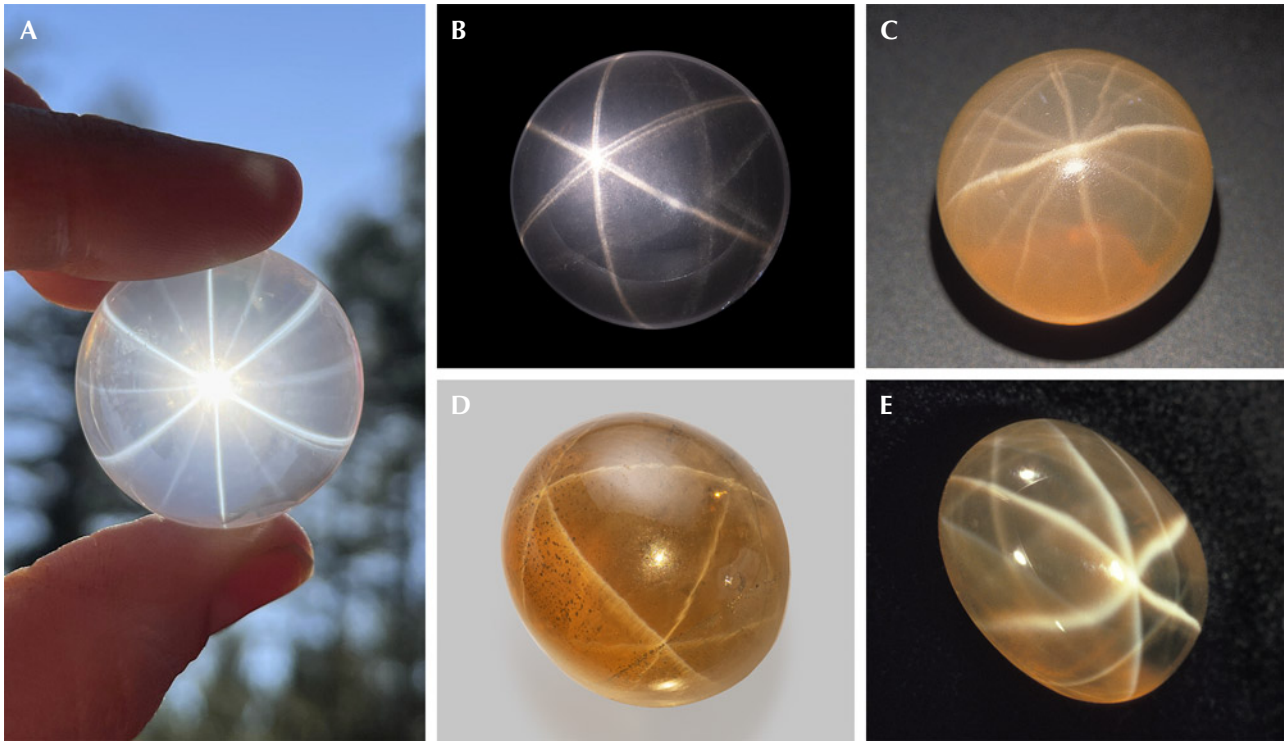

Figure 17. A: A 255 ct polished rectangular slice of tiger's-eye from South Africa. B: A 22.03 ct tiger's-eye cabochon from South Africa showing waves due to bent inclusions; courtesy of John I. Koivula. C: A 220 ct hawk's-eye oval cabochon. D: A 19.82 ct pietersite round cabochon showing chatoyant fragments of different colors. Photos by Emily Lane (A and C) and Annie Haynes (B and D).

and the quartz host is unknown, as all analyses were performed on residue fibers with all the quartz dissolved away.

The silicate needle inclusions, most likely formed by solid-state exsolution (Ma et al., 2002), have low RIs that are close to those of the quartz host, resulting in much weaker scattering power compared to the strongly refractive rutile or iron oxide inclusions in other gemstones. Therefore, star quartz has a more transparent appearance than star corundum or garnet. The star in rose quartz is often more strongly observed using light transmitted through the stone, an effect known as "diasterism" (figure 16A) (Killingback, 2006), whereas only "epiasterism" under reflected light can be observed in most other asteriated gemstones.

Some rose quartz crystals display 12-rayed stars, indicating two sets of needle inclusions with different crystallographic orientations (figure 16, A and C). It is possible that the two orientations are from different mineral inclusions, as both dumortierite and boron-bearing sillimanite were found as needles in a rose quartz from Brazil (Ma et al., 2002). Needle inclusions elongated off the (001) plane are also occasionally observed in quartz (Johnson and Koivula, 1999; Schmetzer and Glas, 2003), creating complex star networks in sphere-cut crystals similar to star garnet (figure 16, D and E; video 3). Chatoyancy is also very rarely observed in quartz (Choudhary and Vyas, 2009; Choudhary, 2011), indicating needle inclusions elongated parallel to the *c*-axis. Unfortunately, the nature of these abnormally oriented needles is not clear.

TIGER'S-EYE AND PIETERSITE

Tiger's-eye is a chatoyant variety of quartz containing altered amphibole needle inclusions (figure 17, A and B). Unlike the other star or chatoyant gemstones in which the host is a single crystal, tiger's-eye consists of columnar polycrystalline quartz crystals that are 0.1–1.0 mm in diameter and 1–10 mm in length (Heaney and Fisher, 2003). As indicated by its orientation, the chatoyancy of tiger's-eye is created by fibrous mineral inclusions and not the columnar quartz crystals (figure 18). No special COR has been observed between the needle inclusions and the

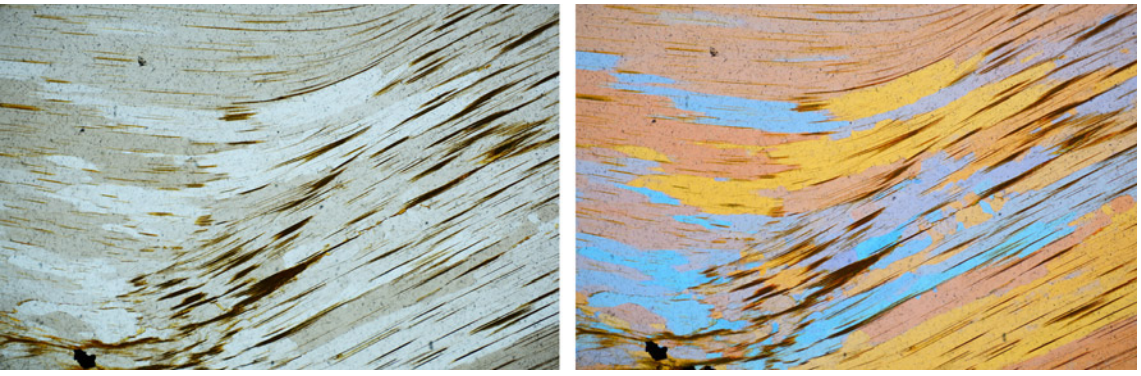

Figure 18. Thin section of tiger's-eye under cross-polarized light (left) and with a lambda plate inserted to enhance the contrast across grain boundaries (right). The dark brown needles are the iron oxide/hydroxide from weathered amphibole. Photomicrographs by Amir C. Akhavan; field of view 1.5 mm.

quartz crystals, suggesting that the aligned needle orientation must be controlled by crystal growth. The typical golden-brown color is caused by the iron-rich amphibole needles being weathered to iron (hydr)oxides. In the less common dark blue variety, commonly known as hawk's-eye (or falcon's-eye) (figure 17C), the amphibole needles are less altered and retain their original color.

Tiger's-eye has long been attributed to pseudomorphism with quartz replacing crocidolite, a blue asbestiform variety of the sodic amphibole riebeckite (Rbk: $Na_2Fe_5Si_8O_{22}(OH)_2$) (Wibel, 1873). However, Heaney and Fisher (2003) proposed that quartz and riebeckite grew synchronously through an episodic crack-seal mechanism, as optical and electron microscopic observations failed to show any evidence for pseudomorphism.

Pietersite, reportedly found only in Namibia and China, is generally described as a brecciated variety of tiger's-eye (figure 17D). Although the chatoyancy is also caused by crocidolite fibers, the silica that composes pietersite is in the form of chalcedony (discussed later in the section on iridescent agate) instead of columnar quartz. The chaotic texture of pietersite also indicates a formation mechanism different from that of tiger's-eye. Instead of pseudomorphism or a crack-seal mechanism, pietersite specimens are theorized to have formed as solution breccias, in which the crocidolite fibers form by late-stage reactions between chalcedony and hematite in a sodic fluid (Hu and Heaney, 2010).

OTHER ASTERIATED AND CHATOYANT STONES

Needle-like inclusions, which are the most common inclusion habits, can be found in almost any included mineral. The shape of an inclusion is often controlled by the lattice match across the boundary between the included mineral and the host, as demonstrated by the examples discussed above. A needle inclusion

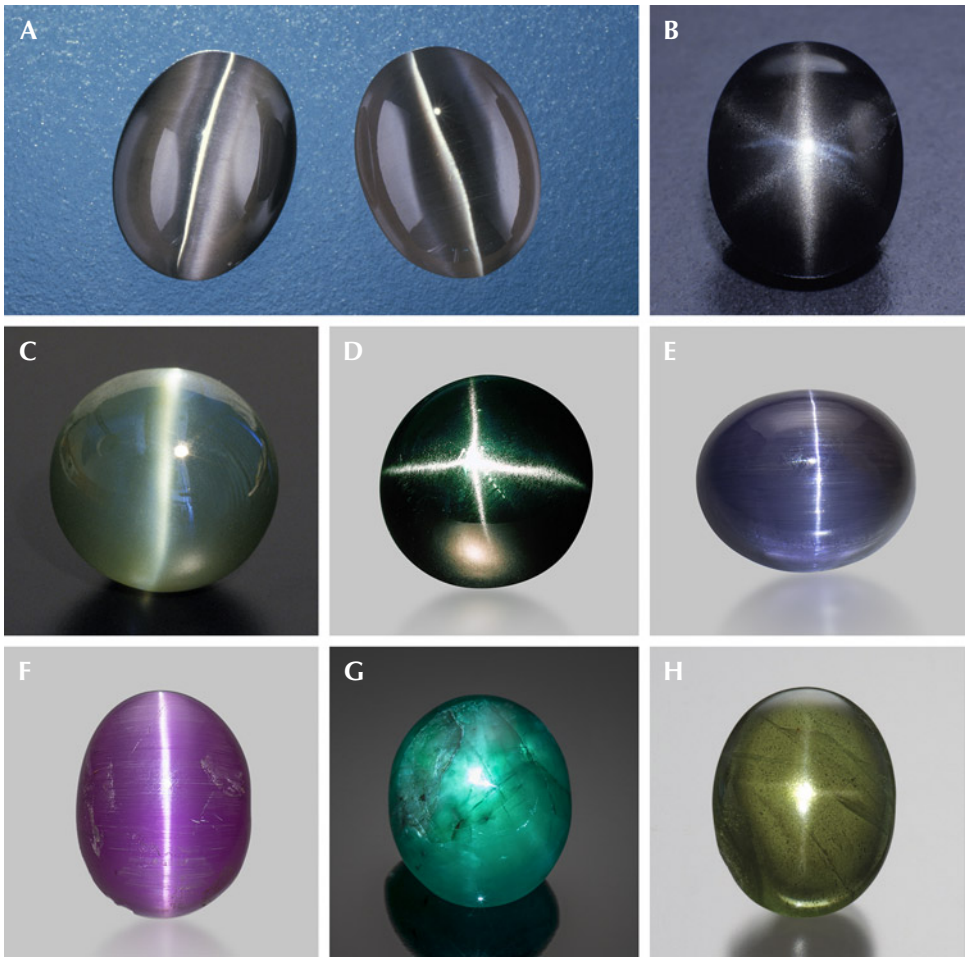

Figure 19. A. A 1.72 ct fiber-optic glass cabochon (left) looks visually identical to a 1.78 ct cat's-eye sillimanite (right). B: A black star scapolite. C: A 125.46 ct cat's-eye zircon. D: A four-rayed star diopside. E: A 2.69 ct cat's-eye tanzanite; courtesy of John I. Koivula. F: A 2.73 ct cat's-eye pezzottaite from Madagascar; courtesy of John I. Koivula. G: A 25.86 ct star emerald; courtesy of Manuel Marcial de Gomar. H: A 22.21 ct four-rayed star peridot. Photos by Shane F. McClure (A), Robert Weldon (B, G, and H), ICA (C), Mike Havstad (D), and Emily Lane (E and F).

requires only a near-perfect lattice match along one dimension, with the interfaces along the other two dimensions restrained to a very small scale by strain. Many defects generated during crystal growth or dissolution, such as growth tubes and etch channels, also have an oriented linear form, which may scatter light analogously to needle inclusions. In addition, some minerals—such as actinolite, hypersthene, sillimanite, and chrysotile—naturally adopt a columnar or fibrous habit similar to that observed in tiger's-eye. Therefore, chatoyancy and asterism may be observed in almost any mineral host included with fibrous minerals or defects (figure 19). Even diamond has been reported to show asterism (Watts, 2021). There have been attempts to list all the gemstones that are reported to display asterism or chatoyancy (Kumaratilake, 1997; Steinbach, 2016, 2018), which will not be repeated here. Because the star and cat's-eye effects can only be observed in a cabochon cut, it is highly probable that many chatoyant and asteriated minerals have not been discovered simply because no one has cut and polished them into a curved shape. In fact, many of the reported stars and cat's-eyes in gemstones are so weak that they are only observable under strong fiber-optic light, which may attract the attention of niche collectors, but probably would not be an eye-catcher in the general gem market. The columnar or fibrous texture is also easy to fabricate in glass and plastic by simply pulling and fusing together a bundle of optical fiber. Therefore, chatoyant glass (figure 19A, left) and plastic are very affordable imitations of cat's-eye gemstones of any color. Nonetheless, there is yet to be a convincing glass or plastic imitation for asterism, as the crystallographic symmetry is necessary to force the fibers into multiple directions.

AVENTURESCENCE IN GEMSTONES

The word *aventurine* derives from *a ventura* in Italian, meaning "by chance," originating from the glittering glass "avventurina," now known as "aventurine glass" or "goldstone" (figure 20A), which was allegedly invented by accident in eighteenth-century Italy (Moretti et al., 2013). The name was first adopted in mineralogy for quartzite (a metamorphic rock predominantly composed of polycrystalline quartz) containing glimmering mica crystals (figure 20B), although the best-known aventurescent mineral is aventurine feldspar. The term *aventurescence* is now used to describe the glittering effect created by isolated and visually discernible flat interfaces scattered in any transparent to translucent gemstone. Most aventurescence in gemstones is caused by oriented inclusions, and would appear as a sudden intense reflection (box E) that occurs only in certain directions, commonly known as schiller (Colony, 1935).

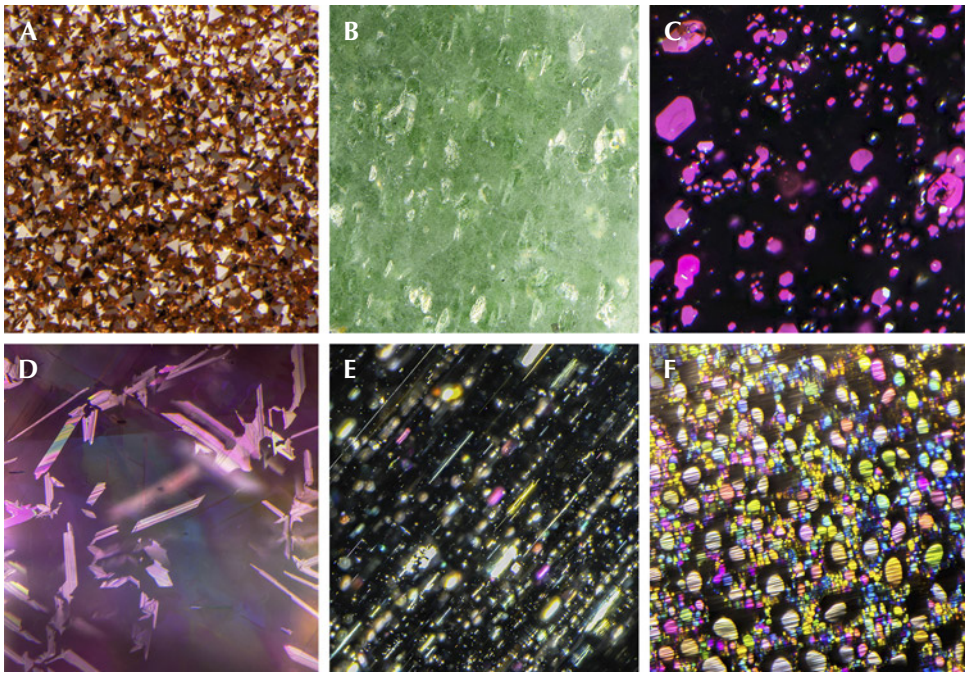

Figure 20. A: Triangular copper particles in goldstone glass. B: Glitters of fuchsite (Cr-muscovite) in aventurine quartz (quartzite). C: Flaky covellite (CuS) inclusions in a quartz crystal showing magenta color under reflected lighting. D: Flaky titanite (sphene) inclusions in a spinel crystal. E: Rectangular and needle inclusions in aventurescent aquamarine. F: Thin-film fluid inclusions in aquamarine. Photomicrographs by Nathan Renfro; fields of view 1.34 mm (A), 5.50 mm (B), 3.15 mm (C), 1.22 mm (D), 5.78 mm (E), and 2.36 mm (F). Courtesy of John I. Koivula.

Box E: Reflection of Light and Thin-Film Interference

When light is incident on a smooth interface between two optical media with different RIs, part of its energy reflects off the interface while the rest transmits through the material. The direction of the reflected light follows the law of reflection, with the reflected angle the same as the incident angle. The intensities of the reflected light rays follow the Fresnel equations and are functions of the incident angle, the relative RI between the two media, and the polarization of light. Generally, reflection is stronger with a larger relative RI. For incident light perpendicular to the interface, the reflectivity, or the fraction of energy reflected at the surface, equals:

$$\left(\frac{n_A - n_B}{n_A + n_B}\right)^2 \quad \text{(E-1)}$$

in which n_A and n_B are the RIs of the two media. The reflectivity also decreases with increasing glancing angle (angle between the incident light and the reflecting surface) (figure E-1).[1]

When two parallel interfaces are very close to each other, with the distance in between less than the wavelength of light, the light rays reflected from them interfere with one another and create colors. This process is commonly known as thin-film interference. The interference conditions depend on the RI of the film relative to the media around it (figure E-2) because the phase of the reflected light is shifted by 180° when traveling on the side with lower RI, but not when traveling on the side with higher RI. When the thin film is coated on the surface of a medium with higher RI, such as the antireflective coating on eyeglasses and binoculars or the tarnish layer on the surface of ore minerals, the phase change occurs at both surfaces of the thin film (figure E-2, left). Therefore, constructive interference occurs when the light reflected from the bottom surface of a thin film with thickness d travels one (or any integer multiple m) wavelength (λ) farther than the light reflected from the top surface:

$$2n_B d \sin \theta_B = m\lambda \quad \text{(E-2)}$$

On the other hand, if the thin film is sandwiched between the same medium, such as a soap film or a bubble in air, or film inclusions in transparent minerals, the phase change occurs only at the top surface (or only at the bottom surface if the RI of the film is lower than the surrounding medium) (figure E-2, right). In this case, constructive interference occurs if the optical path difference is half of the wavelength (or any odd integer multiples of the half wavelength):

$$2n_B d \sin \theta_B = (m - \tfrac{1}{2})\lambda \quad \text{(E-3)}$$

Interference colors also can be created by pairs of thin film layers periodically stacked on top of one another. This is much more complicated than simple thin-film interference because incident light is split at each interface and

[1]Glancing angle instead of incident angle is used in this article to maintain consistency with the other optical processes discussed.

Figure E-1. Schematic drawing of light rays reflecting off a flat interface, with reflectivity plotted as a function of the glancing angle (the angle θ between the incident light and the interface). When light is incident from the side with a smaller RI (red arrows from medium A), only a fraction of the energy reflects back (red curve on the graph), with the rest refracted through the interface. However, from the side with a larger RI (blue arrows from medium B), 100% of the energy reflects back at small glancing angles (total internal reflection, flat section of blue line on the graph) and only refracts through the interface at large glancing angles.

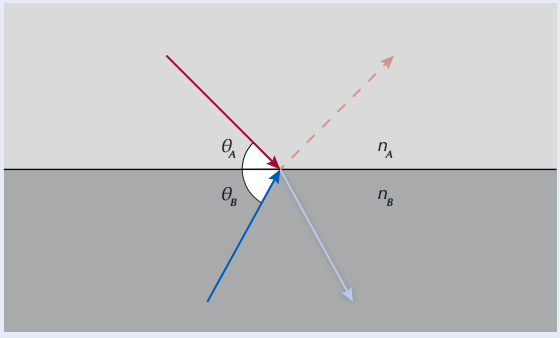

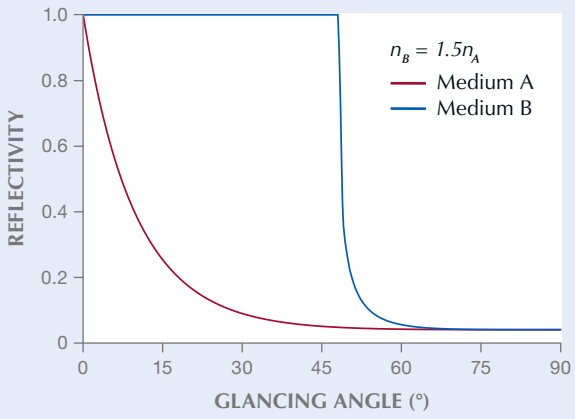

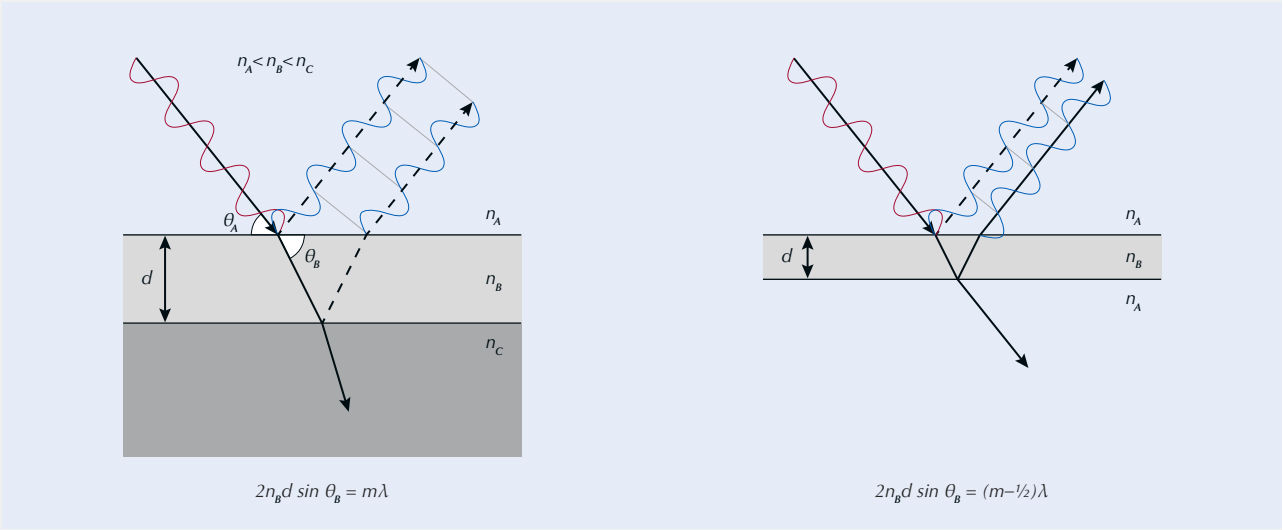

Figure E-2. Schematic drawing of thin-film interference between light reflected by two adjacent interfaces. Left: When the RI of the film is intermediate between the media above and below it, the light reflected by both interfaces changes its phase by 180°, resulting in a simple interference condition (equation E-2). Right: When the RI of the film is higher or lower than the media both above and below it, the phase change occurs only at one of the interfaces, and the required thickness for interference is halved (equation E-3).

reflected multiple times before exiting the material (figure E-3). This type of texture is known as a one-dimensional photonic crystal (periodic stacking in one direction). Qualitatively, it can be considered the summed effect of multiple thin-film interferences. For each pair of A-B layers, with respective RIs of n_A and n_B, the condition for constructive interference is:

$$2(n_A d_A \sin \theta_A + n_B d_B \sin \theta_B) = m\lambda \quad \text{(E-4)}$$

This equation models the interference among all solid (or dashed) reflected rays in figure E-3. At the same time, thin-film interference is generated within individual A (or B) layers (between solid and dashed rays in figure E-3):

$$2n_A d_A \sin \theta_A = (m'-½)\lambda \quad \text{(E-5)}$$

If both equations are satisfied, the reflected intensity is maximized, and the structure is known as an ideal multilayer, whereas if only the first equation (equation E-4 here) is satisfied, the reflected intensity is weaker, and the structure is called a non-ideal multilayer (Kinoshita, 2008).

Note that the interference wavelength (λ) is a function of the film thickness (d), the RI of the film (n_B), and the angle between the refracted light and the film surface (θ_B), which means that in theory the interference color should change with different incident angles. However, the RI of the interfering film is often much higher than that of air or the host mineral, so the range of θ_B is much smaller than θ_A. Moreover, the reflection is only strong enough to be observable at certain incident angles due to Fresnel's equations (figure E-1), further restraining the possible range of θ_B. This is partly why the interference color from thin films or multilayers in minerals often remains the same with changing viewing angles.

Figure E-3. Schematic drawing of multilayer interference. The interference condition can be approximated by thin-film interference of each periodic layer pair, and also by each individual layer.

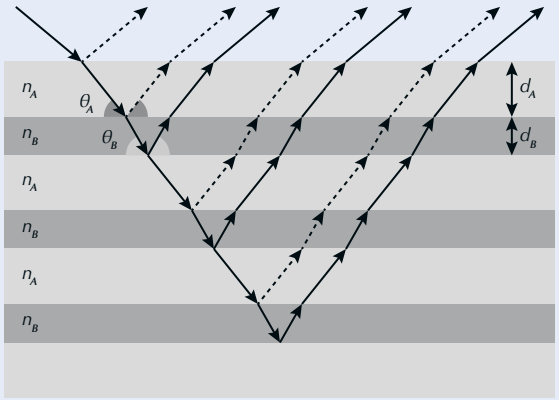

It should be noted that although less abundant than needle inclusions, flaky or thin-film inclusions are not uncommon in minerals (e.g., figure 20, C–F). Indeed, inclusions of any shape may have flat facets that reflect light. Almost all needles discussed above have a rectangular cross section with flat surfaces when examined with an electron microscope, which means light will be scattered preferentially perpendicular to the flat surfaces and create a schiller or sheen effect. The straight edges of some film inclusions, on the other hand, can also scatter light more randomly like a needle, creating chatoyancy or asterism in a cabochon-cut stone. It is not unusual for inclusions in a stone to vary in size and shape. As a result, the appearance of a stone, or the phenomenon it displays, depends greatly on how it is cut and polished.

COPPER SUNSTONE

Gem-quality aventurine feldspars are typically known as "sunstones" (Andersen, 1915), with mainly two types of reflective inclusions found in nature: metallic copper and iron oxides. Copper platelet inclusions in feldspars are rare and only have been reported in feldspar phenocrysts in certain basalts, as in the well-known Oregon sunstone. Similar material has also been reported from Ethiopia, but it shows a chemistry distinct from that of Oregon sunstone (Kiefert et al., 2019; Sun et al., 2020). The copper platelets are oriented along the cleavage planes of feldspar, mostly the (010) plane and less commonly the (001) plane (Farfan and Xu, 2008; Xu et al., 2017). Because the copper platelets are completely opaque, the color of the schiller arises only from the light reflected by the copper particles, which is reddish brown (figure 21). Copper sunstones may contain colloidal copper particles in addition to the platelets, resulting in red or blue-green bodycolors underneath the schiller (again, see figure 1 second from left in bottom row). As mentioned earlier, copper is known to diffuse quickly in feldspar crystals, which may be why the relatively fast cooling in volcanic rocks is necessary for them to precipitate as metallic particles instead of diffusing out of the crystal as the solubility of copper decreases in the feldspar. Nonetheless, the cooling rate of sunstone-bearing basaltic rocks is still much slower than in any experiments in a laboratory. It may take months to years for the basaltic lava to cool down from the melting temperature. This is why copper sunstone showing strong aventurescence has yet to be created in a laboratory, even though red and green colors have been produced relatively easily from copper diffusion (Jin et al., 2023).

HEMATITE SUNSTONE

Hematite sunstones are mostly found in granites or pegmatites and can be generally divided into two categories: orthoclase and sodic plagioclase (oligoclase or albite). They typically can be easily distinguished by

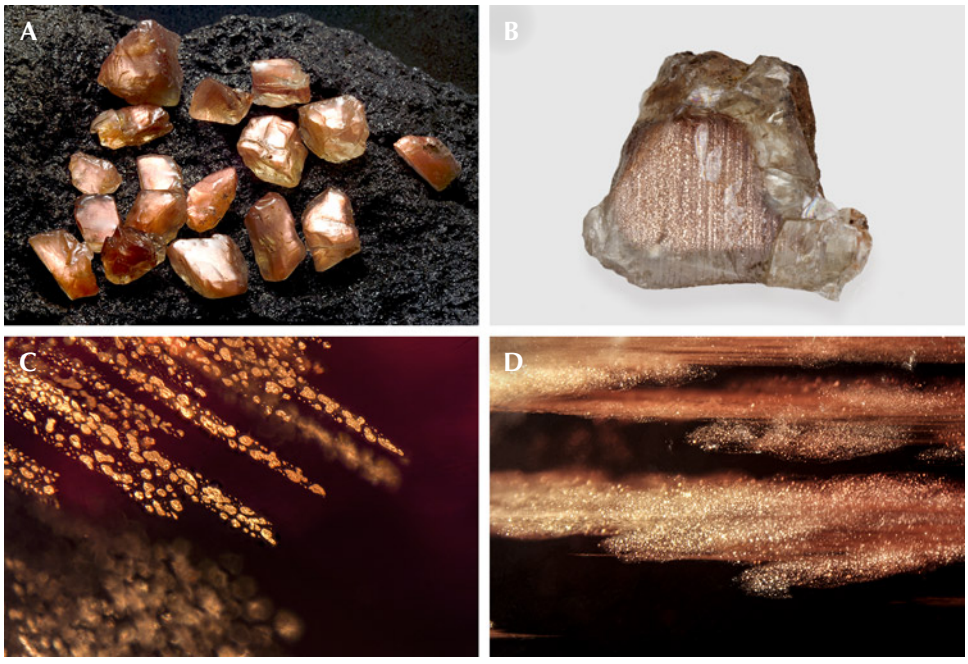

Figure 21. A: Rough Oregon sunstones showing strong schiller from copper platelets. B: A 20 ct rough Oregon sunstone from the Ponderosa mine. C and D: Copper platelets of different sizes and shapes in Oregon sunstone. Photos by Desert Sun Mining & Gems (A), Robert Weldon (B), and Rosie Young (C and D); fields of view 3.57 mm (C) and 5.14 mm (D).

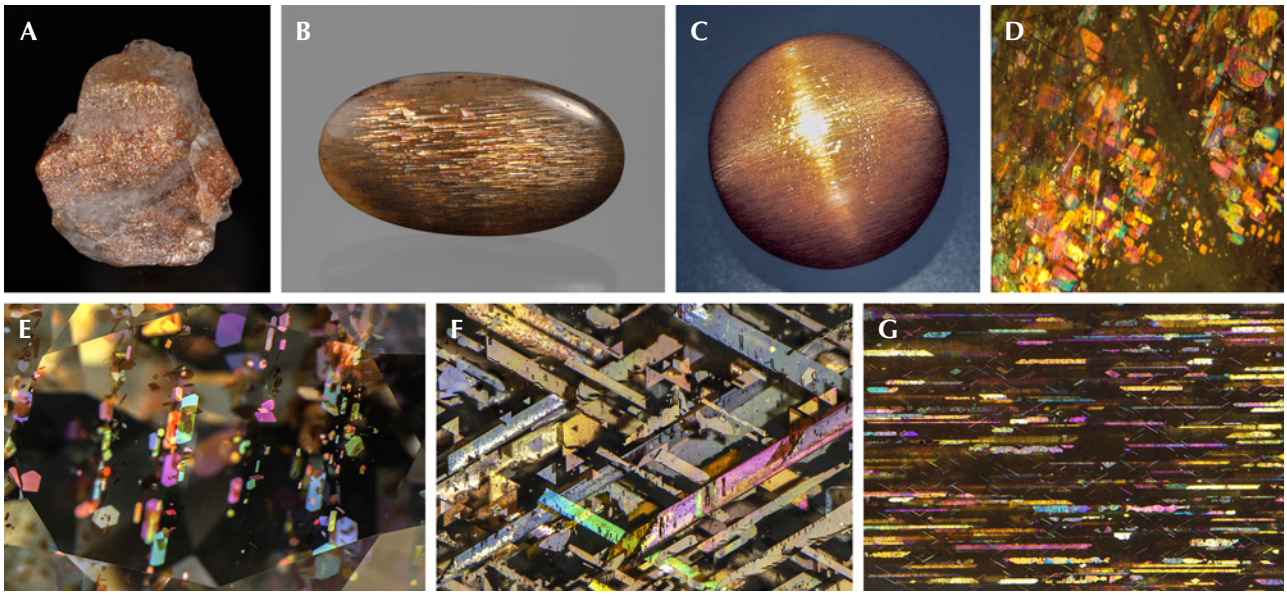

Figure 22. A: A 42.50 ct rough oligoclase sunstone reportedly from Tanzania. B: An 18.40 ct "meteor shower sunstone" cabochon from Tanzania. C: A 14.77 ct round orthoclase sunstone cabochon from Tanzania showing a four-rayed star. D: Iridescent reflection from hematite inclusions in a Canadian labradorite due to thin-film interference. E: Hematite platelets in an oligoclase "confetti sunstone" from Tanzania; courtesy of John I. Koivula. F: Thin-film magnetite and hematite blades elongated along the ⟨011⟩ directions in an orthoclase rainbow lattice sunstone from Australia. G: Thin-film iridescent hematite blades elongated along the [010] directions in an orthoclase sunstone from Tanzania, along with some tiny needles along the ⟨011⟩ directions. Photos by Emily Lane (A), Annie Haynes (B), Maha Tannous (C), Shiyun Jin (D), and Nathan Renfro (E, F, and G); fields of view 2.2 mm (D), 9.56 mm (E), 6.39 mm (F), and 7.20 mm (G).

the shape and orientation of the hematite films. Sodic sunstone, mostly oligoclase, such as the most studied examples from Tvedestrand, Norway (Andersen, 1915; Divljan, 1960; Neumann and Christie, 1962; Kraeft and Saalfeld, 1967; Copley and Gay, 1978, 1979, 1982), contains rectangular and hexagonal hematite plates along the (112), (11$\bar{2}$), (150), and (1$\bar{5}$0) planes. Due to the triclinic symmetry of plagioclase feldspar, the hematite plates are oriented askew relative to the cleavage planes (figure 22, A, D, and E). Orthoclase sunstones, such as those from Tanzania (Hänni et al., 2003) and Australia (Koivula and Kammerling, 1989), on the other hand, tend to have long hematite blades parallel to the (100) plane and extended along the [010] or ⟨011⟩ directions of the feldspar (figure 22, B, C, F, and G), which are always symmetrical around the cleavage planes (Jin et al., 2022b). These elongated inclusions often create chatoyancy or asterism when cut into a cabochon (Hyrsl, 2001; Hänni et al., 2003). Smaller hexagonal or triangular flakes parallel to the (100) and (102) planes are also common in lower-quality orthoclase sunstones (Liu et al., 2018; Jin et al., 2022b).

Unlike the metallic black color of large hematite crystals, the hematite film inclusions in sunstones are transparent with orange to deep red colors depending on their thicknesses, yielding what appears to be an orange to red bodycolor. The transparent hematite flakes in sunstones are sometimes misidentified as biotite by those who are not familiar with their transparent appearance (Lee and Parsons, 2015). The thinner hematite inclusions can also create iridescent colors due to thin-film interference (figure 22, D–G), primarily observable only with an optical microscope.

The process that creates the hematite flakes in sunstones takes much longer than the process that creates the copper platelets, as indicated by the different types of rocks they are found in. The mechanism that produces the hematite flakes is still not well understood, with several hypotheses proposed over the past two centuries (Smith and Brown, 1988, pp. 638–639). Simultaneous crystallization was the first to be rejected because hematite flakes are not oriented along the common growth faces of feldspar (Andersen, 1915). Precipitation of iron from the feldspar lattice is the simplest theory, but this

explanation poses the question of why some feldspars with exceptionally high iron content remain hematite-free. Another hypothesis is that reaction with the surrounding fluid introduces iron into the feldspar crystals, but it does not explain how the imported iron is transported and precipitated as hematite flakes inside the feldspar. A recent study of rainbow lattice sunstone from central Australia showed that the hematite films in orthoclase sunstone were originally magnetite (Mag: Fe_3O_4) films that were oxidized at a later stage (Jin et al., 2022b). Rainbow lattice sunstone is a unique sunstone with exceptionally large magnetite and hematite "blades," creating a rainbow lattice effect resulting from the thin-film interference of light reflected by hematite films (figure 22F). Only the thinner parts of the magnetite films have been oxidized to hematite, showing light yellow to orange colors in transmitted light and pink to blue iridescence under reflected light. The magnetite films, crosscutting the plagioclase lamellae exsolved from the orthoclase matrix, clearly represent precipitation of iron dissolved in the feldspar lattice, likely due to decreasing oxygen fugacity. The orientation of the magnetite films, like the other oriented precipitates in mineral crystals such as star sapphire, is a result of minimization of the surface energy by finding the interface with the best lattice match. The same mechanism should apply to other orthoclase sunstones, such as those from Tanzania and the United States (North Carolina) (Hänni et al., 2003; Choudhary, 2008; Challener et al., 2017), based on the similar appearance and orientation of the hematite films. The only difference is that all of the precipitated magnetite films in the other orthoclase sunstones have been oxidized to hematite due to their smaller and thinner sizes. However, it is not clear whether this process can be expanded to the sodic plagioclase sunstones, as those hematite flakes are typically thicker (darker red color with less iridescence) with more pristine hexagonal forms.

CLOUDED FELDSPAR

Although only a small proportion of included feldspars qualify as sunstones, crystallographically oriented needle-like iron oxide inclusions are almost ubiquitous in plutonic and metamorphic plagioclase feldspars (e.g., figure 23A). Feldspars containing dense iron oxide needles, also known as clouded feldspars

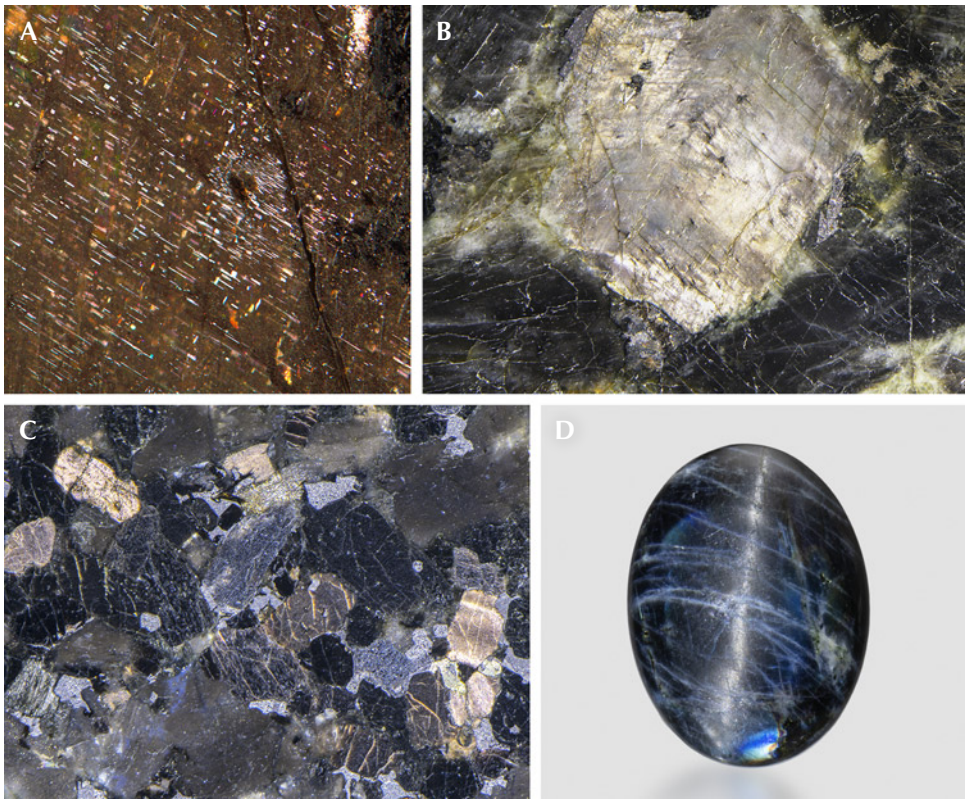

Figure 23. A: Oriented needle inclusions in a labradorite from Ukraine (commercially known as "Volga Blue"). B: A labradorite crystal in a polished anorthosite slab (Volga Blue) showing silver sheen at a different angle from iridescence. C: Labradorite crystals in a gabbro slab from India (commercially known as "black galaxy") showing golden sheen from oxidized magnetite needles. D: A 14.54 ct labradorite cabochon showing chatoyancy. Photos by Shiyun Jin (A), Nathan Renfro (B and C), and Emily Lane (D); fields of view 4.76 mm (A), 36.5 mm (B), and 9.7 mm (C).

(Smith and Brown, 1988, p. 639), display black, dark gray, or brown colors with an almost opaque appearance. A silver (or less commonly golden) sheen can often be observed on the polished surfaces of these clouded feldspars, which makes their host gabbro or anorthosite rocks popular countertop materials (figure 23, B and C). When cut into cabochons, clouded feldspar can display a cat's-eye (or star) effect as expected (figure 23D). However, cat's-eye (or star) plagioclase feldspars rarely appear in the gem market, mostly because the quality of the chatoyancy or asterism is generally not attractive enough by itself to be worth the cost of careful cutting and polishing.

Due to their geological importance in the study of magmatic and metamorphic processes, as well as the historical evolution of Earth's magnetic field, the needle inclusions in plagioclase feldspar have been studied extensively compared to the other oriented inclusions found in minerals, providing important insights into how they formed. Combining optical microscopy, EBSD, and TEM analysis has revealed multiple types of magnetite needles with different CORs to the host feldspars (Bian et al., 2023 and references therein). Most observations suggest that these needles form by precipitation of iron that was originally dissolved in the feldspar structure, perhaps due to interaction with a reducing fluid (Bian et al., 2021). The crystallographic orientations of the magnetite needles likely resulted from the minimization of both interfacial energy and atomic rearrangement. Interestingly, the needle inclusions seem to appear only in more calcic plagioclase feldspars (andesine, labradorite, bytownite, and anorthite), whereas the thin-film and platy iron oxide inclusions (hematite or magnetite) are primarily found in sodic plagioclase and alkali feldspars (oligoclase, albite, and orthoclase) (Jin et al., 2022b), although both types of inclusions have been observed in labradorite from Canada (figure 22D) (Jin et al., 2021). Several factors might contribute to this different morphology of iron oxide inclusions, including lattice parameters and crystal structures, anisotropic diffusion of iron, and thermal and redox histories.

GOLDEN SHEEN SAPPHIRE

Another example of gemstones displaying both asterism and aventurescence is gold sheen sapphire (or Zawadi sapphire) reportedly from Kenya (figure 24, left), yet the exact location of the mine is still unclear (Bui et al., 2015; Soonthorntantikul et al., 2016). Although most star sapphires can display a weak shimmer or sheen on a flat polished (001) surface, gold sheen sapphire shows a much stronger aventurescence, comparable to that of sunstone. A facet-grade aventurescent sapphire, with an appearance resembling Oregon sunstone's schiller (figure 24, right; Sripoonjan et al., 2019), was also reported with a Kenyan origin, although it may not be from the same mine as the typical translucent to opaque material. And obviously, gold sheen sapphire also displays very strong asterism in a cabochon cut (Bui et al., 2015; Miura et al., 2018). Most inclusions in gold sheen sapphire are the typical acicular hematite and ilmenite as in most star sapphires but noticeably denser in number (again, see figure 8C). Many of these hematite and ilmenite inclusions also expand into flaky shapes, sometimes with irregular edges, which further enhances their reflectivity. Dark platy magnetite inclusions with triangular or rhombic shapes, like those observed in rainbow lattice sunstone, are also found in gold sheen sapphire (Bui et al., 2015;

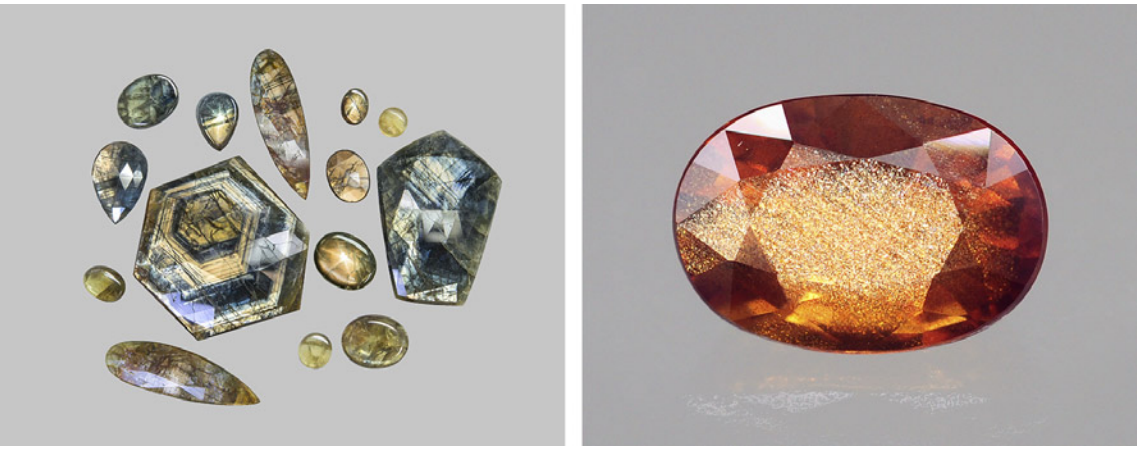

Figure 24. Left: Gold sheen sapphires from eastern Kenya (largest 97.69 ct). Photo by Lhapsin Nillapat. Right: A 4.34 ct faceted transparent orange sapphire showing a golden sheen effect. Photo by Tasnara Sripoonjan; courtesy of the Gem and Jewelry Institute of Thailand.

Narudeesombat et al., 2018) and have not been reported in other star sapphires. The occasional goethite inclusions are likely from late-stage alteration of hematite and magnetite, as much gold sheen sapphire material is severely fractured. Unsurprisingly, the iron concentration in gold sheen sapphire is on the higher end for natural sapphire, but there is nothing unusual about the trace element chemistry of these stones (Miura et al., 2018; Narudeesombat et al., 2018; Sripoonjan et al., 2019). The flaky iron oxide inclusions with irregular edges parallel to the (001) plane strongly suggest solid-state precipitation of oversaturated iron from the corundum lattice instead of epitactic crystallization during crystal growth, because most gold sheen sapphire material shows obvious hexagonal {110} growth zoning parallel to the *c*-axis. These sapphires may have experienced some special thermal and redox histories that promoted the precipitation of iron, and further investigation is warranted. It should be noted that there is most certainly a marketing bias for these heavily included sapphires, because the more common black star sapphires from Thailand, Cambodia, or Australia can also display a strong golden sheen on flat polished surfaces but are never noted for their aventurescence. Nonetheless, since the name *gold sheen*[3] is more closely associated with the Kenyan material, perhaps the more general term *golden sheen sapphire* could be used for heavily included sapphires of unclear origins that display a strong golden aventurescence.

SHEEN AND IRIDESCENT OBSIDIAN

Some obsidian glasses display a diffuse sheen due to reflections from aligned inclusions, which sometimes qualify as aventurescence. Depending on the color of the reflection, they are commonly referred to as silver sheen obsidian or gold sheen obsidian (figure 25, A and B; videos 4 and 5). Some obsidian, often called rainbow or fire obsidian, can display a wide range of iridescence (figure 25, C–F; Johnson and Koivula, 1997). Unfortunately, despite the availability of this material, studies of these included volcanic glasses are extremely limited, providing little information on the mechanism creating the optical phenomenon. Obsidian is an amorphous solid formed by rapid quenching of siliceous melts, an extremely fast process far from equilibrium, and it is therefore more difficult to determine the parageneses of the inclusions in obsidian relative to those for crystalline mineral hosts that are mostly controlled by thermodynamics. Lenticular features filled with gas or glass of a different composition, flattened and aligned due to the flow of the silicic melt, along with oriented pyroxene or feldspar crystals, have been reported in samples of Mexican obsidian, which can contribute to the sheen from internal reflections (Ma et al., 2001). Thin layers measuring 300 to 700 nm thick filled with nano-size magnetite crystals observed in fire obsidian from Glass Buttes, Oregon, may cause thin-film interference and explain the rainbow colors (Ma et al., 2007). A recent study showed that these aligned inclusions in obsidian can not only produce special optical effects but also create complex magnetic properties in these natural glasses (Mameli et al., 2016). Given the dramatically different appearances of sheen obsidians from different locations, multiple mechanisms could be involved in creating these optical phenomena.

IRIDESCENCE IN FELDSPARS

Iridescent feldspars are the most studied phenomenal gemstones, mainly due to their accessibility and geological importance. Prominent physicists Robert Strutt, fourth Baron Rayleigh (son of third Baron Rayleigh, who discovered Rayleigh scattering) and C.V. Raman (who discovered Raman scattering) both investigated these spectacular phenomenal stones during their careers (Strutt, 1923a; Raman, 1950a; Raman and Jayaraman, 1950, 1953a). The amount of research on this subject could easily constitute a separate review article on its own. Only the results of the studies that are most relevant to the gemological and optical properties of iridescent feldspars will be summarized in this section.

Iridescent feldspars generally can be separated into three categories based on their bulk chemical composition: labradorite, peristerite, and moonstone (figure 26), all of which owe their optical phenomena to submicron intergrowth textures resulting from solid-state exsolution (figure 27). Because oriented iron oxide inclusions are so common in feldspars, iridescent feldspars often also display aventurescence at a different orientation (figure 22). In fact, uniform golden aventurescence in some sunstones can appear quite similar to yellow/orange iridescence in labradorite (figure 23).

[3]At the time of writing, "Gold Sheen" is a refused and abandoned trademark application (#87535320) by the United States Patent and Trademark Office, although it (or its translation) may be a valid trademark in some other markets.

Figure 25. A: A 7.26 ct golden sheen obsidian from Mexico. B: A 6.95 ct silver sheen obsidian from Mexico. C: A 7.69 ct cat's-eye obsidian from Mexico. D: A 54.32 ct fire obsidian fashioned by Tom Dodge. E: A 14.7 g "velvet" obsidian from Mexico. F: A rainbow obsidian showing layers with different iridescent colors. Note that only A and B are considered aventurescent due to the eye-visible reflective inclusions, whereas the sheen in C–F is not created by visually discernible structures. Photos by Annie Haynes (A–C), Robert Weldon (D), and Emily Lane (E). Courtesy of John I. Koivula (A–C) and Rocks for the Spirit (F).

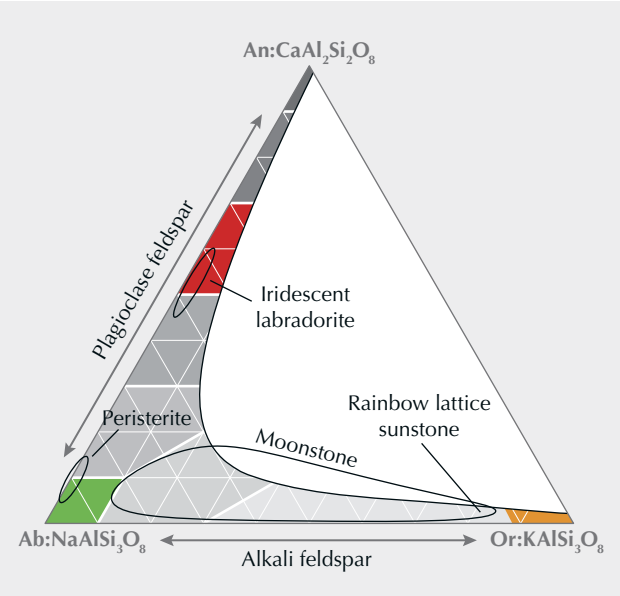

*Figure 26. Ternary diagram of the feldspar group minerals, with the composition ranges of three different types of iridescent feldspars circled. The chemical ranges of labradorite s.s. (*stricto sensu*), albite s.s., and adularia are highlighted in red, green, and orange, respectively.*

To avoid confusion, Smith and Brown (1988, p. 20) tried to redefine the term *schiller* to be reserved only for reflections from visible inclusions, as in aventurescence. Unfortunately, such an attempt to change the definition of a long-used term is unlikely to be widely adopted, especially since the term has been equally (if not more) commonly used for iridescence than for aventurescence (e.g., Colony, 1935). In this article, "schiller" is defined as any specular reflection arising from within a crystal, either because of flaky inclusions or exsolution lamellae, as long as it is strongly directional.

Iridescent Labradorite. The term *labradorite*, without any modification, refers to any plagioclase feldspar with a composition between An_{50} (50 mol.% anorthite and 50 mol.% albite) and An_{70} (70 mol.% anorthite and 30 mol.% albite) (figure 26). For instance, most Oregon sunstones are labradorites. The name *labradorite* originated from its type locality, Paul's Island in Labrador, Canada, which produces the most famous iridescent variety. Iridescent labradorites are found around the world in plutonic rocks that experienced extremely slow cooling or high-grade metamorphism, with bulk compositions between $An_{46\pm2}$ and $An_{60\pm2}$ (Ribbe, 1983; Smith, 1983). These crystals can grow to exceptionally large sizes, sometimes up to several decimeters. Anorthosite rocks composed of iridescent labradorites

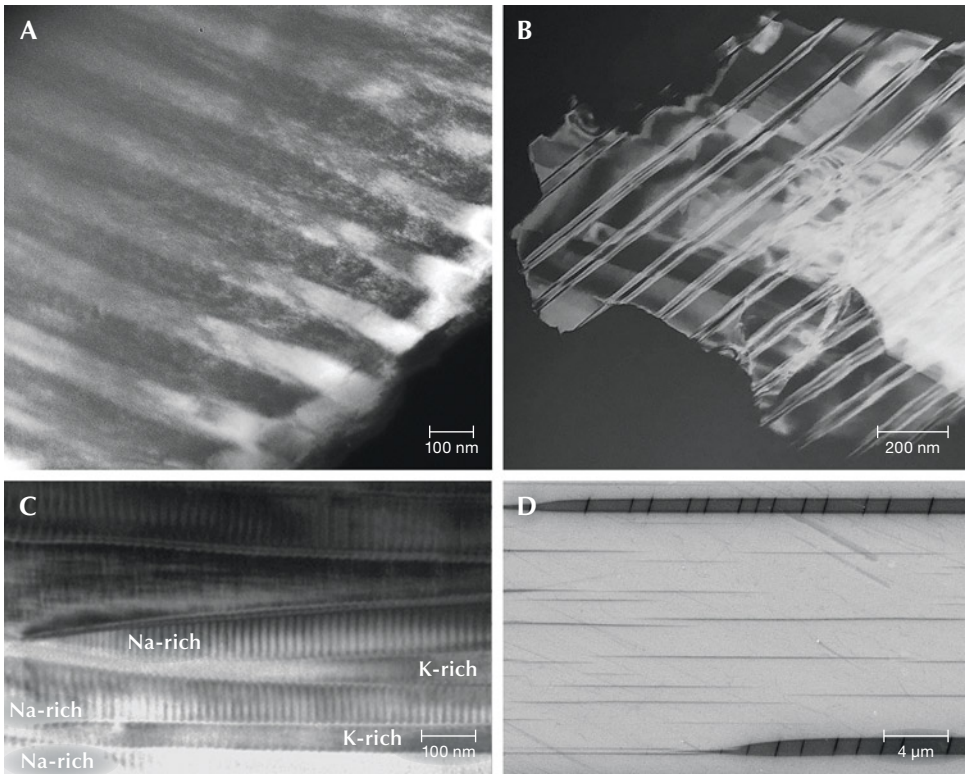

Figure 27. A: Darkfield TEM image of labradorite from Canada with blue iridescent color. B: Darkfield image of peristerite with blue iridescent color from the U.S. state of Virginia. C: Brightfield image of moonstone with greenish yellow iridescence. D: SEM image of the (010) cleavage surface of rainbow lattice sunstone from Australia. Images by Seungyeol Lee (A) and Shiyun Jin (D); images B and C courtesy of Huifang Xu.

are often used as high-end countertop materials. The best-quality iridescent labradorites are found in Canada, Finland, and Madagascar.

The exsolution texture in iridescent labradorite, known as the Bøggild intergrowth, is composed of alternating wider calcic lamellae (~70–200 nm) and thinner sodic lamellae (~50–100 nm), which are mostly oriented parallel to the $(\bar{3}\ 20\ 2)$ plane (Bøggild, 1924), making the iridescence observable on the (010) cleavage surface. The iridescent color correlates with the average thickness of the lamellae, such that a total thickness of adjacent calcic and sodic lamellae of ~150 nm yields blue iridescent colors, >250 nm yields red iridescent colors, and a continuous prismatic spectrum is observed in between (Ribbe, 1983). The periodicity of the Bøggild intergrowth is very regular (figure 27A) compared to exsolution textures in other minerals, so the iridescence of labradorite is almost always intense with high saturation (figure 28). As a result, the iridescent spectrum can be predicted using a relatively simple kinematic theory of light reflection (Bolton et al., 1966), and the appearance rendered by computer modeling of the iridescence is quite realistic with only a few parameters (Weidlich and Wilkie, 2009).

Although labradorites with the same iridescent color from different locations can have different compositions, the iridescent color zones within the same crystal are always directly correlated with the composition, with the red iridescent zone ~2–3 mol.% more calcic than the blue iridescent zone (Jin et al., 2021). Because of this high sensitivity to small chemical variations, the iridescent color zones in labradorite often feature straight, sharp boundaries (figure 28, A–D), which are not observed in other iridescent feldspars. This characteristic is interpreted to reflect the special

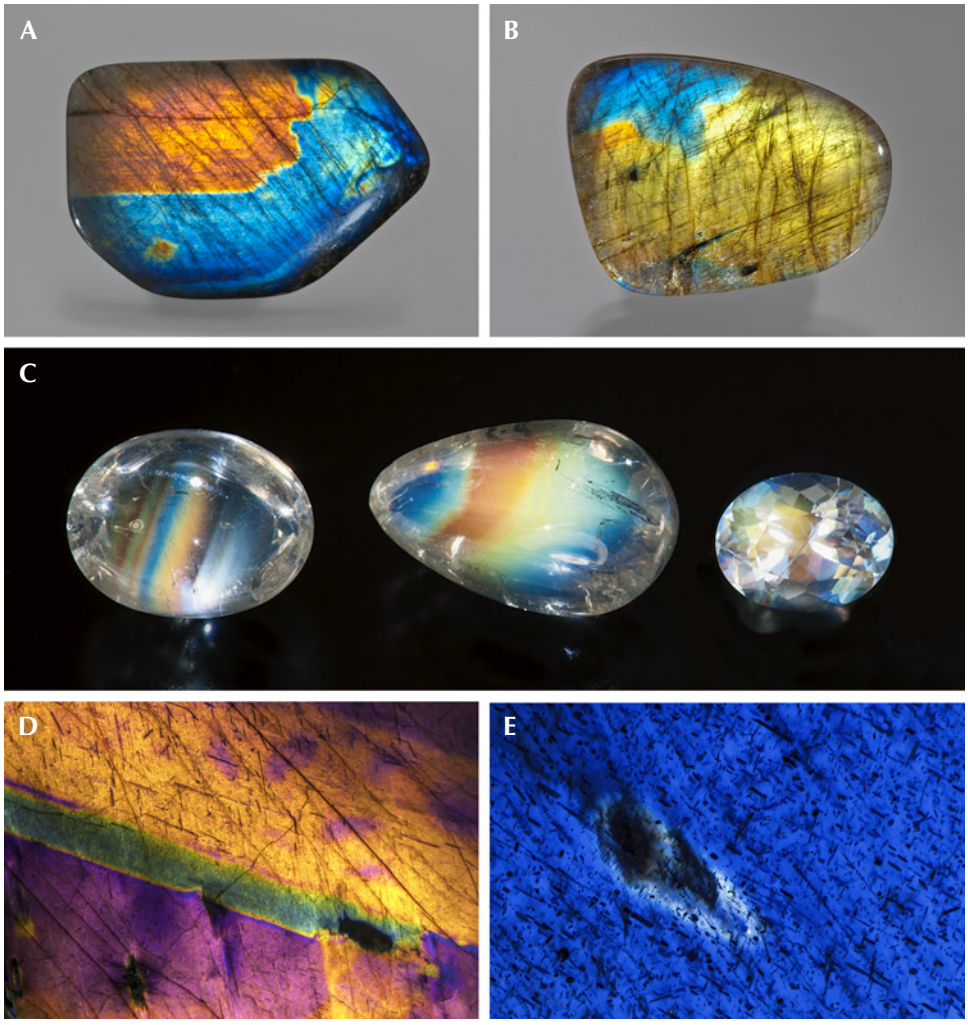

Figure 28. A and B: Labradorite from Finland (28.05 × 42.66 mm) and Madagascar (23 × 35 mm), respectively, showing iridescence close to the surface; courtesy of Black Star Trading Company. C: The iridescence of Zambian "rainbow moonstone" labradorite (largest 2.82 ct) comes from much deeper inside the stone due to its high transparency; gift of Scott Davies. D: Labradorite from Finland is heavily clouded with opaque inclusions that block light from traveling deep into the crystal, so the iridescence appears as a coating on the surface. E: Higher magnification reveals that the opaque inclusions are floating over the blue iridescence, indicating that the interference color always arises from inside the labradorite crystal. Photos by Robert Weldon (A–C) and Nathan Renfro (D and E); fields of view 18.8 mm (D) and 5.05 mm (E).

shape of the miscibility gap creating the Bøggild intergrowth, which is an inclined loop that closes at low temperature (Jin et al., 2021). Nonetheless, the exact shapes or even topologies of the Bøggild intergrowths are still not fully resolved, mainly due to the challenges of accurately analyzing the composition of individual lamellae, as well as the limited numbers of samples studied in detail (Jin et al., 2021).

The bodycolor of iridescent labradorite is mainly determined by the density of iron oxide inclusions, as most calcic plagioclases from plutonic rocks are clouded. The darkness of labradorite can dramatically affect the appearance of iridescence by controlling the depth of the light reflected by the lamellae inside the crystal. Spectrolite from Finland, with a nearly black bodycolor, shows iridescence at the surface of the crystal (figure 28, A and D), whereas "rainbow moonstone" labradorite with almost no iron oxide inclusions (Koivula, 1987; Win and Moe, 2012) shows diffuse iridescence coming from deeper inside the crystal (figure 28C), resulting in an appearance that may be confused with moonstone, as suggested by its name.

Peristerite. Peristerite is the least-known iridescent feldspar, and it is nearly always misidentified as moonstone due to their similar appearances. Technically, peristerites are sodic plagioclases with bulk compositions between An_2 and An_{16} that have exsolution textures. Only sodic plagioclase from a pegmatite with a composition ranging from An_5 to An_{13} can develop exsolution lamellae coarse enough to cause multilayer interference of visible light and create iridescent colors (Ribbe, 1983). The name *peristerite* comes from *peristera*, Greek for "pigeon," for its resemblance to the iridescent colors of a pigeon's neck feathers. The unmixing is driven by the aluminum-silicon ordering in the pure albite structure as it transitions from "high albite" (disordered aluminum-silicon framework) to "low albite" (fully ordered aluminum-silicon framework) below 600°C (Smith, 1983). As a result, pure low albite (~An_0) is the dominant phase in peristerites, with intergrowths of minor oligoclase (~An_{20}). The best-known peristerite location is Ontario, Canada. The iridescence of peristerite is mostly light blue, with light yellow and pink iridescence also occasionally observed. The peristerite exsolution lamellae are generally oriented parallel to the $(0\bar{8}1)$ plane (Ribbe, 1983), similar to Bøggild intergrowths, with the iridescence also observable on the (010) cleavage surface (figure 29). Although its light bodycolor and desaturated iridescence may resemble moonstone, peristerite can be easily identified by the presence of polysynthetic Albite-twin lamellae, as well as by the orientation of the iridescence.

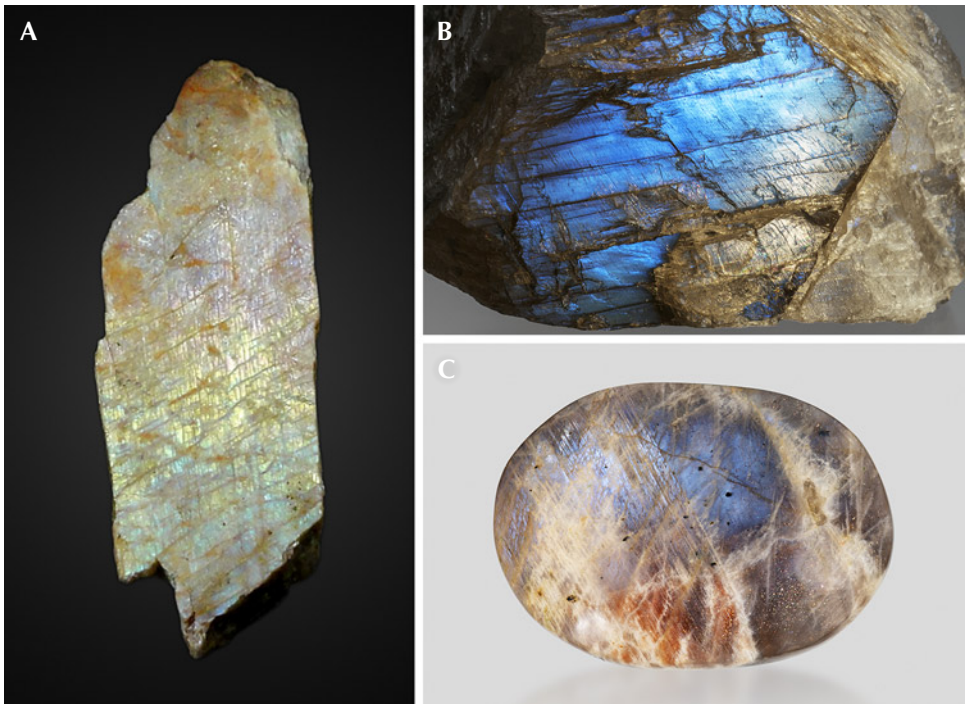

Figure 29. A: A peristerite from Ontario, Canada (7 cm long), showing pink, yellow, and green iridescence; courtesy of GIA Museum, collection no. 32588. B: Clear peristerite from Tanzania (677 g) showing light blue iridescence on the (010) cleavage surface; gift of Lithos Africa. C: A polished peristerite from Tanzania (7.5 cm long) that also displays aventurescence from hematite platelet inclusions; courtesy of Rachelle Turnier. Photos by John Montgomery (A) and Emily Lane (B and C).

Figure 30. A: Moonstone cabochons of various colors from India (113.79 carats total); in memory of Dr. Frederick H. Pough. B: An iridescent anorthoclase in larvikite from Norway (commercially known as "blue pearl"). C: A 2.6 cm long rough moonstone fragment from the U.S. state of Wisconsin, showing strong blue iridescence. D: A rainbow lattice sunstone from Australia showing white iridescence. E: Three cat's-eye moonstones (left to right: 13.1, 6.36, and 6.08 ct) exhibiting chatoyancies of different sharpness; right stone gift of Beverly J. Bystricky, courtesy of GIA Museum, nos. 22154, 38696, and 39155. F: A four-rayed star moonstone (17.3 ct) from Madagascar; courtesy of GIA Museum, collection no. 19470. Photos by Emily Lane (A, B, and F), Shiyun Jin (C and D), and Orasa Weldon (E).

Moonstone. Moonstone is named after its white or silver iridescent glow that resembles moonlight. Only cryptoperthite, an alkali feldspar with nonperiodic submicron intergrowth textures between albite and orthoclase, can produce such desaturated iridescence and be called "moonstone." Unfortunately, the name has been haphazardly applied to any light-colored feldspars, such as peristerite or transparent labradorite, that display a diffuse or desaturated iridescence, which has added confusion to an already complicated subject. Although light bodycolors are the most common, a wide range of different colors and shades can be found in moonstones, mostly determined by the types and densities of inclusions (figure 30).

Unlike the multiple discrete miscibility gaps of the plagioclase series between albite and anorthite, the alkali feldspar solid solution between albite and orthoclase has only one large miscibility gap. Despite its simple topology, the wide composition range of this solvus results in more intricate intergrowth textures in alkali feldspars, with lamellar thicknesses ranging from a few nanometers to several millimeters. The lamellar textures are further complicated by the composition-dependent order-disorder phase transitions and the resulting twin structures. Many book chapters and review articles have been dedicated to this subject (Yund, 1983, 1984; Parsons and Brown, 1984, 1991; Parsons et al., 2015). Although the submicroscopic exsolution textures responsible

for the iridescence of moonstone have been extensively studied using electron microscopy, their direct correlations with the iridescent colors have not been carefully investigated.

Depending on the composition and thermal history, a menagerie of widely different textures has been reported in moonstone. Alkali feldspars with intermediate compositions (~$Ab_{80}Or_{20}$–$Ab_{40}Or_{60}$) start with spinodal decomposition that creates alternating albite and orthoclase lamellae with flat interfaces nearly parallel to the ($\bar{6}01$) plane (figure 27C), which over time can evolve to wavy and zigzag boundaries along the ($\bar{6}\bar{6}1$) planes to minimize the elastic strain at the interface. Further coarsening of the texture may result in isolated domains of albite with lozenge-shaped cross sections (Yund, 1983). These moonstones typically show blue iridescence with various degrees of saturation (e.g., figure 30C), although light yellow iridescence has also been occasionally observed.

Alkali feldspars with more potassic compositions develop a different texture when they exsolve. Because their compositions fall outside the range for spinodal decomposition, it is only possible for them to exsolve through nucleation and growth of albite lamellae from the orthoclase matrix. As a result, the albite lamellae occur as isolated thin films (or thicker "spindles") parallel to the ($\bar{6}01$) plane (Parsons et al., 2015), which can create iridescence through thin-film interference (Jin et al., 2022b). However, unlike the hematite films in sunstones with parallel faces and constant thickness, the albite films are lens-shaped, thicker in the middle and tapering out at the edges (figure 27D). Therefore, the thickness of the albite films covers a continuous range from zero to a few hundred nanometers, causing thin-film interference over the entire visible spectrum and thereby creating a bright white iridescence (figure 30D). Sodic alkali feldspars may behave similarly to potassic feldspars, except with orthoclase thin films exsolving from an albite matrix. However, high-quality sodic moonstone is relatively rare, partly due to the complications related to the lower symmetry and the more calcic composition.

Because of the wide miscibility gap and faster interdiffusion rate between albite and orthoclase, the individual lamellae or domains in moonstones are always close to the end-member compositions. The larger chemical difference between lamellae means a larger disparity in RIs, creating stronger reflection and scattering at the interfaces (again, see equation C-1 and figure E-1). The more distinct crystal structures also create strong strains at the interface, making them vulnerable to low-temperature fluid-induced alterations. This is why moonstone almost always has a milky translucent appearance, with the iridescence shallow beneath the surface (figure 30). The most extreme case is the anorthoclase in larvikite (figure 30B), which is often misidentified as labradorite due to its darker bodycolor. Moonstone's milky appearance often leads to the misconception that its iridescent sheen is caused by Rayleigh or Mie scattering, similar to opalescence (Cartier, 2009), instead of interference of light reflected by lamellar structures. In contrast, with much smaller chemical and RI differences between lamellae, inclusion-free labradorite and peristerite can appear crystal-clear with iridescence coming from much deeper inside the crystal (figures 28C and 29B, respectively).

In gemology, moonstone's iridescence is called adularescence. Unfortunately, this term presents some issues that often lead to confusion. First, it incorrectly implies relevance to adularia, a low-temperature variety of almost pure potassic feldspar (defined by a unique rhombic crystal habit; figure 26), which never[4] displays adularescence (e.g., Tutton, 1921). "Adularescence" did not appear in any academic mineralogical literature on feldspars until very recently (Jin et al., 2022b), making it impossible to trace its origin. Perhaps "perthescence" after perthite would have been a more proper name, following a similar logic as labradorescence and peristerescence, but feldspar mineralogists have adopted the more general term *iridescence*.

Second, the character of iridescence in moonstone is highly variable, and some more saturated iridescent colors may look similar to peristerite and labradorite (figure 30C). The diverse appearance of moonstone iridescence has misled some to incorrectly associate the name with a light bodycolor instead of the moonlight-like glow. Consequently, "adularescence" is often applied to peristerite and light-colored labradorite, likely because "moonstone" is much more marketable than some iridescent plagioclase with an obscure name. This unrestricted and often confusing usage of the name *moonstone* created strange trade names such as

[4]It may be theoretically plausible for a highly sodic adularia formed in extremely unusual conditions to develop exsolution textures and become a moonstone, but to the best of the authors' knowledge at the time of writing, no such material has been reported. This incorrectly implied relevance between moonstone and adularia might be the reason for a common misconception that all moonstones are orthoclase feldspars.

TABLE 1. Comparison of the properties of various iridescent feldspars.

	Labradorite	Peristerite	Moonstone
Chemical composition	$Ca_{0.60–0.46}Na_{0.38–0.52}K_{0.02–0.03}$ $Al_{1.60–1.46}Si_{2.40–2.54}O_8$	$Na_{0.95–0.87}Ca_{0.05–0.13}K_{0–0.03}$ $Al_{1.05–1.13}Si_{2.95–2.87}O_8$	$K_{0.85–0.1}Na_{0.15–0.9}Ca_{0–0.1}$ $Al_{1–1.1}Si_{3–2.9}O_8$
Phenomenon	Labradorescence	Peristerescence	Adularescence
RI	1.56–1.57	1.54–1.55	1.52–1.53
Crystal system	Triclinic	Triclinic	Monoclinic/triclinic
Twinning	Polysynthetic Albite twins parallel to (010) always prominent; Pericline twins near (001) cutting through the iridescence also possible		Not observable without magnification except in anorthoclase; complicated patterns may be seen under the microscope
Orientation of iridescence	Best seen on the (010) cleavage, parallel to the Albite twin lamellae		Mostly on fractures or polished surface near (100), intersecting both cleavage planes
Color of iridescence	Any spectral color, from violet to red, always high saturation	Mostly blue, but yellow, pink, and violet also common	Silver, white, light blue, and occasionally light yellow
Zoning of iridescence	Multiple iridescent colors separated by sharp boundaries almost always present in large specimens (figure 28, A–D)	Uncommon; if present, the transition is always smooth and blurry between different zones (figures 29A and 30, B and C)	
Bodycolor and transparency	Mostly dark colored due to opaque inclusions, although materials from certain locations can be transparent and clear (figure 28)	Almost always light colored; transparency may vary depending on inclusions and alteration; mostly transparent to semitransparent	Color varies widely depending on chemistry and inclusions, but light colors are most common; always milky in appearance and translucent to semitranslucent
Other possible phenomena	Silver chatoyancy or asterism due to opaque needle inclusions are common in dark-colored labradorite cabochons (figure 23B); aventurescence also observed in some specimens (figure 22D)	Low-quality aventurescence possible but uncommon (figure 29C)	Chatoyancy or asterism (rare) may appear in cabochon-cut stones (figure 30, E and F); aventurescence, if present, usually overwhelms adularescence, and the material would be classified as sunstone before moonstone (e.g., figures 22F and 30D)

"rainbow moonstone." If moonstone is named after its resemblance to moonlight, how can something with rainbow colors be called moonstone?

It is certainly unrealistic to hope that the gem trade will always adopt scientifically accurate mineralogical terms and abandon ambiguous trade names such as "rainbow moonstone." Nonetheless, for gemological researchers and collectors who care about proper usage, the iridescent feldspar terminology certainly needs to be clarified. Although it would not be possible to replace the term *adularescence* due to its long history and wide adoption in gemology, ideally the term should be restricted for the moonlight-like white or silver glow as originally intended. However, since the name *moonstone* now includes any iridescent cryptoperthite (Smith and Brown, 1988, p. 20), it is perhaps inevitable that adularescence would cover the less common blue or yellow iridescence as well. Still, it should be strictly limited to "true moonstones" that are alkali feldspars with intergrown albite and orthoclase. Note that the general term *iridescence*,[5] probably for lack of a better word, has been used in the mineralogical literature to describe all optical effects that involve the interference of light, including white and silver adularescence (e.g., Parsons, 2010). The term *iridescent color*, however, should certainly be reserved for spectral interference colors with high saturation (figure B-1). The key distinctions between different iridescent feldspars are twinning, zoning, and iridescence orientation. Bodycolors, inclusions, and iridescent color are certainly useful but not always diagnostic as many would assume. The physical and color properties of various iridescent feldspars are summarized in table 1.

[5]The terms *adularescence*, *labradorescence*, and *peristerescence* are not descriptive terms based on appearance but are directly tied to the gem species moonstone, labradorite, and peristerite, respectively. This means that they are only useful when the gemstone has already been positively identified. Therefore, only the general term *iridescence* should be used when describing an unidentified feldspar gem.

To observe the iridescence of a moonstone, or any other iridescent feldspar, a face near-parallel to the lamellae orientation must be well-polished. On a flat surface, the iridescence can be seen only at certain angles relative to the illumination, which is why it is a schiller effect. As on asteriated or chatoyant stones, a curved surface focuses the reflected light into a smaller area above the stone, allowing the iridescence to be seen over a wider angle. This is why iridescent feldspars are often cut into cabochons or "pebbles." Moreover, the lamellae in moonstones are not simple two-dimensional structures. The thin films in potassic moonstones are elongated belts along the [106] axis (Jin et al., 2022b). The zigzag lamellae in intermediate or sodic moonstones have parallel ridges, which can evolve further into isolated needle-shaped albite domains parallel to the [106] axis. These linear features in the exsolution textures can create chatoyancy in a cabochon-cut moonstone (figure 30E). It is still unclear what textures cause the rare star effect in moonstones without hematite inclusions (figure 30F), but it might be related to the tweed or crosshatched twinning texture often found in low-temperature orthoclase. The "pull-aparts" along the (001) cleavage planes in the thicker albite spindles (dark near-vertical lines in figure 27D) resulting from the lattice dimension discrepancy between albite and orthoclase (Fitz Gerald et al., 2006) could also be responsible for the extra asterism rays in addition to the common cat's-eye associated with the linear textures along the [106] axis.

It is worth noting that synthetic colorless spinels showing chatoyancy or asterism, likely due to exsolution lamellae of corundum, have been reported as imitations of moonstone (Breebaart, 1958; Renfro, 2011a; Hodgkinson, 2017).

OTHER IRIDESCENT MINERALS WITH THIN-FILM OR MULTILAYER STRUCTURES

Exsolution textures are common in mineral solid solutions beyond feldspars, which means that iridescent colors due to multilayer interference can be found in other minerals as well. However, with crystal sizes much smaller than feldspars, these other iridescent stones do not draw nearly as much attention as iridescent feldspars. Two notable examples are Nuummite and iridescent garnet.

Nuummite, meaning "derived from Nuuk" in Greenlandic, is the trade name for iridescent amphibolite, first found near Nuuk, Greenland (Appel and Jensen, 1987; Rodgers et al., 1996). Similar material has also been discovered in the Sahara Desert of central Mauritania (Renfro, 2011b) and in the U.S. state of Wyoming (Dietrich et al., 1988). Studies of exsolution textures in orthoamphiboles are very limited compared to those of feldspars. It is confirmed that the iridescence in Nuummite is caused by periodic exsolution lamellae parallel to (010), alternating between anthophyllite (Ath: $Mg_7Si_8O_{22}(OH)_2$) and gedrite (Ged: $Mg_5Al_4Si_6O_{22}(OH)_2$) (Christie and Olsen, 1974; Champness and Lorimer, 1976; Gittos et al., 1976; Champness and Rodgers, 2000). With iridescent colors from golden yellow to violet-blue, over a dark gray matrix, Nuummite appears very similar to labradorite, except with smaller crystal sizes and elongated blade shapes (figure 31A). Also similar to iridescent feldspars, some Nuummite show zoning in the iridescence (Renfro, 2011b), likely due to slight variations in the chemical composition within the amphibole crystal.

Pink to blue iridescence are also sometimes observed in andradite garnet, known as "iridescent garnet" or "rainbow andradite" (figure 31B). They were first discovered in the Adelaide mining district in the state of Nevada (Ingerson and Barksdale, 1943), and later also found in Sonora, Mexico; Nara, Japan; and Inner Mongolia, China (Badar and Akizuki, 1997; Hainschwang and Notari, 2006; Badar et al., 2010; Nakamura et al., 2017; Yang et al., 2023). Electron microscope images show lamellar textures in these iridescent stones parallel to the {110} crystal face, with alternating layers rich in iron and aluminum (Nakamura et al., 2017). It is not clear whether these lamellae were created by exsolution or crystal growth. Structure refinement shows that the iridescent garnet has a non-cubic symmetry, resulting in anomalous birefringence in the typically isotropic mineral (Nakamura et al., 2017). A recent study discovered an orthorhombic garnet phase in the middle of the andradite-grossular ($Ca_3Fe_2Si_3O_{12}$–$Ca_3Al_2Si_3O_{12}$) solid-solution series with almost complete Fe-Al ordering in the structure, separated by miscibility gaps with the end members (Xu et al., 2023), which might be related to the formation of iridescent garnet. Further studies, particularly of the chemical compositions of the individual lamellae, are necessary to fully understand these rare and mysterious gemstones.

Many ore minerals, such as "peacock ore" (bornite, Bn: Cu_5FeS_4) (Buckley and Woods, 1983; Vaughan et al., 1987), show an iridescent tarnish on the surface due to a submicron oxidation layer that

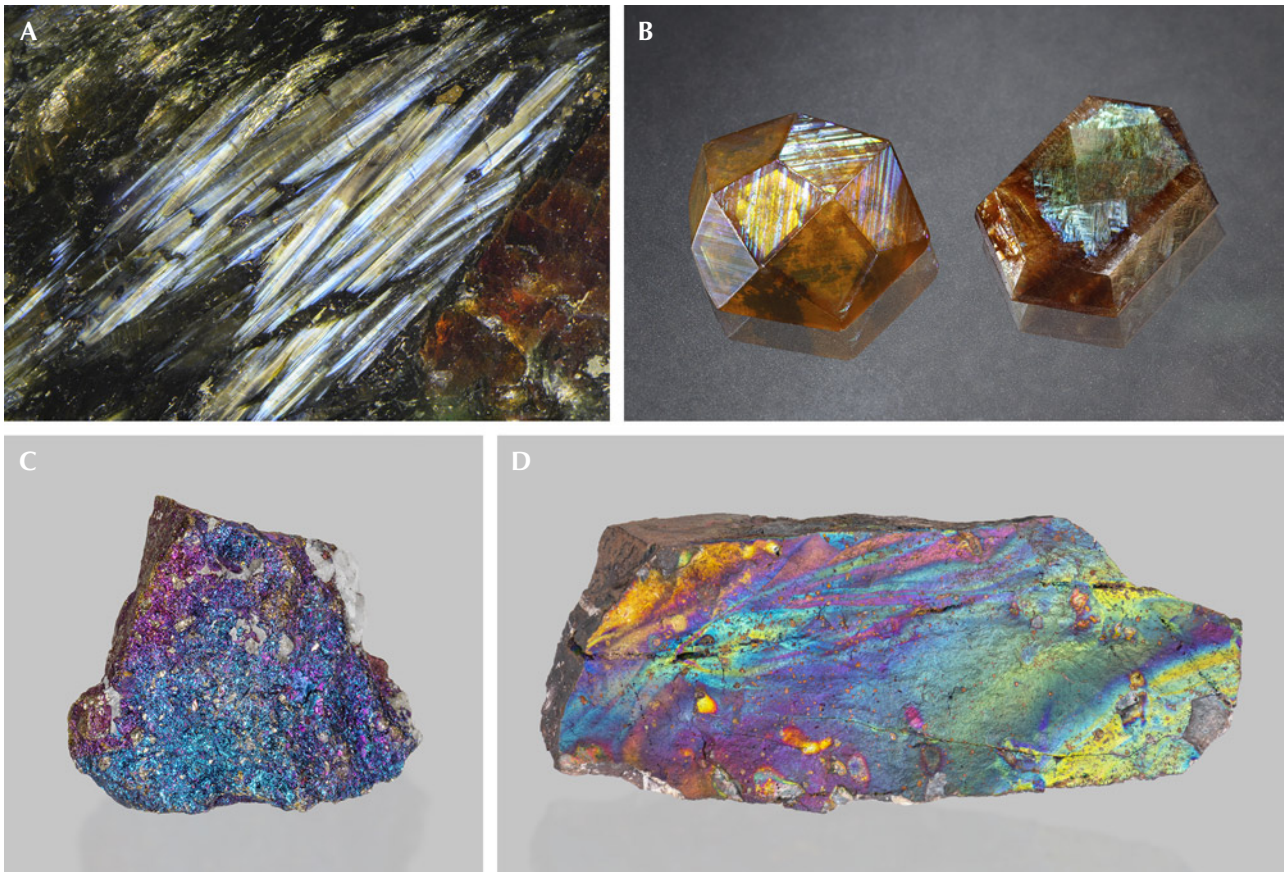

Figure 31. A: Elongated orthoamphibole crystals in Nuummite showing blue and yellow iridescence; field of view 10.29 mm. B: Two polished iridescent andradite crystals from Sonora, Mexico (left, 12 ct; courtesy of GIA's Dr. Edward J. Gübelin collection, no. 33283), and Nara, Japan (right, 11.39 ct; courtesy of Keiko Suehiro, GIA Museum no. 36136). C: Acid-treated chalcopyrite (7 cm wide) showing purple and blue iridescent tarnish on the surface; courtesy of Rachelle Turnier. D: Iridescent geothite (turgite) from Bukit Besi, Malaysia (12 cm long); courtesy of Rachelle Turnier. Photos by Nathan Renfro (A), Annie Haynes (B), and Emily Lane (C and D).

can cause thin-film interference. Most of these minerals are sulfides and native metals, which form in reducing conditions and can be easily oxidized when exposed to an oxidizing atmosphere. This process can be accelerated by acid treatment, which is used to artificially create the iridescent tarnish (e.g., figure 31C). Iridescent goethite, or turgite, which can already be an alteration or weathering product of other iron ore minerals, is a notable exception among iron ores (figure 31D). Electron microscopy analyses reveal quasiperiodic layers of voids near the surface that can cause thin-film or multilayer interference responsible for the striking iridescent colors. It is not clear how these void layers form, but episodic surface poisoning due to cyclical weather conditions is a likely mechanism (Heaney et al., 2018).

IRIDESCENT QUARTZ

Natural iridescent quartz, also known as iris quartz, rainbow quartz, schiller quartz, anandalite, and adularescent quartz, has been recognized since its discovery in the Deccan Traps of India in the nineteenth century (Petrov and Tanaka, 2011). Iridescent quartz has also been reported from the United States (Washington), Uruguay, Brazil, Germany, Turkey, and Morocco (Gübelin and Koivula, 2005; Petrov and Tanaka, 2011; Renfro and Koivula, 2011). Although it was discovered more than a hundred years ago, iridescent quartz mostly escaped scientific investigation, with the exception of a brief study by Raman (1950b). The structure in natural quartz causing the iridescent colors, ranging from red to blue, was not revealed until recently (Lin and Heaney, 2017). The iridescence in quartz is visible only on the minor z {011} faces of

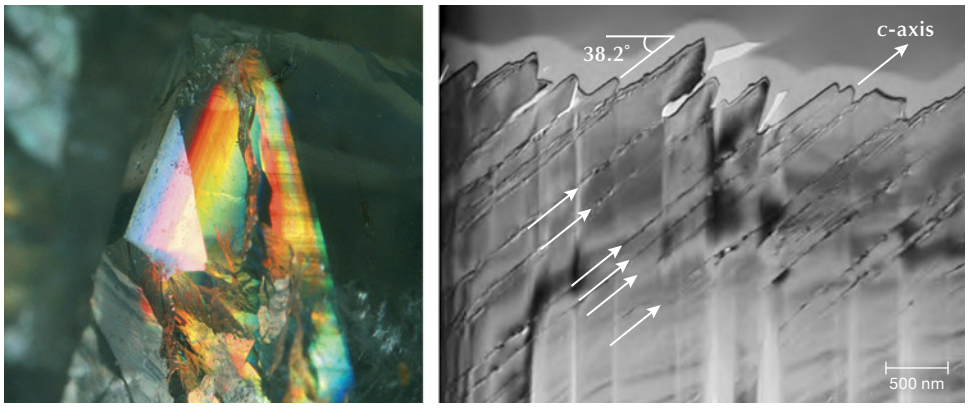

Figure 32. Left: An iridescent quartz crystal from India. Photomicrograph by Nathan Renfro; field of view 6.3 mm. Right: A TEM image showing periodic grooves on the z face of an iridescent quartz; image from Lin and Heaney (2017).

euhedral quartz crystals, not on any other crystal faces or broken surfaces (figure 32, left). Upon polishing, the iridescence briefly intensifies before completely disappearing, indicating it comes from a very thin layer near the surface of the crystal. Electron microscope and AFM images reveal periodic groove structures on the iridescent face correlated with polysynthetic Brazil twin lamellae, which can diffract visible light like a diffraction grating (box F) and create iridescence (figure 32, right). The grooves are theorized to form by preferential surface etching along the twin boundaries by invasive fluids.

PRECIOUS OPAL

Opal has been studied extensively due to its broad occurrence and long history as a gemstone, as well as the more recent interest in photonic material design with an opal-like periodic structure (Baryshev et al., 2006; Arnon et al., 2018). However, like with moonstone, most scientific investigations of opal focus on its submicron textures and atomic structures, with few quantifying its optical properties. In gemology, "precious opal" is separated from "common opal" by its play-of-color[6] (figure 33). Only microscopically ordered opal-AG and opal-CT may show the play-of-color effect (Curtis et al., 2019), and SEM investigations into the iridescence have revealed stacked silica nanospheres (opal-AG) or "lepispheres" (spheres of blades in opal-CT) of the same size (~250 nm), providing the first evidence of 3D photonic crystals (figure 34) (Sanders, 1964; Darragh and Sanders, 1965). Common opal-AG is also composed of nano-size silica spheres, but the latter are not regularly stacked due to their nonspherical shapes and broad size distributions (again, see figure 2). Common opal-CT shows even more variability with respect to nanostructures, ranging from nano-size silica platelets to nanofibers (Gaillou et al., 2008). Some non-iridescent opals also have regular periodic structures, but the diameters of the silica spheres are too large or too small to diffract visible light. Precious opal can be synthesized through the Stöber process (Stöber et al., 1968), which involves organic solvents that are not present in geological environments where natural opals form. Some XRD analyses show that synthetic opal can be more crystalline than opal-CT, even though they comprise silica nanospheres similar to natural opal-AG, instead of the lepispheres as in natural opal-CT (Hernández-Ortiz et al., 2015). The fragility of synthetic opals is similar to that of natural ones, which is partly why opal simulants made partially or purely of plastic are more common in the market (Renfro and Shigley, 2018; Renfro, 2019).

Sanders (1968) performed a light diffraction experiment on a precious opal using a similar configuration as X-ray crystallography, thereby directly correlating the optical effect and the internal structure of opal for the first time. Quantitative models have also been developed for synthetic opals,[7] showing an angle dependence for the diffracted color that matches the experimental observations (Baryshev et al., 2003a,b, 2006). Besides the sharp diffraction spots expected for a perfect 3D periodic structure, local planar or linear stacking defects of the nanospheres in opal can also give rise to continuous scattering features, which is why asterism and chatoyancy can be observed in some opals (Sanders, 1976; Soonthorntantikul, 2014) (figure 33, E and F).

[6]Using the term *opalescence* to describe opal's play-of-color should be discouraged because not all opal displays play-of-color. The milky appearance, however, is a common feature of all opals, which should be what the term is used to describe.

[7]Because opal does not have a well-defined chemistry or crystal structure, it is difficult to define a distinct boundary between synthetic opal and opal simulants (e.g., Schmetzer and Henn, 1987). Therefore, the term *synthetic opal* may not always be used precisely in non-gemological literature.

Box F: Diffraction of Light by Periodic Structures

Light scattered by a periodic structure can interfere and cause diffraction of certain wavelengths along specific directions. The simplest example of this phenomenon is from a diffraction grating, which is a planar optical element with a periodic structure (figure F-1). Diffraction gratings can be further categorized into transmission gratings, with periodic slits that allow light to pass through, and reflective gratings, which have periodic grooves that reflect light. Note that the individual slits or grooves in a diffraction grating may scatter light in multiple directions like the needle inclusions described in box B, although certain directions may be preferred over others depending on the shape of the cross section.

The principle for constructive interference, or the "diffraction" condition, is the same as for thin-film interference, such that the optical path difference between light scattered by different slits (period of d) or grooves is an integral multiple (m) of the wavelength (λ):

$$2d(\cos\theta_i - \cos\theta_s) = m\lambda \qquad \text{(F-1)}$$

where θ_i and θ_s are the incident angle and the scattering angle relative to the grating plane, respectively. This equation is also known as the Laue equation in X-ray crystallography. It should be noted that the scattering angle in the equation applies to both backscattering (reflection grating) and forward scattering (transmission grating). In fact, a diffraction grating can function as both a transmission grating and a reflective grating if the surfaces between the slits are reflective.

Note that the equation has two independent angles, which is much less restrictive than the thin-film or multilayer interference that follows the law of reflection and refraction. This means that the diffraction colors from periodic structures can be seen in many different directions, instead of only at one specific orientation. Moreover, the cosine function is more sensitive to changes at the typical viewing angles closer to 90°. As a result, the iridescent color from diffraction dramatically changes with small changes of incident angle, sample orientation, or viewing direction (figure F-2), creating the phenomenon known as play-of-color. In fact, with a large enough diffraction grating, the entire visible spectrum can be seen without any movement, as light diffracted from various parts of the diffraction grating enters the eye at different angles and is seen as different colors (figure F-2).

The periodic diffraction structure can be expanded into two or three dimensions, which creates more complicated diffraction patterns. The basic principle remains the same as in equation F-1, except it would need to be applied to all periodic arrays found in the higher-dimensional structure. The volumetric equivalent of the planar diffraction grating is called a "photonic crystal" because it diffracts visible light similar to the way in which a crystalline solid diffracts X-rays. Depending on the num-

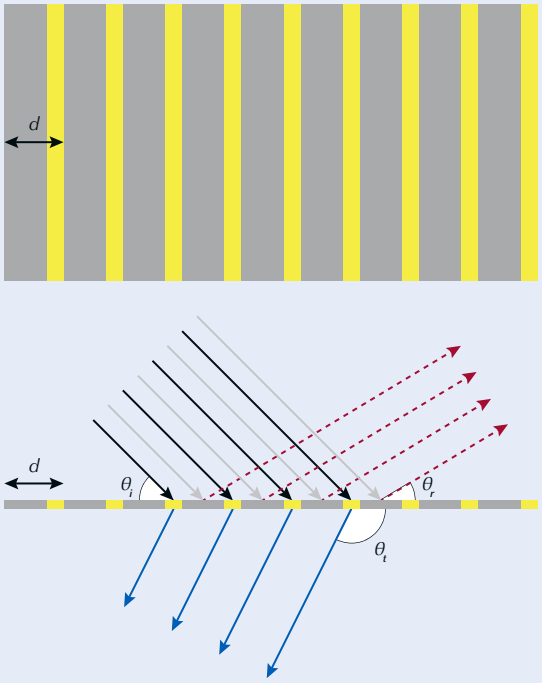

Figure F-1. Schematic drawing of a diffraction grating (top) and its cross section (bottom). Light can be reflected by the periodic grooves or transmitted through the periodic slits in the grating. The light waves scattered by different grooves or slits can constructively interfere with each other depending on the incident and scattering angles.

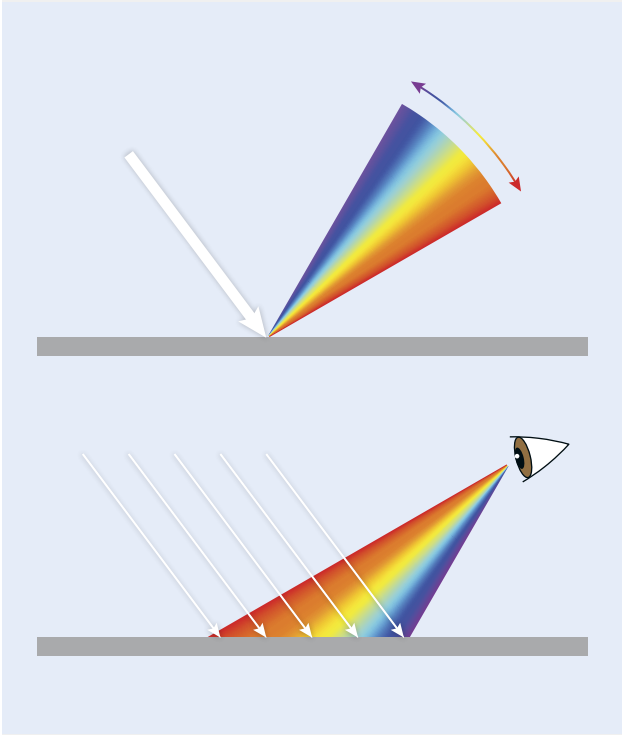

Figure F-2. The interference color created by a diffraction grating is very sensitive to the scattering angle. Dramatic color change can be observed with a small tilt (top), and the entire color spectrum may be seen over a wider area (bottom). This is why iridescence created by diffraction is often called play-of-color.

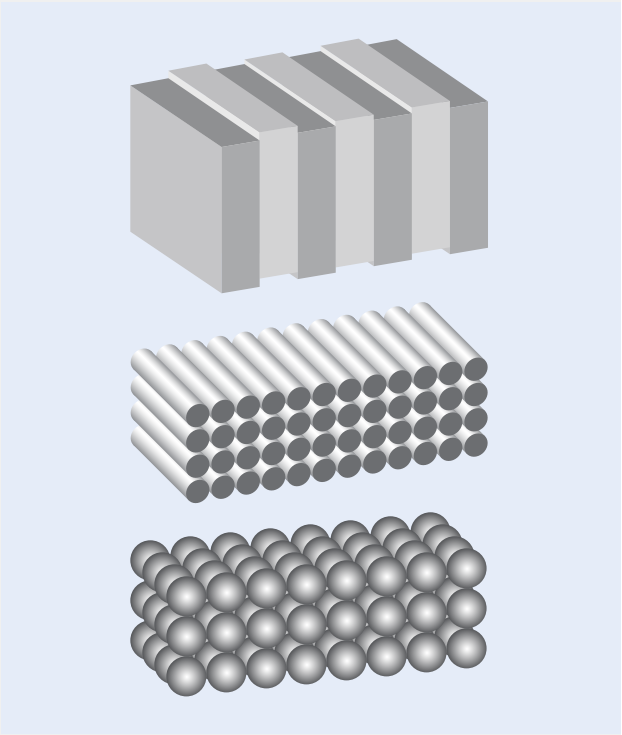

Figure F-3. Schematic drawing of 1D (top), 2D (middle), and 3D (bottom) photonic crystals, as defined by the number of dimensions in which they are periodic. The periodic units in photonic crystals are typically at a scale of ~100–200 nm.

ber of periodic directions, they can be further divided into 1D, 2D, and 3D photonic crystals (figure F-3). The layered structures of iridescent feldspars and garnets discussed above are examples of 1D photonic crystals, which is why the multilayer interference condition is sometimes described as Bragg's law following the terminology of crystallography. By a similar analogy, the disordered structures that scatter light randomly, as in common opal, milky sapphire, and fancy white diamond, can be considered photonic glasses. Compared to the particles, needles, and films discussed in previous sections, the periodic structures of diffraction gratings and photonic crystals are much more intricate and require more complicated processes to form, so they are typically less common in minerals. The formation mechanisms of the gemstones discussed in this section are also generally not well understood.

Colors created by the scattering, interference, or diffraction of light are often known as structural colors (or less commonly "physical" colors), as they are produced by the physical structures in the material. Unlike pigmented (chemical) colors created by the selective absorption of wavelengths within the visible light spectrum due to electron transfer or excitation, which thus are determined only by chemistry, structural colors are often considered "not real" and referred to as "pseudochromatic" colors in older literature references (e.g., Ostwald, 1965; Nassau, 1978), partly because they may change dramatically with the viewing angle. However, the difference between structural color and pigmented color may not be as distinct as most would assume. For instance, the colors of metal colloids, such as the red and green colors of Oregon sunstones, are certainly structural as they depend strongly on the sizes and shapes of the metallic nanoparticles, although their appearances are often indistinguishable from chemical pigments. Compared to pigmented colors, structural colors are typically brighter, easier to tune, more durable, and more economical and environmentally friendly, which might be why they are so prominent in the biological world, most commonly found in butterfly wings and bird feathers (Kinoshita, 2008).

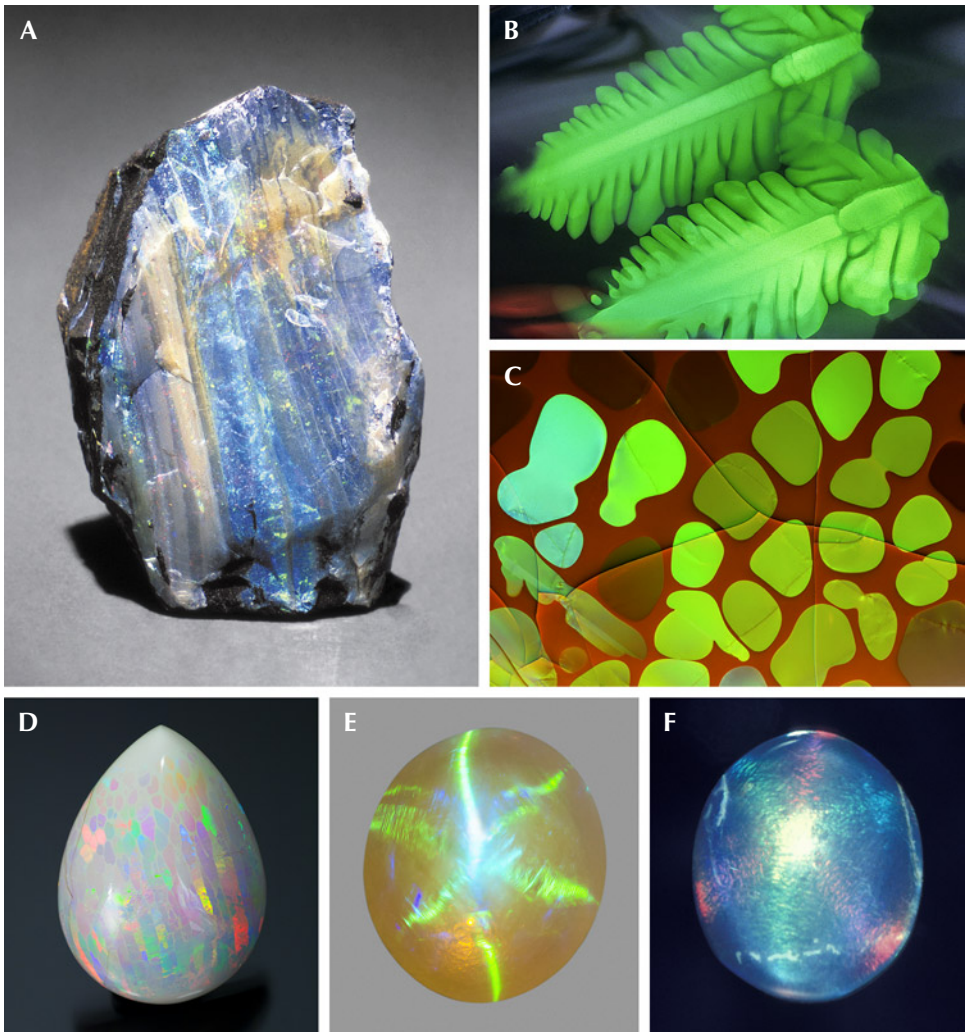

Figure 33. A: A rough opal showing play-of-color in a layered structure. B: Opal from the U.S. state of Nevada, showing two fern-shaped holographic play-of-color patterns. C: Play-of-color in a cell structure; courtesy of John I. Koivula. D: Ethiopian opal showing play-of-color in a digit pattern; courtesy of Opalinda and EyaOpal. E: A 2.39 ct opal showing a six-rayed star with play-of-color. F: Another star opal with different play-of-color on the opposing rays. Photos by GIA staff (A, E, and F), John I. Koivula (B), Nathan Renfro (C), and Robert Weldon (D); fields of view 13.5 mm (B) and 11.28 mm (C).

IRIS AGATE AND FIRE AGATE

Agate is a banded variety of chalcedony, which is a fibrous cryptocrystalline variety of silica mostly composed of polysynthetic Brazil-twinned α-quartz intergrown with mogánite (Mog: SiO_2), a silica polymorph. Agates form mostly in the cavities of acidic or basic volcanic rocks, although they are also occasionally found in hydrothermal veins or sedimentary rocks. The characteristic banding of even unpigmented agates with respect to darkness and clarity reflects variations in the relative proportions of quartz and mogánite and their crystal sizes and habits, as well as the presence of porosity and microinclusions (Götze et al., 2020). The chalcedony fibers in agate are mostly "length-fast," meaning they are elongated perpendicular to the *c*-axis of quartz,

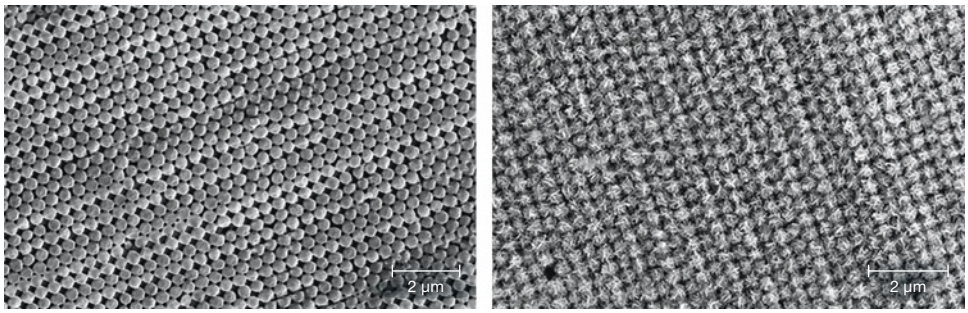

Figure 34. Left: SEM image of a precious opal-AG from California. Right: SEM image of a precious opal-CT from Mexico showing lepispheric structures. Images from Gaillou (2015).

instead of parallel to that axis like prismatic quartz crystals. Pervasive screw dislocations torque the optical axis of the silica crystallites in agate to twist around the fiber axis (Heaney, 1993), creating a unique banded pattern in cross-polarized light known as *Runzelbänderung* (figure 35A; Bernauer, 1927). The more vibrant colors of agate arise mainly from pigmentation by iron (hydr)oxides or manganese oxide compounds. The formation mechanism of agate is still mostly enigmatic, and no attempts at synthesis have been successful in reproducing the nanoscale textures of agate (Götze et al., 2020; Moxon and Palyanova, 2020; Heaney, 2021).

Some agate, when cut into doubly polished thin slabs, show iridescence under transmitted light and therefore are called "iris agate" (figure 35, B–D). The iridescence of most iris agate is diffuse, with low color saturation, although brilliant play-of-color can occasionally be observed in specimens of the best quality. The special optical property of iris agate was first described by Brewster (1813 and 1843) who observed a periodic texture parallel to the agate banding that functions as a transmission grating, which was first captured photographically by Jones (1952). Raman and Jayaraman (Jayaraman, 1953; Raman and Jayaraman, 1953b, 1955) correctly pre-

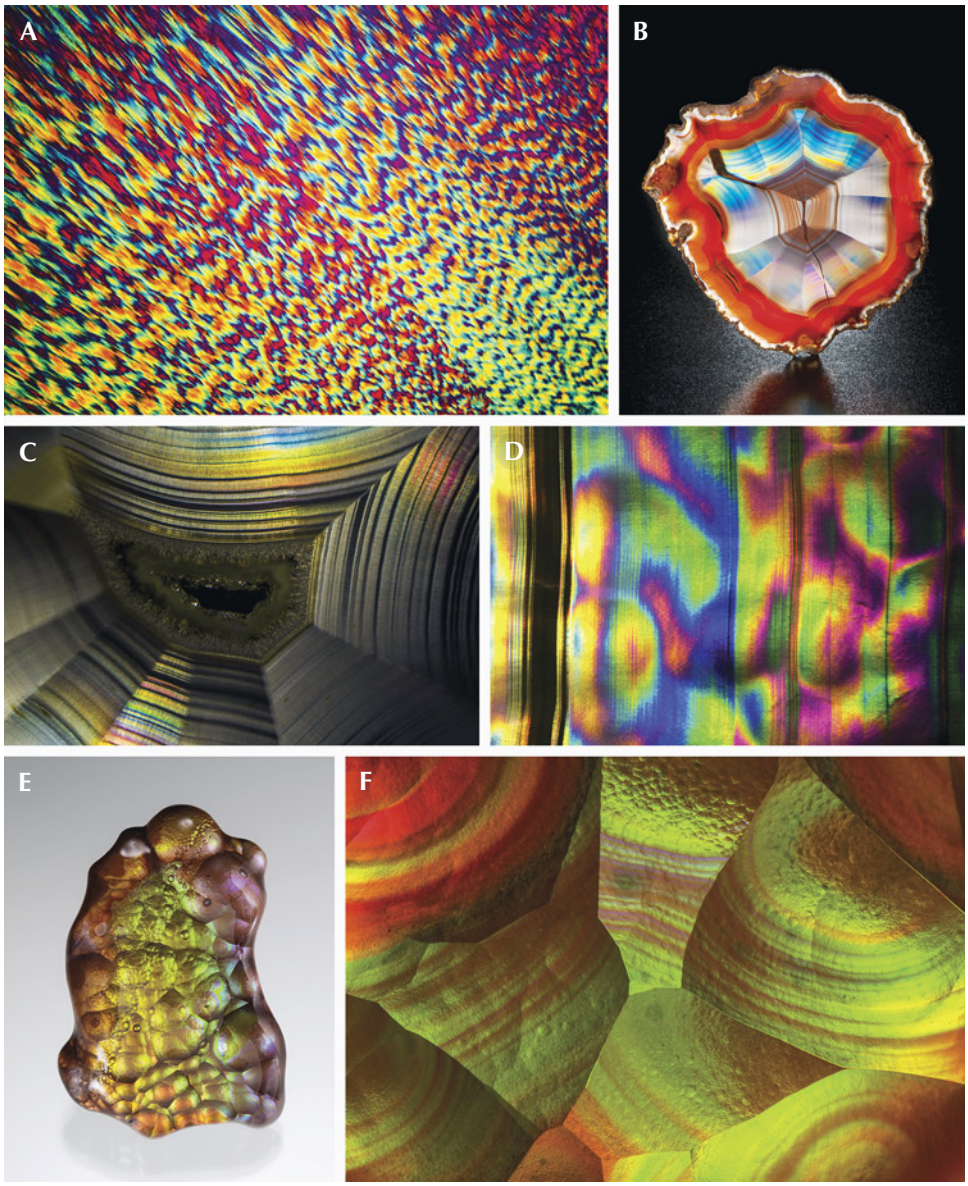

Figure 35. A: A thin section of iris agate under cross-polarized light (lambda plate inserted) showing a Runzelbänderung *pattern. B: An iris agate slice from Mexico; courtesy of Si and Ann Frazier. C: Iris agate banding. D: Iris agate banding with patchy play-of-color. E: A 48.04 ct botryoidal fire agate from the U.S. state of Arizona; courtesy of Larry Woods, GIA Museum no. 37742. F: Iridescent surface of a botryoidal fire agate showing concentric patterns. Photos by Nathan Renfro (A, C, D, and F) and Robert Weldon (B and E); fields of view 32 mm (C), 15.67 mm (D), and 6.87 mm (F).*

dicted the optical orientation of the quartz crystallites based on the polarization of the transmitted light. Electron and optical microscopy studies have revealed hierarchical fractal textures in agate, which show intricate intergrowth relations among mogánite, Brazil-twinned quartz, and untwinned quartz at scales ranging from nanometers to centimeters (Heaney, 2021). Unfortunately, no study has been published that couples TEM analyses with laser light diffraction experiments to clarify the relation between the iridescence quality and the periodicity of the intergrowth texture.

Fire agate is another variety of iridescent chalcedony that typically has a botryoidal form. It displays primarily green to orange iridescence over a predominantly brown bodycolor (figure 35, E and F). The iridescence, or "fire," of fire agate is observed on the unpolished natural surface under reflected light, and it does not change dramatically at different angles. Studies on fire agates are terribly limited, and thus, without any careful high-resolution electron microscopy investigation, the cause of the iridescence is still undetermined. Thin-film interference from layers of iron (hydr)oxide, which is also responsible for the dark brown bodycolor, is the most probable cause of the iridescence in fire agate (McMackin, 1974; Schumann, 2009; Newman, 2014).

It should be noted that fire agate is often not considered real agate because identification is based on its iridescence rather than the characteristic banding. Nonetheless, a recent study revealed typical agate banding in the cross section of a fire agate from the U.S. state of Arizona (Natkaniec-Nowak et al., 2020), although it is not clear if the banding is necessary to create the fire effect, or if they are even related at all. More careful microscopic studies over a broader selection of samples are needed to confirm (or disprove) the relation between the fire effect and the agate banding.

"RAINBOW" HEMATITE

Metamorphic hematite schist in a banded-iron formation from the Andrade iron ore deposit in Minas Gerais, Brazil, shows sparkling iridescent colors ranging from purple, blue, and green to yellow and orange (figure 36A). SEM and AFM images show orderly stacked spindle-shaped hematite nanorods arranged in a triangular pattern (figure 36, B and C). The hematite nanocrystals are ~200–300 nm long and

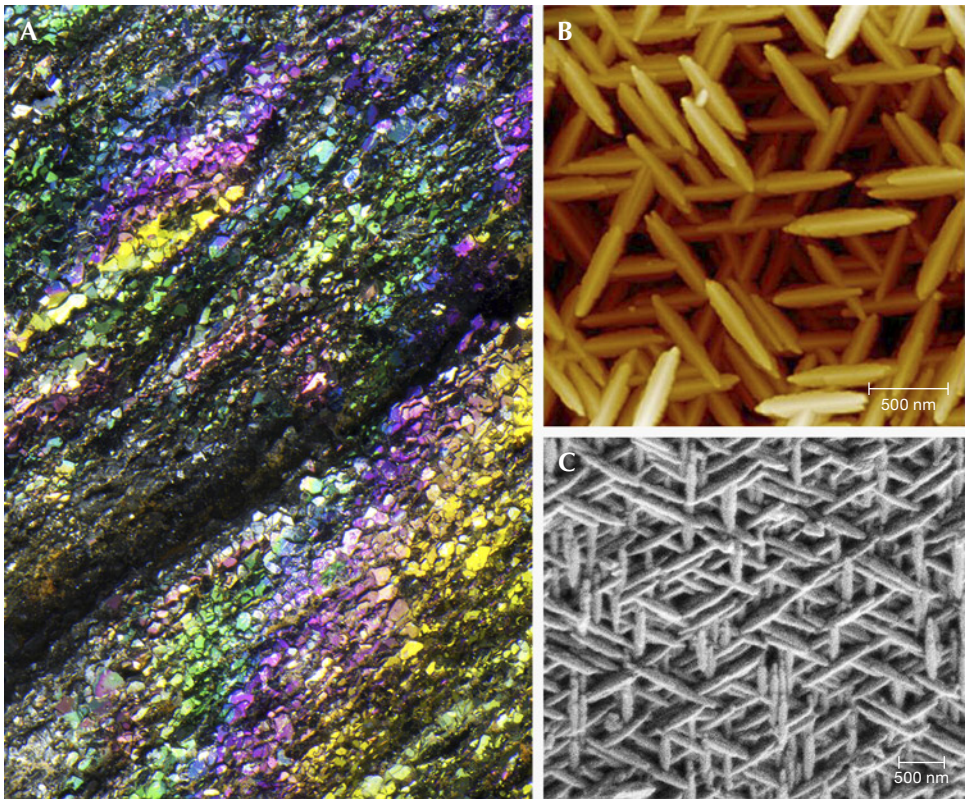

Figure 36. A: "Rainbow" hematite specimen showing different iridescent colors; courtesy of Rhonda Wilson. Photomicrograph by Nathan Renfro; field of view 4.07 mm. B and C: AFM and SEM images of the surface of "rainbow" hematite; images from Lin et al. (2018).

~50–60 nm wide, with the spacing in between on the scale of 280–400 nm, which makes "rainbow" hematite a 3D photonic crystal like precious opal (Lin et al., 2018). Nonetheless, the iridescence appears to be a surface effect in light of hematite's high absorptivity and reflectivity. Hematite's high RI further constrains the diffraction angle, resulting in iridescent colors that do not change noticeably with changing angles, instead of the play-of-color effect observed in precious opal.

EDS analyses and structural refinement from XRD reveal high concentrations of aluminum and trace phosphorus impurities in "rainbow" hematite, which may be the reason for the unusual shape of the nanocrystals. Phosphorus is known to preferentially attach to the prismatic {100} and {110} faces, which promotes spindle-shaped crystals over the typical rhombohedral form. The orderly stacked texture of "rainbow" hematite is theorized to have resulted from oriented aggregation, due to spontaneous alignment of the crystal lattices of independently crystallized hematite nanorods (Lin et al., 2018).

The nanorod structure was believed to be pervasive throughout the entire specimen because the iridescence can also be observed on freshly fractured surfaces (Lin et al., 2018). However, because strongly foliated hematite schist is composed of iridescent flakes at the scale of ~100 μm (figure 36A), the "freshly fractured" surface could be mostly separated boundaries between flakes, instead of revealing the interior of individual flakes. A recent study showed that some flakes contain non-iridescent patches, which are exposed areas of bulk hematite crystals (free of aluminum or phosphorus in the EDS spectrum) under a "coating" of stacked nanorods (Rossman and Ma, 2025). Somewhat similar nanorod structures associated with the enrichment of aluminum and phosphorus (or arsenic) have also been observed on the surface of several non-foliated hematite specimens from Mexico and the United States (Oregon and Alaska), although their nature could not be confirmed by XRD or EBSD due to the limited size (Rossman and Ma, 2025).

RAINBOW SCAPOLITE

Some included scapolite (Scp: $Ca_4Al_6Si_6O_{24}CO_3$–$Na_4Al_3Si_9O_{24}Cl$ solid solution) crystals, reportedly from India, Tanzania, and Mozambique (Choudhary, 2013; Ye et al., 2021), display striking iridescent colors under reflected light (figure 37), hence called rainbow scapolite. The iridescence derives from thin brown lamellar inclusions decorated by darker dots, which are identified as magnetite using Raman spectroscopy and XRD (Sun et al., 2015; Ye et al., 2021), presumably formed by solid-state precipitation.

Different from the iron oxide inclusions in rainbow lattice sunstone, the iridescence from the magnetite inclusions in scapolite changes color dramatically when observed at different angles (video 6), making it a play-of-color effect like that in precious opal. The transparent appearance of the typically opaque magnetite lamellae also indicates that the iridescence of rainbow scapolite is created

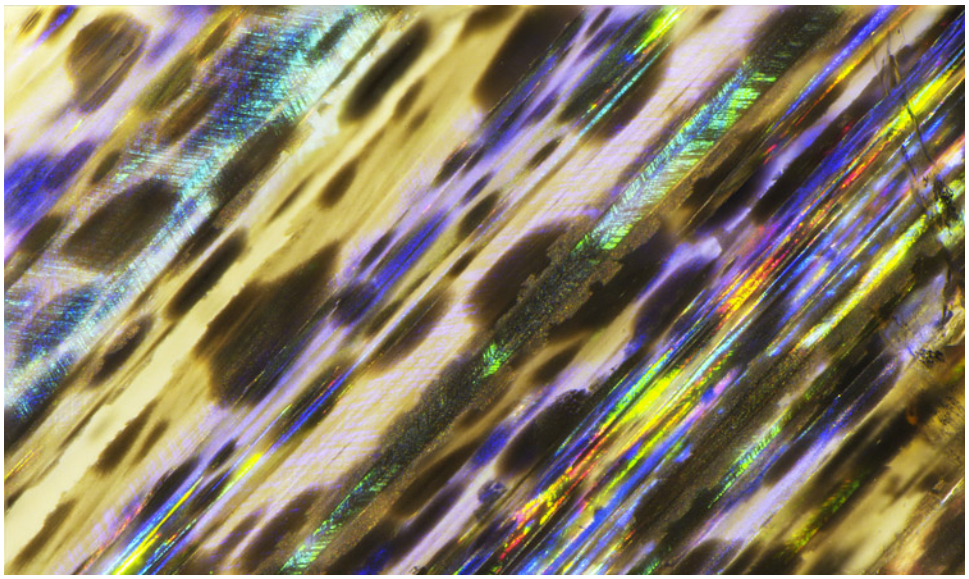

Figure 37. Magnetite inclusions in rainbow scapolite showing iridescence under reflected light. The iridescent color is observed only at certain angles due to diffraction. Photomicrograph by Nathan Renfro; field of view 4.8 mm.

by a diffraction grating instead of thin-film interference (Ye et al., 2021). Scapolite is a unique mineral that can contain the diffracting crystals inside rather than on the surface, so it can be faceted without affecting the play-of-color. Further electron microscopic investigation is needed to understand the mechanism that creates such an intricate structure inside an otherwise homogeneous crystal.

IRIDESCENCE OF SHELL AND PEARL

Structural colors are much more common in the biological world than in the mineral world because living creatures are better at creating minute and regular structures at the optical scale. Butterfly wings, bird feathers, beetle shells, fish scales, and even fern leaves can all display brilliant iridescent colors from submicron structures that have been perfected by natural selection over millions of years (Kinoshita, 2008). With shells and pearls, mineralogy and biology intersect through the process known as biomineralization.

Most pearls and the inner surfaces of shells of pearl-producing mollusks are constructed of nacre, or mother-of-pearl, a composite material consisting of closely packed single-crystal aragonite (Arg: $CaCO_3$) platelets bonded together by thin films of conchiolin (an insoluble protein), forming a "brick-and-mortar" structure (figure 38, left). The aragonite platelets range from ~300–600 nm in thickness (Snow et al., 2004), with the degree of variation depending on the species and growth conditions. Surprisingly, despite the seemingly straightforward lamellar texture reminiscent of that of iridescent labradorite, the origin of iridescence in nacre is not as simple as many would assume.

Most studies of iridescent nacre have been performed on shells instead of pearls (Raman, 1935; Ball, 1982; Liu et al., 1999, 2003; Brink et al., 2002; Tan et al., 2004; Snow and Pring, 2005), mainly because iridescence is more prominent in the former (Snow et al., 2004) (figure 39), although the lower prices and larger sizes of shells certainly also influence sample selection. The nacre of a pearl is believed to be identical to the shell it is extracted from, as they form through the same mineralization process. However, it should not be assumed that the cause of iridescence is also the same for pearls and shells, because surface textures could play an important role.

Much evidence suggests that the iridescence of nacre is caused by a diffraction grating on its surface. Early studies showed that some iridescent colors of nacre can be "communicated" or transferred to beeswax (Brewster, 1833; Pfund, 1917; Strutt, 1923b). More recent studies of shells have both documented the periodic grooves on the shell surface using SEM and measured the optical backscatter diffraction pattern with a laser (Liu et al., 1999, 2003; Tan et al., 2004). The periodic steps observed in these studies are created by the shell surface intersecting the stacked aragonite layers at a small angle (figure 38, right). Interestingly, as Raman (1935) first pointed out, the internal multilayer interference effect coincides with a section of the surficial diffraction spectrum along the same direction, because the diffraction grating on the surface arises from the layered structure inside the nacre. Several recent computational studies have simulated the appearance of

Figure 38. Left: SEM image of the cross section of a broken pearl showing packed aragonite platelets. Image from Snow et al. (2004). Right: SEM image of the surface of an iridescent shell showing periodic grooves that act as a reflection grating. Image from Liu et al. (1999).

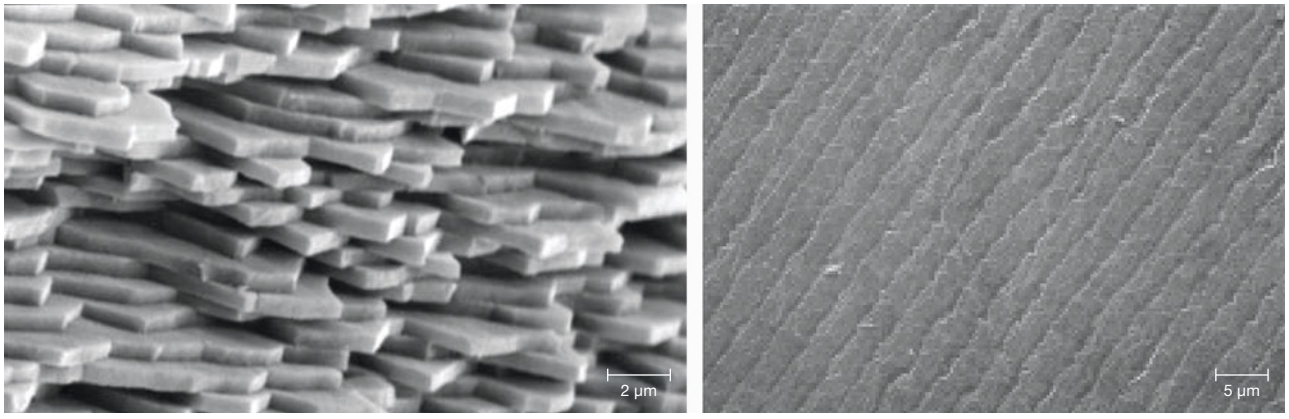

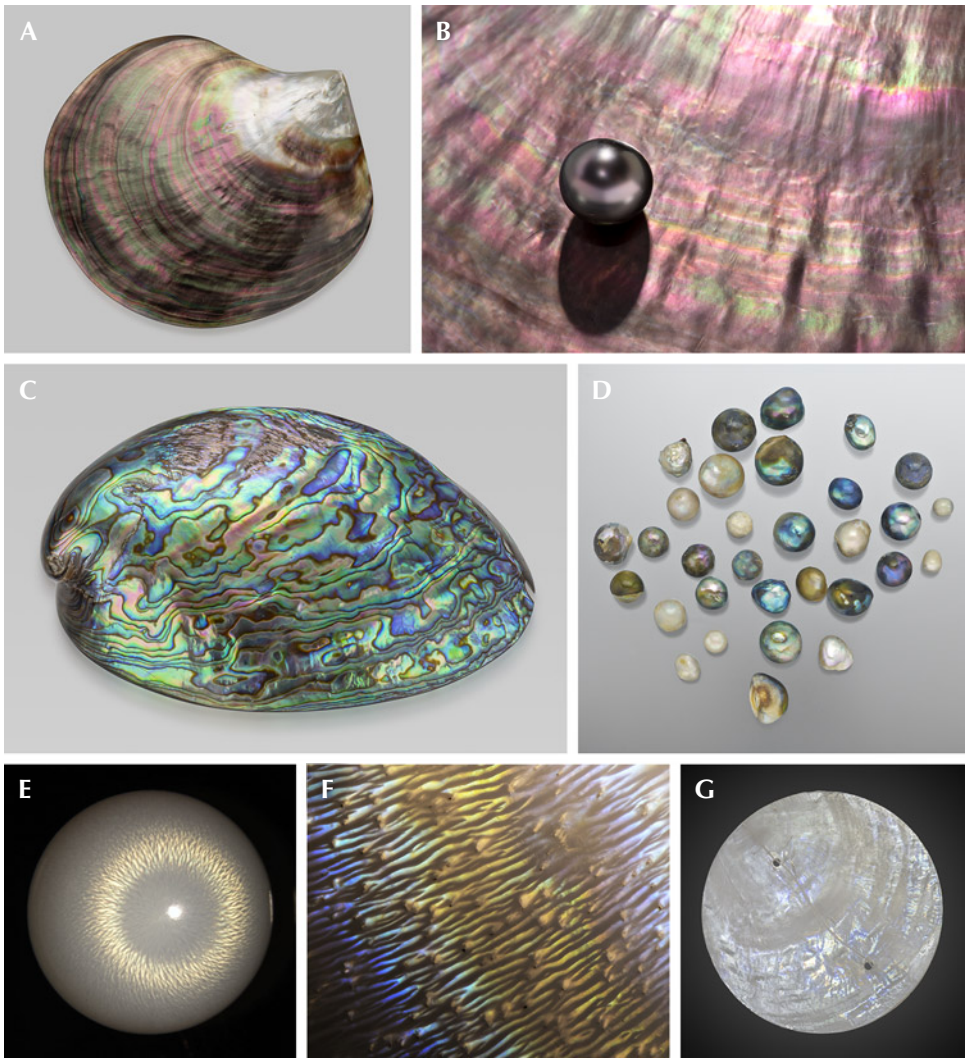

Figure 39. A: A polished Pinctada margaritifera *shell (110.9 g) from Tahiti showing strong iridescent colors; courtesy of GIA Museum, collection no. 23105. B: A Tahitian cultured pearl with pink iridescent overtone on top of an iridescent shell. C: An 87.90 g polished abalone shell; courtesy of GIA Museum, collection no. 36706. D: Semi-round abalone pearls, the largest measuring 10.93 mm and the smallest 4.46 mm; courtesy of KCB Natural Pearls. E: Iridescent flame structure on a 9.80 mm non-nacreous* Tridacna *pearl under fiber-optic illumination resembles a chatoyant effect. F: Flame structure of a* Spondylus *pearl showing yellow and blue iridescent colors; field of view 2.34 mm. G: Circularly cut windowpane oyster (*Placuna placenta*) shell (50 mm in diameter) showing faint iridescence. Photos by Emily Lane (A, C, and G), Robert Weldon (B), and Artitaya Homkrajae (E and F).*

pearls quite accurately using the multilayer interference model (Fan et al., 2021; Ozaki et al., 2021).

The most striking iridescent nacre is found in the shells of abalone (figure 39C), which as a sea snail (Gastropoda), belongs to a different class of shellfish than oysters, clams, and scallops (Bivalvia). Abalone is also known for producing irregularly shaped pearls with strong iridescence (figure 39D). The nacre produced by gastropods is columnar, comprising aragonite platelets that are thinner and more uniform than the sheet nacre found in bivalve shells (Snow and Pring, 2005), perhaps accounting for the stronger iridescence. The columnar nacre also contains isolated "stacks" on the surface (Guo, 2010), although it is not clear whether they contribute to the iridescent colors of abalone shells and pearls.

It is often assumed that the iridescence in shell and pearl is exclusive to the nacreous surface. However, recent studies have found a tilted lamellar structure under the non-nacreous outer surface of limpet shells, creating polarization-dependent green iridescent colors (Brink et al., 2002; Brink and van der Berg, 2005). Iridescence has also been observed in the flame structure of some non-nacreous pearls (figure 39, E and F), the underlying submicron structures of which have not yet been studied. A pearl consisting of calcite (Cal: $CaCO_3$) instead of aragonite with a "nacreous" appearance has also been discovered (Au, 2022). And a study on the windowpane oyster shell, which can display faint iridescence (figure 39G), revealed a calcite-dominant composition as well (Li and Ortiz, 2013).

IRIDESCENT AMMONITE

Ammonite is another shell-making mollusk closely related to squid and octopus, all of which belong to the class Cephalopoda. Ammonites are discussed separately in this section because they went extinct along with non-avian dinosaurs ~66 million years ago; therefore, they can be found only as fossils in sedimentary rocks. Ammonite fossils have been studied extensively by paleontologists, as they are considered important index fossils for the Devonian through the Cretaceous periods due to their broad geographic distribution and rapid evolutionary trends.

Some ammonite fossils from Madagascar, Canada, and Russia display iridescence with various colors, making them desirable not only to rock and fossil collectors but also in the gem market (figure 40). The best-quality material with the brightest iridescence is found in the marine shales of the Bearpaw Formation in southern Alberta, Canada, which was trademarked by the mining company Korite as "Ammolite," a term that is now in the public domain and can be applied to any iridescent ammonite (Mychaluk et al., 2001; Mychaluk, 2009). The iridescent ammonite recently discovered in Krasnoyarsk Krai, Russia, appears to be of comparable quality to Canadian ammolite, but in much smaller quantities (Radko et al., 2021). Most iridescent ammonites are in fractured pieces, which are extremely fragile and require special stabilization and manufacturing processes (e.g., stabilization with epoxy or made into doublets or triplets backed and covered by tougher materials) before they can be used for jewelry (Mychaluk et al., 2001; Shen and Liao, 2017).

The iridescence of ammolite is among the brightest of all iridescence in gem materials, yet studies of its optical properties and internal structures are very limited, partly due to its relatively recent discovery (Mychaluk et al., 2001). Iridescent ammonite is comprised of mostly aragonite, with small amounts of apatite, pyrite, siderite, and calcite (Shen and Liao, 2017; Radko et al., 2021). The few SEM images of iridescent ammonite reveal layers of aragonite platelets similar to the nacre in modern shells and pearls (Mychaluk et al., 2001; Shen and Liao, 2017; Radko et al., 2021). It is not clear how the fossilization process has altered the internal structures of the shells and affected the iridescent colors. The breakdown and replacement of the organic films in the original nacre would change the reflective properties of ammonite and may enhance the iridescent color.

SUMMARY

The range of different optical phenomena in the gem world is quite astonishing. The diversity of different optical phenomena in gemstones reflects the extreme ranges of thermodynamic conditions exhibited by geological processes. Most of the light-diffracting structures in phenomenal gemstones are secondary and form long after the original crystal-

Figure 40. Left: Iridescent ammonite fossil in its shale host rock (45 cm wide) from Alberta, Canada; gift of Korite International, GIA Museum no. 30195. Right: An ammonite fossil from Alberta, Canada, showing a full spectrum of color; courtesy of John I. Koivula. Photos by Kevin Schumacher (left) and Nathan Renfro; field of view 13.09 mm (right).

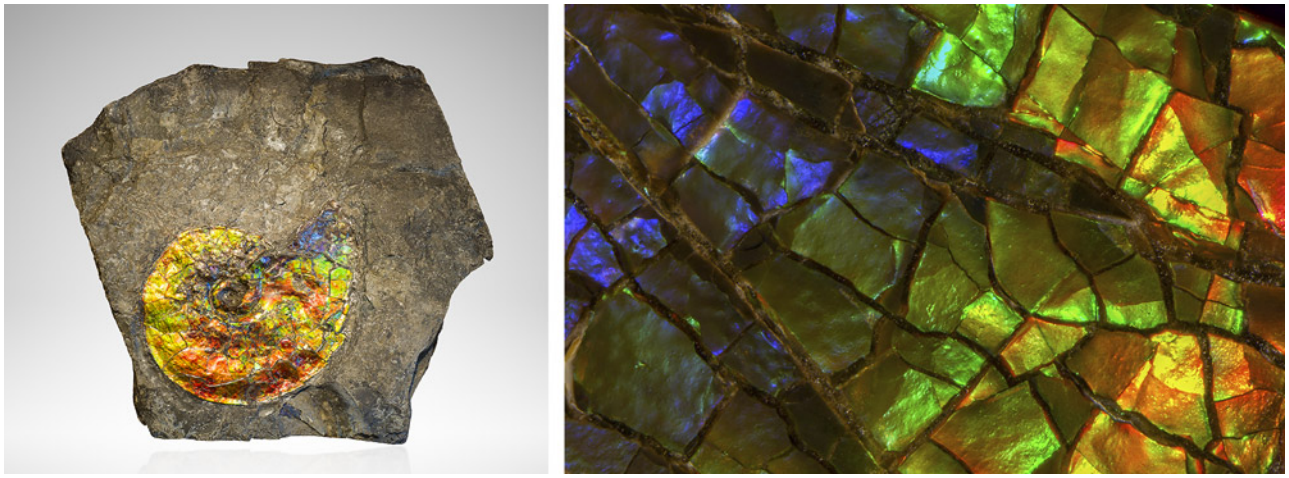

lization through precipitation, exsolution, or chemical alteration. Crystals formed in equilibrium are normally homogeneous without any internal texture. Cooling, decompression, and changing oxygen fugacity can push a homogeneous crystal out of equilibrium to start unmixing or reacting with its surroundings. These diffusion-controlled solid-state reactions are typically very slow, which restricts the scale of the inclusions and exsolution textures to sizes small enough to scatter or diffract visible light.

The primary heterogeneities in gemstones typically form directly through nonequilibrium processes. Low-temperature mineralization (e.g., agate and opal) is often disequilibrated by kinetic barriers, with the extreme case being biomineralization at ambient temperature (i.e., shells and pearls). Nonequilibrium processes can also occur at higher temperatures due to drastically changing temperature, pressure, or chemistry. For instance, rapid crystal growth can create linear defects such as growth tubes in pegmatite minerals, and rapid quenching of flowing lava can form flattened gas bubbles in sheen obsidian.

The degree of disequilibration strongly affects the form of optical phenomena in gemstones. Phenomenal gemstones that formed slowly at high temperatures, through magmatism or metamorphism, typically have a more pervasive and uniform appearance, such as asteriated corundum and iridescent feldspars. On the other hand, those formed at lower temperatures, or rapidly within a short period of time, are often more heterogeneous and disorganized, such as iris agate and fire obsidian. Perhaps the most enigmatic aspect of the phenomenal gemstone formation is the fine line between order and randomness. For instance, how do opal and agate textures switch rapidly back and forth between vibrant play-of-color and dull milky scattering within the same specimen? Why do pearls and shells from the same species display such different iridescent colors?

All optical phenomena in gemstones can be described as diffraction of light by their submicron inclusions or textures with broadly variable sizes and shapes. The diffraction pattern is the reciprocal of the light-diffracting particle, meaning the more extended the particle is in a certain dimension, the more confined the diffracted light is in that direction. The nanoparticles in fancy white diamonds and milky sapphires are zero-dimensional particles, which scatter light evenly in every direction in three-dimensional space. The one-dimensional needles in chatoyant and asteriated gemstones diffract light into a two-dimensional cone. The two-dimensional plates and layers in aventurescent and schillerized gemstones reflect light in a fixed direction, with one remaining degree of freedom (the incident angle can still change). The diffraction condition of the three-dimensional photonic crystals is restricted to zero dimension (to use the terminology of X-ray crystallography, the reciprocal space of a 3D periodic structure consists of arrays of discrete zero-dimensional spots, meaning that the diffracted beam can only be observed when the incident angle, diffraction angle, and wavelength satisfy a very specific condition with zero degrees of freedom).

The optical effects of phenomenal gemstones are described only qualitatively in this article. However, just as crystal structures can be determined and refined from XRD patterns, the optical properties can quantitatively reveal the submicron structures and textures of minerals. For instance, the iridescence spectrum can be used to calculate the lamellae thickness distribution in labradorite and peristerite, and the particle size and density in milky sapphires or copper feldspars can be quantified by measuring the scattering intensity in different directions. Unfortunately, despite the immense research focus on biomimetic photonic materials, there have been few attempts to quantify the submicron structures in minerals using their optical properties. Admittedly, such measurements can be quite challenging due to the heterogeneity and irregular shapes commonly found in natural materials. Nonetheless, as powerful as modern electron microscopes are, they can provide only two-dimensional information for surfaces and cross sections, whereas optical diffraction and spectroscopy can characterize the textures in three dimensions. Hopefully the studies of optical phenomena in gemstones can inspire new analytical techniques for characterizing three-dimensional structures and textures of both synthetic and natural nanomaterials.

For videos of phenomenal gemstones, visit: gia.edu/gems-gemology/summer-2025-phenomenal-gemstones

ABOUT THE AUTHORS
Dr. Shiyun Jin is a senior research scientist, Nathan D. Renfro is senior manager of colored stone identification, Dr. Aaron C. Palke is senior manager of research, and Dr. James E. Shigley is a distinguished research fellow, at GIA in Carlsbad, California.

ACKNOWLEDGMENTS
The authors thank Peter Heaney and an anonymous reviewer for many constructive comments and suggestions. The authors are deeply grateful to everyone who contributed the photographs and images used in this article. Special thanks to John I. Koivula, Rachelle Turnier, and McKenzie Santimer for providing many of the specimens from personal and museum collections, and to Emily Lane and Annie Haynes for their photography and photo editing. We would also like to thank Artitaya Homkrajae for sharing her expertise in pearls and shells, which helped clarify some of the terminology for these organic gems.

REFERENCES

Abduriyim A. (2009) The characteristics of red andesine from the Himalaya Highland, Tibet. *Journal of Gemmology*, Vol. 31, No. 5–8, pp. 283–298.

Abduriyim A., McClure S.F., Rossman G.R., Leelawatanasuk T., Hughes R.W., Laurs B.M., Lu R., Isatelle F., Scarratt K., Dubinsky E.V., Douthit T.R., Emmett J.L. (2011) Research on gem feldspar from the Shigatse Region of Tibet. *G&G*, Vol. 47, No. 2, pp. 167–180.

Ague J.J., Eckert J.O. (2012) Precipitation of rutile and ilmenite needles in garnet: Implications for extreme metamorphic conditions in the Acadian Orogen, U.S.A. *American Mineralogist*, Vol. 97, No. 5-6, pp. 840–855, http://dx.doi.org/10.2138/am.2012.4015

Andersen O. (1915) On aventurine feldspar. *American Journal of Science*, Vol. s4-40, No. 238, pp. 351–399, http://dx.doi.org/10.2475/ajs.s4-40.238.351

Appel P.W.U., Jensen A. (1987) A new gem material from Greenland: Iridescent orthoamphibole. *G&G*, Vol. 23, No. 1, pp. 36–42, http://dx.doi.org/10.5741/GEMS.23.1.36

Applin K.R., Hicks B.D. (1987) Fibers of dumortierite in quartz. *American Mineralogist*, Vol. 72, No. 1-2, pp. 170–172.

Arnon Z.A., Pinotsi D., Schmidt M., Gilead S., Guterman T., Sadhanala A., Ahmad S., Levin A., Walther P., Kaminski C.F., Fändrich M., Kaminski Schierle G.S., Adler-Abramovich L., Shimon L.J.W., Gazit E. (2018) Opal-like multicolor appearance of self-assembled photonic array. *ACS Applied Materials & Interfaces*, Vol. 10, No. 24, pp. 20783–20789, http://dx.doi.org/10.1021/acsami.8b04912

Au C.Y.W. (2022) Lab Notes: Calcite found on the surface of a saltwater "nacreous" pearl. *G&G*, Vol. 58, No. 4, pp. 477–478.

Axler J.A., Ague J.J. (2015) Oriented multiphase needles in garnet from ultrahigh-temperature granulites, Connecticut, U.S.A. *American Mineralogist*, Vol. 100, No. 10, pp. 2254–2271, http://dx.doi.org/10.2138/am-2015-5018

Badar M.A., Akizuki M. (1997) Iridescent andradite garnet from the Sierra Madre Mountains, Sonora, Mexico. *Neues Jahrbuch für Mineralogie - Monatshefte*, Vol. 1997, No. 12, pp. 529–539, http://dx.doi.org/10.1127/njmm/1997/1997/529

Badar M.A., Akizuki M., Hussain S. (2010) Optical anomaly in iridescent andradite from the Sierra Madre Mountains, Sonora, Mexico. *Canadian Mineralogist*, Vol. 48, No. 5, pp. 1195–1203, http://dx.doi.org/10.3749/canmin.48.5.1195

Bailey S.W. (1977) Report of the I.M.A.-I.U.Cr. Joint Committee on Nomenclature. *American Mineralogist*, Vol. 62, No. 5-6, pp. 411–415.

Baldwin L.C., Tomaschek F., Ballhaus C., Gerdes A., Fonseca R.O.C., Wirth R., Geisler T., Nagel T. (2017) Petrogenesis of alkaline basalt-hosted sapphire megacrysts. Petrological and geochemical investigations of in situ sapphire occurrences from the Siebengebirge Volcanic Field, Germany. *Contributions to Mineralogy and Petrology*, Vol. 172, No. 6, article no. 43, http://dx.doi.org/10.1007/s00410-017-1362-0

Ball R.A. (1982) Further studies on iridescence of marine shells. *Australian Gemmologist*, Vol. 14, No. 10, pp. 266–271.

Barry J.C., Bursill L.A., Hutchison J.L., Lang A.R., Rackham G.M., Sumida N. (1987) On voidites: A high-resolution transmission electron microscopic study of faceted void-like defects in natural diamonds. *Philosophical Transactions of the Royal Society of London. Series A, Mathematical and Physical Sciences*, Vol. 321, No. 1560, pp. 361–401, http://dx.doi.org/10.1098/rsta.1987.0018

Baryshev A.V., Kaplyanskii A.A., Kosobukin V.A., Limonov M.F., Samusev K.B., Usvyat D.E. (2003a) Bragg diffraction of light in high-quality synthetic opals. *Physica E: Low-dimensional Systems and Nanostructures*, Vol. 17, pp. 426–428, http://dx.doi.org/10.1016/S1386-9477(02)00905-0

——— (2003b) Bragg diffraction of light in synthetic opals. *Physics of the Solid State*, Vol. 45, No. 3, pp. 459–471, http://dx.doi.org/10.1134/1.1562231

Baryshev A.V., Kosobukin V.A., Samusev K.B., Usvyat D.E., Limonov M.F. (2006) Light diffraction from opal-based photonic crystals with growth-induced disorder: Experiment and theory. *Physical Review B*, Vol. 73, No. 20, article no. 205118, http://dx.doi.org/10.1103/PhysRevB.73.205118

Bernauer F. (1927) Uber zickzackbanderung (Runzelbänderung) und verwandle polarisation serscheinungen an kristallen und kristallaggregation. *Neues Jahrbuch für Mineralogie, Geologie und Palaeontologie, Beilageband*, Vol. 55, pp. 92–143.

Bian G., Ageeva O., Rečnik A., Habler G., Abart R. (2021) Formation pathways of oriented magnetite micro-inclusions in plagioclase from oceanic gabbro. *Contributions to Mineralogy and Petrology*, Vol. 176, No. 12, article no. 104, http://dx.doi.org/10.1007/s00410-021-01864-8

Bian G., Ageeva O., Roddatis V., Habler G., Schreiber A., Abart R. (2023) Oriented secondary magnetite micro-inclusions in plagioclase from oceanic gabbro. *American Mineralogist*, Vol. 108, No. 9, pp. 1642–1657, http://dx.doi.org/10.2138/am-2022-8784

Bøggild O.B. (1924) On the labradorization of the feldspars. *Mathematisk-Fysiske Meddelelser*, Vol. 6, pp. 1–79.

Bohren C.F., Huffman D.R. (1998) *Absorption and Scattering of Light by Small Particles*. John Wiley & Sons, Ltd, Mörlenbach, Germany.

Bolton H.C., Bursill L.A., McLaren A.C., Turner R.G. (1966) On the origin of the colour of labradorite. *Physica Status Solidi (B)*, Vol. 18, No. 1, pp. 221–230, http://dx.doi.org/10.1002/pssb.19660180123

Boyd S.R., Kiflawi I., Woods G.S. (1995) Infrared absorption by the B nitrogen aggregate in diamond. *Philosophical Magazine B*, Vol. 72, No. 3, pp. 351–361, http://dx.doi.org/10.1080/13642819508239089

Breebaart A.J. (1958) Synthetic moonstone—Coloured spinel. *Journal of Gemmology*, Vol. 6, No. 5, pp. 213–214.

Brewster D. (1813) XIII. On some properties of light. *Philosophical*

Transactions of the Royal Society of London, Vol. 103, pp. 101–109, http://dx.doi.org/10.1098/rstl.1813.0016
——— (1833) *A Treatise on Optics*. Carey, Lea, & Blanchard, Philadelphia.
——— (1843) On the cause of the colour in iris agate. *Philosophical Magazine*, Vol. 22, pp. 434–435.
Brink D.J., van der Berg N.G. (2005) An investigation of green iridescence on the mollusc *Patella granatina*. *Journal of Physics D: Applied Physics*, Vol. 38, No. 2, article no. 338, http://dx.doi.org/10.1088/0022-3727/38/2/019
Brink D.J., van der Berg N.G., Botha A.J. (2002) Iridescent colors on seashells: An optical and structural investigation of *Helcion pruinosus*. *Applied Optics*, Vol. 41, No. 4, pp. 717–722, http://dx.doi.org/10.1364/AO.41.000717
Brown L.D. (2005) Characterisation of Australian Opals. PhD thesis, University of Technology Sydney, Ultimo, Australia.
Buckley A.N., Woods R. (1983) X-ray photoelectron spectroscopic investigation of the tarnishing of bornite. *Australian Journal of Chemistry*, Vol. 36, No. 9, pp. 1793–1804, http://dx.doi.org/10.1071/ch9831793
Bui T.N., Deliousi K., Malik T.K., De Corte K. (2015) From exsolution to 'gold sheen': A new variety of corundum. *Journal of Gemmology*, Vol. 34, No. 8, pp. 678–691.
Bui T.N., Entremont P., Gauthier J.-P. (2017) Large 12-rayed black star sapphire from Sri Lanka with asterism caused by ilmenite inclusions. *Journal of Gemmology*, Vol. 35, No. 5, pp. 430–435.
Bui T.N., Entremont P., Mazzero F., Gauthier J.-P. (2020) Stereoscopy in asteriated gemstones revisited. *Journal of Gemmology*, Vol. 37, No. 3, pp. 298–305.
Cartier R. (2009) Optical phenomena in gemstones. *Australian Gemmologist*, Vol. 23, No. 10, pp. 447–449.
Challener S., Renfro N.D., Sun Z. (2017) Micro-World: New phenomenal feldspar from North Carolina with iridescent inclusions. *G&G*, Vol. 53, No. 4, p. 467.
Champness P.E., Lorimer G.W. (1976) Exsolution in silicates. In H.-R. Wenk, Ed., *Electron Microscopy in Mineralogy*. Springer, Berlin, Heidelberg, pp. 174–204, http://dx.doi.org/10.1007/978-3-642-66196-9_9
Champness P.E., Rodgers K.A. (2000) The origin of iridescence in anthophyllite-gedrite from Simiuttat, Nuuk district, southern West Greenland. *Mineralogical Magazine*, Vol. 64, No. 5, pp. 885–889, http://dx.doi.org/10.1180/002646100549715
Choudhary G. (2008) Aventurine K-feldspar. *Journal of Gems & Gemmology*, Vol. 10, No. 3, pp. 20–22.
——— (2011) Gem News International: Pink cat's-eye quartz, with color and chatoyancy caused by tourmaline needles. *G&G*, Vol. 47, No. 3, pp. 245–246.
——— (2013) Gem News International: Zoned scapolite from India. *G&G*, Vol. 49, No. 1, pp. 58–59.
Choudhary G., Vyas M.B. (2009) "Multiphenomenal" quartz from India. *Gems & Jewellery*, Vol. 18, No. 1, pp. 10–12.
Christie O.H.J., Olsen A. (1974) Spinodal precipitation in minerals. Review and some new observations. *Bulletin de Minéralogie*, Vol. 97, No. 2, pp. 202–205, http://dx.doi.org/10.3406/bulmi.1974.6879
Colony R.J. (1935) Schiller structure. *American Mineralogist*, Vol. 20, No. 12, pp. 828–837.
Copley P.A., Gay P. (1978) A scanning electron microscope investigation of some Norwegian aventurine feldspars. *Norsk Geologisk Tidsskrift*, Vol. 58, No. 1, pp. 93–95.
——— (1979) Crystallographic studies of some Norwegian aventurinised feldspars by optical, X-ray, and electron optical methods. *Norsk Geologisk Tidsskrift*, Vol. 59, No. 3, pp. 229–237.
——— (1982) The heat treatment of some Norwegian aventurinized feldspars. *Mineralogical Magazine*, Vol. 45, No. 337, pp. 107–110, http://dx.doi.org/10.1180/minmag.1982.045.337.12
Curtis N.J., Gascooke J.R., Johnston M.R., Pring A. (2019) A review of the classification of opal with reference to recent new localities. *Minerals*, Vol. 9, No. 5, article no. 299, http://dx.doi.org/10.3390/min9050299
Darragh P.J., Sanders J.V. (1965) Origin of colour in opal based on electron microscopy. *Australian Gemmologist*, Vol. 7, pp. 9–12.
Dietrich R.V., White J.S., Nelen J.E., Chyi K.-L. (1988) A gem-quality iridescent orthoamphibole from Wyoming. *G&G*, Vol. 24, No. 3, pp. 161–164, http://dx.doi.org/10.5741/GEMS.24.3.161
Divljan S. (1960) The results of field and laboratory studies of aventurine plagioclases from some Norwegian pegmatites. In: *Proceedings of the 21st International Geological Congress, Norden*. pp. 94–101.
Drev S., Komelj M., Mazaj M., Daneu N., Rečnik A. (2015) Structural investigation of (130) twins and rutile precipitates in chrysoberyl crystals from Rio das Pratinhas in Bahia (Brazil). *American Mineralogist*, Vol. 100, No. 4, pp. 861–871, http://dx.doi.org/10.2138/am-2015-5120
Durán A., Fernández Navarro J.M., García Solé J., Agulló-López F. (1984) Study of the colouring process in copper ruby glasses by optical and EPR spectroscopy. *Journal of Materials Science*, Vol. 19, No. 5, pp. 1468–1475, http://dx.doi.org/10.1007/BF00563041
Eaton-Magaña S., Ardon T., Breeding C.M., Shigley J.E. (2019) Natural-color fancy white and fancy black diamonds: Where color and clarity converge. *G&G*, Vol. 55, No. 3, pp. 320–337, http://dx.doi.org/10.5741/GEMS.55.3.320
Ediriweera R.N., Perera S.I., Phil M. (1989) Heat treatment of Geuda stones – Spectral investigation. *Journal of Gemmology*, Vol. 21, No. 7, pp. 403–404.
Emmett J.L., Douthit T.R. (2009) *Copper Diffusion in Plagioclase*. GIA News from Research, https://www.gia.edu/doc/Cu-diffusion-Emmett.pdf
Emori K., Oto S., Igami Y., Uzuhashi J., Ohkubo T., Kitawaki H., Miyake A. (2024) Nano-inclusions associated with beryllium in untreated blue sapphires from Diego Suarez, Madagascar. *Journal of Gemmology*, Vol. 39, No. 4, pp. 364–372.
Eppler W.F. (1958) Notes on asterism in corundum, rose quartz and almandine garnet, and chatoyancy in beryl. *Journal of Gemmology*, Vol. 6, No. 5, pp. 195–212.
Evans T., Kiflawi I., Luyten W., van Tendeloo G., Woods G.S. (1995) Conversion of platelets into dislocation loops and voidite formation in type IaB diamonds. *Proceedings of the Royal Society of London. Series A: Mathematical and Physical Sciences*, Vol. 449, No. 1936, pp. 295–313, http://dx.doi.org/10.1098/rspa.1995.0045
Fan N., Zhou C., Myagkaya E. (2021) Investigation of nacre nanostructure by analyzing its structural color pattern. *Scientific Reports*, Vol. 11, No. 1, article no. 19686, http://dx.doi.org/10.1038/s41598-021-99327-4
Farfan G., Xu H. (2008) Pleochroism in calcic labradorite from Oregon: Effects from size and orientation of nano- and micro-precipitates of copper and pyroxene. *Geochimica et Cosmochimica Acta*, Vol. 72, No. 12, p. A256. Presented at the Goldschmidt Conference, Vancouver, British, Columbia, Canada.
Fitz Gerald J.D., Parsons I., Cayzer N. (2006) Nanotunnels and pull-aparts: Defects of exsolution lamellae in alkali feldspars. *American Mineralogist*, Vol. 91, No. 5-6, pp. 772–783, http://dx.doi.org/10.2138/am.2006.2029
Freestone I. (1987) Composition and microstructure of early opaque red glass. In M. Bimson and I. Freestone, Eds., *Early Vitreous Materials British Museum Occasional Paper 56*, British Museum, London, pp. 173–191.
Freestone I., Meeks N., Sax M., Higgitt C. (2007) The Lycurgus Cup—A Roman nanotechnology. *Gold Bulletin*, Vol. 40, No. 4, pp. 270–277, http://dx.doi.org/10.1007/BF03215599
Frondel C. (1954) Commercial synthesis of star sapphires and star rubies. *Transactions of the American Institute of Mining and*

Metallurgical Engineers, Vol. 199, No. 1, pp. 78–80.
Gaillou E. (2015) An overview of gem opals: From the geology to color and microstructure. In *Thirteenth Annual Sinkankas Symposium—Opal*, Pala International, Inc., pp. 10–19.
Gaillou E., Fritsch E., Aguilar-Reyes B., Rondeau B., Post J., Barreau A., Ostroumov M. (2008) Common gem opal: An investigation of micro- to nano-structure. *American Mineralogist*, Vol. 93, No. 11-12, pp. 1865–1873, http://dx.doi.org/10.2138/am.2008.2518
Gao Y., Merkle K.L., Chang H.L., Zhang T.J., Lam D.J. (1992) Study of defects and interfaces on the atomic scale in epitaxial TiO_2 thin films on sapphire. *Philosophical Magazine A*, Vol. 65, No. 5, pp. 1103–1125, http://dx.doi.org/10.1080/01418619208201499
Gauthier J.-P., Fritsch E., Bui T.N., Fereire J. (2023) Clues to understanding the enigma of the unusual asterism in "Mercedes-star" quartz. *Journal of Gemmology*, Vol. 38, No. 7, pp. 678–695.
Gittos M.F., Lorimer G.W., Champness P.E. (1976) The phase distributions in some exsolved amphiboles. In H.-R. Wenk, Ed., *Electron Microscopy in Mineralogy*. Springer, Berlin, Heidelberg, pp. 238–247, http://dx.doi.org/10.1007/978-3-642-66196-9_16
Giuliani G., Ohnenstetter D., Fallick A.E., Groat L., Fagan A.J. (2014) Chapter 2: The Geology and Genesis of Gem Corundum Deposits. In L.A. Groat, Ed., *Geology of Gem Deposits, Second Edition*. Mineralogical Association of Canada, pp. 29–112, http://dx.doi.org/10.3749/9780921294696.ch02
Goreva J.S., Ma C., Rossman G.R. (2001) Fibrous nanoinclusions in massive rose quartz: The origin of rose coloration. *American Mineralogist*, Vol. 86, No. 4, pp. 466–472, http://dx.doi.org/10.2138/am-2001-0410
Götze J., Möckel R., Pan Y. (2020) Mineralogy, geochemistry and genesis of agate—A review. *Minerals*, Vol. 10, No. 11, article no. 1037, http://dx.doi.org/10.3390/min10111037
Gouzy S., Rondeau B., Vinogradoff V., Chauviré B., Coulet M.-V., Grauby O., Terrisse H., Carter J. (2024) Opal synthesis: Toward geologically relevant conditions. *Minerals*, Vol. 14, No. 10, article no. 969, https://dx.doi.org/10.3390/min14100969
Griffiths T.A., Habler G., Abart R. (2020) Determining the origin of inclusions in garnet: Challenges and new diagnostic criteria. *American Journal of Science*, Vol. 320, No. 9, pp. 753–789, http://dx.doi.org/10.2475/11.2020.01
Gu T., Ohfuji H., Wang W. (2019) Origin of milky optical features in type IaB diamonds: Dislocations, nano-inclusions, and polycrystalline diamond. *American Mineralogist*, Vol. 104, No. 5, pp. 652–658, http://dx.doi.org/10.2138/am-2019-6699
Gu T., Wang W. (2018) Optical defects in milky type IaB diamonds. *Diamond and Related Materials*, Vol. 89, pp. 322–329, http://dx.doi.org/10.1016/j.diamond.2018.09.010
Gübelin E.J., Koivula J.I. (2005) *Photoatlas of Inclusions in Gemstones*, Vol. 2, Opinio Verlag, Basel, Switzerland.
Guinel M.J.-F., Norton M.G. (2006) The origin of asterism in almandine-pyrope garnets from Idaho. *Journal of Materials Science*, Vol. 41, No. 3, pp. 719–725, http://dx.doi.org/10.1007/s10853-006-6500-4
Gunaratne H.S. (1981) Geuda sapphires – Their colouring elements and their reaction to heat. *Journal of Gemmology*, Vol. 17, No. 5, pp. 292–300.
Guo D.-J. (2010) Microstructure and crystallography of abalone shells. Masters thesis, University of Glasgow, Glasgow, Scotland.
Hainschwang T., Notari F. (2006) The cause of iridescence in rainbow andradite from Nara, Japan. *G&G*, Vol. 42, No. 4, pp. 248–258, http://dx.doi.org/10.5741/GEMS.42.4.248
Hänni H.A., Koivula J.I., Tannous M. (2003) Gem News International: Star sunstone from Tanzania. *G&G*, Vol. 39, No. 3, pp. 235–236.
He J. (2006) Precipitation in titanium-doped sapphire. PhD thesis, Case Western Reserve University, Cleveland, OH, USA.
He J., Lagerlof K.P.D., Heuer A.H. (2011) Structural evolution of TiO_2 precipitates in Ti-doped sapphire (α-Al_2O_3). *Journal of the American Ceramic Society*, Vol. 94, No. 4, pp. 1272–1280, http://dx.doi.org/10.1111/j.1551-2916.2010.04217.x
Heaney P.J. (1993) A proposed mechanism for the growth of chalcedony. *Contributions to Mineralogy and Petrology*, Vol. 115, No. 1, pp. 66–74, http://dx.doi.org/10.1007/BF00712979
——— (2021) Iris agates and cantor dusts: The textural complexity of agates. *Seventeenth Annual Sinkankas Symposium—Agate and Chalcedony*. Pala International, Inc., pp. 29–39.
Heaney P.J., Fisher D.M. (2003) New interpretation of the origin of tiger's-eye. *Geology*, Vol. 31, No. 4, pp. 323–326, http://dx.doi.org/10.1130/0091-7613(2003)031<0323:NIOTOO>2.0.CO;2
Heaney P.J., Post J.E., Chen S.A., Clark T., Wenzel T., Jacucci G., Vignolini S. (2018) Painting a rainbow with ochre: Iridescence in botryoidal goethite. Presented at the GSA Annual Meeting, GSA, Indianapolis, Indiana, USA, http://dx.doi.org/10.1130/abs/2018AM-318614
Hernández-Ortiz M., Hernández-Padrón G., Bernal R., Cruz-Vázquez C., Castaño V. (2015) Nanocrystalline mimetic opals: Synthesis and comparative characterization vs. natural stones. *International Journal of Basic and Applied Sciences*, Vol. 4, No. 2, pp. 238–243, http://dx.doi.org/10.14419/ijbas.v4i2.4174
Hodgkinson A. (2017) Moonstone mystery. *Journal of Gemmology*, Vol. 35, No. 5, pp. 378–380.
Hofmeister A.M., Rossman G.R. (1983) Color in feldspars. In P.H. Ribbe, Ed., *Feldspar Mineralogy*. Mineralogical Society of America, Washington, D.C., pp. 271–280, http://dx.doi.org/10.1515/9781501508547-016
Hu K., Heaney P.J. (2010) A microstructural study of pietersite from Namibia and China. *G&G*, Vol. 46, No. 4, pp. 280–286, http://dx.doi.org/10.5741/GEMS.46.4.280
Hughes E.B. (2018) Micro-World: Star spinel with four and six rays. *G&G*, Vol. 54, No. 2, p. 230.
Hwang S.L., Shen P., Chu H.T., Yui T.F., Iizuka Y. (2013) A TEM study of the oriented orthopyroxene and forsterite inclusions in garnet from Otrøy garnet peridotite, WGR, Norway: New insights on crystallographic characteristics and growth energetics of exsolved pyroxene in relict majoritic garnet. *Journal of Metamorphic Geology*, Vol. 31, No. 2, pp. 113–130, http://dx.doi.org/10.1111/jmg.12002
——— (2015) Origin of rutile needles in star garnet and implications for interpretation of inclusion textures in ultrahigh-pressure metamorphic rocks. *Journal of Metamorphic Geology*, Vol. 33, No. 3, pp. 249–272, http://dx.doi.org/10.1111/jmg.12119
Hwang S.-L., Shen P., Yui T.-F., Chu H.-T. (2010) On the coherency-controlled growth habit of precipitates in minerals. *Journal of Applied Crystallography*, Vol. 43, No. 3, pp. 417–428, http://dx.doi.org/10.1107/S0021889810007454
Hyršl J. (2001) Some new unusual cat's-eyes and star stones. *Journal of Gemmology*, Vol. 27, No. 8, pp. 456–460.
Ignatov S.I., Platonov A.N., Sedenko V.S., Taran M.N. (1990) Pozheve zabravlennya kvarcu, zvyazane z mikrovklyuchennyami dumortyeritu. *Dopovidi Akademii nauk Ukrainskoi RSR, Seriia B: Heolohichni, khimichni ta biolohichni nauky*, Vol. 7, pp. 23–26.
Ingerson E., Barksdale J.D. (1943) Iridescent garnet from the Adelaide Mining District, Nevada. *American Mineralogist*, Vol. 28, No. 5, pp. 303–312.
Izokh A.E., Smirnov S.Z., Egorova V.V., Anh T.T., Kovyazin S.V., Phuong N.T., Kalinina V.V. (2010) The conditions of formation of sapphire and zircon in the areas of alkali-basaltoid volcanism in Central Vietnam. *Russian Geology and Geophysics*, Vol. 51, No. 7, pp. 719–733, http://dx.doi.org/10.1016/j.rgg.2010.06.001
Jayaram V. (1988) The precipitation of alpha-TiO_2 from supersaturated solutions of Ti in alumina crystal structure and morphology. *Philosophical Magazine A*, Vol. 57, No. 3, pp.

525–542, http://dx.doi.org/10.1080/01418618808204683
Jayaraman A. (1953) The structure and optical behaviour of chalcedony. *Proceedings of the Indian Academy of Sciences – Section A*, Vol. 38, No. 6, pp. 441–449, http://dx.doi.org/10.1007/BF03045262
Jin S., Palke A.C., Renfro N.D., Sun Z. (2023) Special colors and optical effects of Oregon sunstone: Absorption, scattering, pleochroism, and color zoning. *G&G*, Vol. 59, No. 3, pp. 298–322, http://dx.doi.org/10.5741/GEMS.59.3.298
Jin S., Saxey D.W., Quadir Z., Reddy S.M., Rickard W.D.A., Fougerouse D., Sun X., Palke A.C. (2024) Nanoparticles in natural beryllium-bearing sapphire: Incorporation and exsolution of high field strength elements in corundum. *Contributions to Mineralogy and Petrology*, Vol. 179, No. 12, article no. 110, http://dx.doi.org/10.1007/s00410-024-02189-y
Jin S., Sun Z., Palke A.C. (2022a) Color effects of Cu nanoparticles in Cu-bearing plagioclase feldspars. *American Mineralogist*, Vol. 107, No. 12, pp. 2188–2200, http://dx.doi.org/10.2138/am-2022-8325
——— (2022b) Iron oxide inclusions and exsolution textures of rainbow lattice sunstone. *European Journal of Mineralogy*, Vol. 34, No. 2, pp. 183–200, http://dx.doi.org/10.5194/ejm-34-183-2022
Jin S., Xu H., Lee S. (2021) Revisiting the Bøggild intergrowth in iridescent labradorite feldspars: Ordering, kinetics, and phase equilibria. *Minerals*, Vol. 11, No. 7, article no. 727, http://dx.doi.org/10.3390/min11070727
Johnson M.L., Koivula J.I. (1997) Gem News: "Rainbow" obsidian hearts. *G&G*, Vol. 33, No. 1, p. 63.
——— (1999) Gem News: Twelve-rayed star quartz from Sri Lanka. *G&G*, Vol. 35, No. 1, pp. 54–55.
Johnson M.L., McClure S.F. (1997) Lab Notes: Quartz: Cat's-eye effect caused by large rutile needles. *G&G*, Vol. 33, No. 1, p. 59.
Jones F.T. (1952) Iris agate. *American Mineralogist*, Vol. 37, No. 7-8, pp. 578–587.
Keller D.S., Ague J.J. (2019) Crystallographic and textural evidence for precipitation of rutile, ilmenite, corundum, and apatite lamellae from garnet. *American Mineralogist*, Vol. 104, No. 7, pp. 980–995, http://dx.doi.org/10.2138/am-2019-6849
——— (2020) Quartz, mica, and amphibole exsolution from majoritic garnet reveals ultra-deep sediment subduction, Appalachian orogen. *Science Advances*, Vol. 6, No. 11, article no. eaay5178, http://dx.doi.org/10.1126/sciadv.aay5178
——— (2022) Predicting and explaining crystallographic orientation relationships of exsolved precipitates in garnet using the edge-to-edge matching model. *Journal of Metamorphic Geology*, Vol. 40, No. 7, pp. 1189–1218, http://dx.doi.org/10.1111/jmg.12662
Khamloet P., Pisutha-Arnond V., Sutthirat C. (2014) Mineral inclusions in sapphire from the basalt-related deposit in Bo Phloi, Kanchanaburi, western Thailand: Indication of their genesis. *Russian Geology and Geophysics*, Vol. 55, No. 9, pp. 1087–1102, http://dx.doi.org/10.1016/j.rgg.2014.08.004
Kiefert L., Wang C., Sintayehu T., Link K. (2019) Gem Notes: Sunstone labradorite-bytownite from Ethiopia. *Journal of Gemmology*, Vol. 36, No. 8, pp. 694–695.
Kiflawi I., Bruley J. (2000) The nitrogen aggregation sequence and the formation of voidites in diamond. *Diamond and Related Materials*, Vol. 9, No. 1, pp. 87–93, http://dx.doi.org/10.1016/S0925-9635(99)00265-4
Killingback H. (2005) Stereoscopic effect in asterism and chatoyancy. *Journal of Gemmology*, Vol. 29, No. 5-6, pp. 312–315.
——— (2006) Diasterism in rose quartz. *Gems & Jewellery*, Vol. 15, No. 3, p. 64.
——— (2015) The "coffee-and-cream" effect in chatoyant cabochons. *Journal of Gemmology*, Vol. 34, No. 6, pp. 524–530.
Kinoshita S. (2008) *Structural Colors in the Realm of Nature*. World Scientific Publishing, Singapore.
Koivula J.I. (1987) Gem News: "Rainbow moonstones" are labradorite. *G&G*, Vol. 23, No. 3, p. 175.
Koivula J.I., Kammerling R.C. (1989a) Gem News: A beautiful new form of orthoclase. *G&G*, Vol. 25, No. 1, p. 47.
Koivula J.I., Kammerling R.C., Fritsch E. (1993) Two interesting "double star" sapphires. *Australian Gemmologist*, Vol. 18, No. 7, pp. 235–236.
Kraeft U., Saalfeld H. (1967) Über die aventurin-oligoklase von Tvedestrand und Bjordam (Norwegen). *Swiss Mineralogical and Petrographic Bulletin*, Vol. 47, pp. 247–256, http://doi.org/10.5169/seals-36949
Kumaratilake W.L.D.R.A. (1997) Gems of Sri Lanka: A list of cat's-eyes and stars. *Journal of Gemmology*, Vol. 25, No. 7, pp. 474–482.
——— (1998) Spinel and garnet star networks: An interesting asterism in gems from Sri Lanka. *Journal of Gemmology*, Vol. 26, No. 1, pp. 24–28.
Lee M.R., Parsons I. (2015) Diffusion-controlled and replacement microtextures in alkali feldspars from two pegmatites: Perth, Ontario and Keystone, South Dakota. *Mineralogical Magazine*, Vol. 79, No. 7, pp. 1711–1735, http://dx.doi.org/10.1180/minmag.2015.079.7.21
Li L., Ortiz C. (2013) Biological design for simultaneous optical transparency and mechanical robustness in the shell of *Placuna placenta*. *Advanced Materials*, Vol. 25, No. 16, pp. 2344–2350, http://dx.doi.org/10.1002/adma.201204589
Lin X., Heaney P.J. (2017) Causes of iridescence in natural quartz. *G&G*, Vol. 53, No. 1, pp. 68–81, http://dx.doi.org/10.5741/GEMS.53.1.68
Lin X., Heaney P.J., Post J.E. (2018) Iridescence in metamorphic "rainbow" hematite. *G&G*, Vol. 54, No. 1, pp. 28–39, http://dx.doi.org/10.5741/GEMS.54.1.28
Liu J., Cao S., Zhou D., Li X., Wu Y., Wang H., Li W. (2022) Characteristics and formation of corundum within syenite in the Yushishan rare metal deposits in the northeastern Tibetan Plateau. *American Mineralogist*, Vol. 107, No. 12, pp. 2291–2306, http://dx.doi.org/10.2138/am-2022-8223
Liu J., Shen A.H., Zhang Z., Wang C., Shao T. (2018) Revisiting rainbow lattice sunstone from the Harts Range, Australia. *Journal of Gemmology*, Vol. 36, No. 1, pp. 44–52.
Liu Y., Hurwit K.N., Tian L. (2003) Relationship between the groove density of the grating structure and the strength of iridescence in mollusc shells. *Australian Gemmologist*, Vol. 21, No. 10, pp. 405–407.
Liu Y., Shigley J.E., Hurwit K.N. (1999) Iridescence color of a shell of the mollusk *Pinctada Margaritifera* caused by diffraction. *Optics Express*, Vol. 4, No. 5, pp. 177–182, http://dx.doi.org/10.1364/OE.4.000177
Ma C., Goreva J.S., Rossman G.R. (2002) Fibrous nanoinclusions in massive rose quartz: HRTEM and AEM investigations. *American Mineralogist*, Vol. 87, No. 2-3, pp. 269–276, http://dx.doi.org/10.2138/am-2002-2-308
Ma C., Gresh J., Rossman G.R., Ulmer G.C., Vicenzi E.P. (2001) Micro-analytical study of the optical properties of rainbow and sheen obsidians. *Canadian Mineralogist*, Vol. 39, No. 1, pp. 57–71, http://dx.doi.org/10.2113/gscanmin.39.1.57
Ma C., Rossman G.R., Miller J.A. (2007) The origin of color in "fire" obsidian. *Canadian Mineralogist*, Vol. 45, No. 3, pp. 551–557, http://dx.doi.org/10.2113/gscanmin.45.3.551
Mameli V., Musinu A., Niznansky D., Peddis D., Ennas G., Ardu A., Lugliè C., Cannas C. (2016) Much more than a glass: The complex magnetic and microstructural properties of obsidian. *Journal of Physical Chemistry C*, Vol. 120, No. 48, pp. 27635–27645, http://dx.doi.org/10.1021/acs.jpcc.6b08387
Mayerson W. (2001) Lab Notes: Sapphires with diffusion-induced stars. *G&G*, Vol. 37, No. 4, pp. 324–325.
McClure S.F. (1998) Lab Notes: Ruby, with a true double star. *G&G*, Vol. 34, No. 3, p. 217.
McMackin C.E. (1974) Fire agate – The rising star of the West. *Rocks & Minerals*, Vol. 49, No. 9, pp. 566–568, http://dx.doi.org/10.1080/00357529.1974.11762304

Mie G. (1908) Beiträge zur optik trüber medien, speziell kolloidaler metallösungen. *Annalen der Physik*, Vol. 330, No. 3, pp. 377–445, http://dx.doi.org/10.1002/andp.19083300302

Miura M., Katsurada Y., Saruwatari K. (2018) Gem News International: Update on trace-element chemical characteristics of golden sheen sapphire. *G&G*, Vol. 54, No. 2, pp. 238–241.

Moon A.R., Phillips M.R. (1984a) The physics of asterism in sapphire. *Swiss Mineralogical and Petrographic Bulletin*, Vol. 64, No. 3, pp. 329–334, http://dx.doi.org/10.5169/SEALS-49548

——— (1984b) An electron microscopy study of exsolved phases in natural black Australian sapphire. *Micron and Microscopica Acta*, Vol. 15, No. 3, pp. 143–146, http://dx.doi.org/10.1016/0739-6260(84)90044-3

——— (1985) Asterism—No mystery: A response to "Asterism—the Great Enigma." *Australian Gemmologist*, Vol. 15, No. 11, pp. 395–399.

——— (1991) Titania precipitation in sapphire containing iron and titanium. *Physics and Chemistry of Minerals*, Vol. 18, No. 4, pp. 251–258, http://dx.doi.org/10.1007/BF00202577

Moretti C., Gratuze B., Hreglich S. (2013) Goldstone of aventurine glass: History, recipes, analyses and manufacture. *Archeo-Sciences. Revue d'archéométrie*, No. 37, pp. 135–154, http://dx.doi.org/10.4000/archeosciences.4033

Moxon T., Palyanova G. (2020) Agate genesis: A continuing enigma. *Minerals*, Vol. 10, No. 11, article no. 953, http://dx.doi.org/10.3390/min10110953

Mychaluk K.A. (2009) Update on Ammolite production from Southern Alberta, Canada. *G&G*, Vol. 45, No. 3, pp. 192–196, http://dx.doi.org/10.5741/GEMS.45.3.192

Mychaluk K.A., Levinson A.A., Hall R.L. (2001) Ammolite: Iridescent fossilized Ammonite from Southern Alberta, Canada. *G&G*, Vol. 37, No. 1, pp. 4–25, http://dx.doi.org/10.5741/GEMS.37.1.4

Nakamura Y., Kuribayashi T., Nagase T., Imai H. (2017) Cation ordering in iridescent garnet from Tenkawa village, Nara prefecture, Japan. *Journal of Mineralogical and Petrological Sciences*, Vol. 112, No. 2, pp. 97–101, http://dx.doi.org/10.2465/jmps.161114a

Narudeesombat N., Saengbuangamlam S., Lhuaamporn T., Leelawatanasuk T. (2018) Golden sheen and non-sheen sapphires from Kenya. *Gem Quality Standards & Gem Optics and Color Science*, pp. 282–288.

Nassau K. (1968) On the cause of asterism in star corundum. *American Mineralogist*, Vol. 53, No. 1-2, pp. 300–305.

——— (1978) The origins of color in minerals. *American Mineralogist*, Vol. 63, No. 3-4, pp. 219–229.

Natkaniec-Nowak L., Dumańska-Słowik M., Gaweł A., Łatkiewicz A., Kowalczyk-Szpyt J., Wolska A., Milovská S., Luptáková J., Ładoń K. (2020) Fire agate from the Deer Creek deposit (Arizona, USA) – New insights into structure and mineralogy. *Mineralogical Magazine*, Vol. 84, No. 2, pp. 343–354, http://dx.doi.org/10.1180/mgm.2020.8

Navon O., Wirth R., Schmidt C., Jablon B.M., Schreiber A., Emmanuel S. (2017) Solid molecular nitrogen (δ-N_2) inclusions in Juina diamonds: Exsolution at the base of the transition zone. *Earth and Planetary Science Letters*, Vol. 464, pp. 237–247, http://dx.doi.org/10.1016/j.epsl.2017.01.035

Neumann H., Christie O.H.J. (1962) Observations on plagioclase aventurines from southern Norway. *Norsk Geologisk Tidsskrift*, Vol. 42, No. 2, pp. 389–393.

Newman R. (2014) *Exotic Gems, Volume 3: How to Identify, Evaluate, Select and Care for Matrix Opal, Fire Agate, Blue Chalcedony, Rubellite, Indicolite, Paraiba and Other Tourmalines*. International Jewelry Publications, Los Angeles, California.

Olsen J.S., Gerward L., Jiang J.Z. (1999) On the rutile/α-PbO_2-type phase boundary of TiO_2. *Journal of Physics and Chemistry of Solids*, Vol. 60, No. 2, pp. 229–233, http://dx.doi.org/10.1016/S0022-3697(98)00274-1

Ostwald J. (1965) Schiller and pseudochromatism in minerals and gemstones. *Journal of Gemmology*, Vol. 9, No. 9, pp. 309–324.

Ozaki R., Kikumoto K., Takagaki M., Kadowaki K., Odawara K. (2021) Structural colors of pearls. *Scientific Reports*, Vol. 11, No. 1, article no. 15224, http://dx.doi.org/10.1038/s41598-021-94737-w

Palke A.C., Breeding C.M. (2017) The origin of needle-like rutile inclusions in natural gem corundum: A combined EPMA, LA-ICP-MS, and nanoSIMS investigation. *American Mineralogist*, Vol. 102, No. 7, pp. 1451–1461, http://dx.doi.org/10.2138/am-2017-5965

Palke A.C., Saeseaw S., Renfro N.D., Sun Z., McClure S.F. (2019a) Geographic origin determination of blue sapphire. *G&G*, Vol. 55, No. 4, pp. 536–579, http://dx.doi.org/10.5741/GEMS.55.4.536

——— (2019b) Geographic origin determination of ruby. *G&G*, Vol. 55, No. 4, pp. 580–613, http://dx.doi.org/10.5741/GEMS.55.4.580

Parsons I. (2010) Feldspars defined and described: A pair of posters published by the Mineralogical Society. Sources and supporting information. *Mineralogical Magazine*, Vol. 74, No. 3, pp. 529–551, http://dx.doi.org/10.1180/minmag.2010.074.3.529

Parsons I., Brown W.L. (1984) Feldspars and the thermal history of igneous rocks. In W.L. Brown, Ed., *Feldspars and Feldspathoids: Structures, Properties and Occurrences*, NATO ASI Series. Springer Netherlands, Dordrecht, pp. 317–371, http://dx.doi.org/10.1007/978-94-015-6929-3_9

——— (1991) Mechanisms and kinetics of exsolution—Structural control of diffusion and phase behavior in alkali feldspars. In J. Ganguly, Ed., *Diffusion, Atomic Ordering, and Mass Transport*, Advances in Physical Geochemistry. Springer-Verlag New York, pp. 304–344, http://dx.doi.org/10.1007/978-1-4613-9019-0_10

Parsons I., Fitz Gerald J.D., Lee M.R. (2015) Routine characterization and interpretation of complex alkali feldspar intergrowths. *American Mineralogist*, Vol. 100, No. 5-6, pp. 1277–1303, http://dx.doi.org/10.2138/am-2015-5094

Perera S.I., Phil M., Pannila A.S., Gunasekera H.P.N.J., Ediriweera R.N. (1991) Anomalous behaviour of certain geuda corundums during heat treatment. *Journal of Gemmology*, Vol. 22, No. 7, pp. 405–407.

Petrov A., Tanaka Y. (2011) Iris Quartz. mindat.org, https://mindat.org/article.php/1335/Iris+Quartz, December 2023.

Pfund A.H. (1917) The colors of mother-of-pearl. *Journal of the Franklin Institute*, Vol. 183, No. 4, pp. 453–464, http://dx.doi.org/10.1016/S0016-0032(17)91045-2

Phillips D.S., Heuer A.H., Mitchell T.E. (1980) Precipitation in star sapphire I. Identification of the precipitate. *Philosophical Magazine A*, Vol. 42, No. 3, pp. 385–404, http://dx.doi.org/10.1080/01418618008239365

Promwongnan S., Ounorn P., Maneekrajangsaeng M., Leelawatanasuk T. (2017) Gem Notes: An unusual blue synthetic star spinel. *Journal of Gemmology*, Vol. 35, No. 6, pp. 500–502.

Proyer A., Habler G., Abart R., Wirth R., Krenn K., Hoinkes G. (2013) TiO_2 exsolution from garnet by open-system precipitation: Evidence from crystallographic and shape preferred orientation of rutile inclusions. *Contributions to Mineralogy and Petrology*, Vol. 166, No. 1, pp. 211–234, http://dx.doi.org/10.1007/s00410-013-0872-7

Radko V.A., Ananyev S.A., Petrochenkov D.A., Bondina S.S. (2021) Iridescent ammonite fossil shell material from Norilsk, Krasnoyarsk Krai, Russia. *Journal of Gemmology*, Vol. 37, No. 6, pp. 608–617.

Raman C.V. (1935) On iridescent shells: Part II. Colours of laminar diffraction. *Proceedings of the Indian Academy of Sciences – Section A*, Vol. 1, No. 9, pp. 574–589, http://dx.doi.org/10.1007/BF03035610

——— (1950a) The iridescent feldspars. *Current Science*, Vol. 19, No. 10, pp. 301–305.

——— (1950b) Crystals of quartz with iridescent faces. *Proceedings of the Indian Academy of Sciences – Section A*, Vol. 31, No. 5, pp. 275–279, http://dx.doi.org/10.1007/BF03050101
Raman C.V., Jayaraman A. (1950) The structure of labradorite and the origin of its iridescence. *Proceedings of the Indian Academy of Sciences – Section A*, Vol. 32, No. 1, article no. 1, http://dx.doi.org/10.1007/BF03172469
——— (1953a) The diffusion haloes of the iridescent feldspars. *Proceedings of the Indian Academy of Sciences – Section A*, Vol. 37, No. 1, pp. 1–10, http://dx.doi.org/10.1007/BF03052851
——— (1953b) The structure and optical behaviour of iridescent agate. *Proceedings of the Indian Academy of Sciences – Section A*, Vol. 38, No. 3, pp. 199–206, http://dx.doi.org/10.1007/BF03045221
——— (1955) On the optical behaviour of crypto-crystalline quartz. *Proceedings of the Indian Academy of Sciences – Section A*, Vol. 41, No. 1, pp. 1–6, http://dx.doi.org/10.1007/BF03050587
Renfro N.D. (2011a) Lab Notes: Synthetic star spinel imitation of moonstone. *G&G*, Vol. 47, No. 1, pp. 54–55.
——— (2011b) Gem News International: Nuummite from Mauritania. *G&G*, Vol. 47, No. 3, pp. 242–243.
——— (2019) Gem News International: Imitation opal with interesting play-of-color pattern. *G&G*, Vol. 55, No. 3, pp. 446–447.
Renfro N.D., Koivula J.I. (2011) Gem News International: Spectral interference in quartz from India. *G&G*, Vol. 47, No. 1, pp. 58–59.
Renfro N.D., Shigley J.E. (2018) Lab Notes: New plastic imitation opal from Kyocera. *G&G*, Vol. 54, No. 1, pp. 60–62.
Ribbe P.H. (1983) Exsolution textures in ternary and plagioclase feldspars; interference colors. In P.H. Ribbe, Ed., *Feldspar Mineralogy*. Mineralogical Society of America, Washington, D.C., pp. 241–270, http://dx.doi.org/10.1515/9781501508547-015
Rodgers K.A., Kinny P.D., McGregor V.R., Clark G.R., Henderson G.S. (1996) Iridescent anthophyllite-gedrite from Simiuttat, Nuuk district, southern West Greenland composition, exsolution, age. *Mineralogical Magazine*, Vol. 60, No. 403, pp. 937–947, http://dx.doi.org/10.1180/minmag.1996.060.403.08
Rossman G.R. (2011) The Chinese red feldspar controversy: Chronology of research through July 2009. *G&G*, Vol. 47, No. 1, pp. 16–30, http://dx.doi.org/10.5741/GEMS.47.1.16
Rossman G.R., Ma C. (2025) Iridescent iron oxides. *Minerals*, Vol. 15, No. 2, article no. 108, http://dx.doi.org/10.3390/min15020108
Saminpanya S. (2001) Ti-Fe mineral inclusions in star sapphires from Thailand. *Australian Gemmologist*, Vol. 21, No. 3, pp. 125–128.
Sanders J.V. (1964) Colour of precious opal. *Nature*, Vol. 204, pp. 1151–1153.
——— (1968) Diffraction of light by opals. *Acta Crystallographica Section A*, Vol. 24, No. 4, pp. 427–434, http://dx.doi.org/10.1107/S0567739468000860
——— (1976) The structure of star opals. *Acta Crystallographica Section A*, Vol. 32, No. 2, pp. 334–338, http://dx.doi.org/10.1107/S0567739476000727
Schmetzer K. (1988) Orientated lath-like inclusions of a new type in spinel. *Journal of Gemmology*, Vol. 21, No. 2, pp. 69–72.
Schmetzer K., Bernhardt H.-J. (2002) Star garnets from Ilakaka, Madagascar. *Australian Gemmologist*, Vol. 21, No. 5, pp. 202–206.
Schmetzer K., Bernhardt H.-J., Gilg H.A. (2016) Characterization of oriented inclusions in cat's-eye, star and other chrysoberyls. *Journal of Gemmology*, Vol. 35, No. 1, pp. 28–54.
Schmetzer K., Bernhardt H.-J., Hainschwang T. (2013) Titanium-bearing synthetic alexandrite and chrysoberyl. *Journal of Gemmology*, Vol. 33, No. 5-6, pp. 131–142.
Schmetzer K., Bernhardt H.-J., Kiefert L. (2002) Star garnets and star garnet cat's-eyes from Ambatondrazaka, Madagascar. *Journal of Gemmology*, Vol. 28, No. 1, pp. 13–24.
Schmetzer K., Glas M. (2003) Multi-star quartzes from Sri Lanka. *Journal of Gemmology*, Vol. 28, No. 6, pp. 321–332.
Schmetzer K., Gübelin E., Bernhardt H.-J., Kiefert L. (2000) Oriented inclusions in spinels from Madagascar. *Journal of Gemmology*, Vol. 27, No. 4, pp. 229–232.
Schmetzer K., Henn U. (1987) Synthetic or imitation? An investigation of the products of Kyocera Corporation that show play-of-color. *G&G*, Vol. 23, No. 3, pp. 148–151, http://dx.doi.org/10.5741/GEMS.23.3.148
Schmetzer K., Hodgkinson A. (2011) Synthetic star alexandrite. *Gems & Jewellery*, Vol. 20, No. 3, pp. 9–11.
Schmetzer K., Steinbach M.P. (2022) Gem Notes: Asteriated quartz sphere with sagenitic rutile inclusions. *Journal of Gemmology*, Vol. 38, No. 4, pp. 314–315.
——— (2023) Gem Notes: Three-rayed asterism in quartz: A multi-star network. *Journal of Gemmology*, Vol. 38, No. 6, pp. 552–553.
Schmetzer K., Steinbach M.P., Gilg H.A., Blake A.R. (2015) Dual-color double stars in ruby, sapphire, and quartz: Cause and historical account. *G&G*, Vol. 51, No. 2, pp. 112–143, http://dx.doi.org/10.5741/GEMS.51.2.112
Schumann W. (2009) *Gemstones of the World*. Sterling Publishing Company, Inc., New York.
Shen A.H. (2011) The nature of the Be-Nb-Ta containing cloud in natural Madagascar blue sapphire – An FIB/HRTEM study. GIA News from Research, https://www.gia.edu/gia-news-research/nano-inclusions-natural-sapphire
Shen A.H., Wirth R. (2012) Gem News International: Beryllium-bearing nano-inclusions identified in untreated Madagascar sapphire. *G&G*, Vol. 48, No. 2, pp. 150–151.
Shen C., Liao J. (2017) A study of gemological characteristics of ammolite. *Acta Petrologica Et Mineralogica*, Vol. 35, No. S1, pp. 111–118.
Shipley R.M. (1945) *Dictionary of Gems and Gemology*. Gemological Institute of America, Los Angeles, CA.
Shiryaev A.A., Chesnokov Y., Vasiliev A.L., Hainschwang T. (2023) Exsolution of oxygen impurity from diamond lattice and formation of pressurized CO_2-I precipitates. *Carbon Trends*, Vol. 11, article no. 100270, http://dx.doi.org/10.1016/j.cartre.2023.100270
Smith J.V. (1983) Phase equilibria of plagioclase. In P.H. Ribbe, Ed., *Feldspar Mineralogy*. Mineralogical Society of America, Washington, D.C., pp. 223–239, http://dx.doi.org/10.1515/9781501508547-014
Smith J.V., Brown W.L. (1988) *Feldspar Minerals: Crystal Structures, Physical, Chemical, and Microtextural Properties, Vol. 1*. Springer-Verlag, Berlin, Heidelberg.
Snow M.R., Pring A. (2005) The mineralogical microstructure of shells: Part 2.1 The iridescence colors of abalone shells. *American Mineralogist*, Vol. 90, No. 11-12, pp. 1705–1711, http://dx.doi.org/10.2138/am.2005.1788
Snow M.R., Pring A., Self P., Losic D., Shapter J. (2004) The origin of the color of pearls in iridescence from nano-composite structures of the nacre. *American Mineralogist*, Vol. 89, No. 10, pp. 1353–1358, http://dx.doi.org/10.2138/am-2004-1001
Sobolev N.V., Logvinova A.M., Tomilenko A.A., Wirth R., Bul'bak T.A., Luk'yanova L.I., Fedorova E.N., Reutsky V.N., Efimova E.S. (2019) Mineral and fluid inclusions in diamonds from the Urals placers, Russia: Evidence for solid molecular N_2 and hydrocarbons in fluid inclusions. *Geochimica et Cosmochimica Acta*, Vol. 266, pp. 197–219, http://dx.doi.org/10.1016/j.gca.2019.08.028
Soonthorntantikul W. (2014) Lab Notes: Star opal. *G&G*, Vol. 50, No. 2, pp. 152–153.
Soonthorntantikul W., Atikarnsakul U., Weeramongkhonlert V. (2016) Lab Notes: Update on spectroscopy of "gold sheen" sapphires. *G&G*, Vol. 52, No. 4, pp. 413–414.
Soonthorntantikul W., Vertriest W., Raynaud-Flattot V.L., Sangsawong S., Atikarnsakul U., Khowpong C., Weeramonkhonlert

V., Pardieu V. (2017) An in-depth gemological study of blue sapphires from the Baw Mar Mine (Mogok, Myanmar). *GIA News from Research*, https://www.gia.edu/gia-news-research/blue-sapphires-baw-mar-mine-mogok-myanmar

Sorokina E.S., Karampelas S., Nishanbaev T.P., Nikandrov S.N., Semiannikov B.S. (2017) Sapphire megacrysts in syenite pegmatites from the Ilmen Mountains, South Urals, Russia: New mineralogical data. *Canadian Mineralogist*, Vol. 55, No. 5, pp. 823–843, http://dx.doi.org/10.3749/canmin.1700016

Speich L., Kohn S.C., Wirth R., Bulanova G.P., Smith C.B. (2017) The relationship between platelet size and the B′ infrared peak of natural diamonds revisited. *Lithos*, Vol. 278-281, pp. 419–426, http://dx.doi.org/10.1016/j.lithos.2017.02.010

Sripoonjan T., Saengbuangamlam S., Maneekrajangsaeng M. (2019) Gem News International: Unique orange sapphire with golden sheen effect reportedly from Kenya. *G&G*, Vol. 55, No. 1, pp. 152–155.

Steinbach M.P. (2016) *Asterism: Gems with a Star*. MPS Publishing and Media, Idar-Oberstein, Germany.

——— (2018) An overview of asteriated gems: From common star sapphire to rare star aquamarine to one-of-a-kind star zircon. *G&G*, Vol. 54, No. 3, pp. 258–259.

Stöber W., Fink A., Bohn E. (1968) Controlled growth of monodisperse silica spheres in the micron size range. *Journal of Colloid and Interface Science*, Vol. 26, No. 1, pp. 62–69, http://dx.doi.org/10.1016/0021-9797(68)90272-5

Strutt R.J. (1923a) Studies of iridescent colour, and the structure producing it. III.—The colours of labrador felspar. *Proceedings of the Royal Society of London Series A*, Vol. 103, No. 720, pp. 34–45, http://dx.doi.org/10.1098/rspa.1923.0037

——— (1923b) Studies of iridescent colour, and the structure producing it.—II. Mother-of-pearl. *Proceedings of the Royal Society of London. Series A, Containing Papers of a Mathematical and Physical Character*, Vol. 102, No. 719, pp. 674–677, http://dx.doi.org/10.1098/rspa.1923.0025

Sun Z., Renfro N.D., Palke A.C. (2015) Gem News International: Iridescent scapolite. *G&G*, Vol. 51, No. 1, pp. 104–106.

Sun Z., Renfro N.D., Palke A.C., Breitzmann H., Muyal J., Hand D., Hain M., McClure S.F., Katsurada Y., Miura M., Rossman G.R. (2020) Gem News International: Sunstone plagioclase feldspar from Ethiopia. *G&G*, Vol. 56, No. 1, pp. 184–188.

Tan T.L., Wong D., Lee P. (2004) Iridescence of a shell of mollusk *Haliotis Glabra*. *Optics Express*, Vol. 12, No. 20, pp. 4847–4854, http://dx.doi.org/10.1364/OPEX.12.004847

Tschauner O., Ma C., Lanzirotti A., Newville M.G. (2020) Riesite, a new high pressure polymorph of TiO_2 from the Ries impact structure. *Minerals*, Vol. 10, No. 1, article no. 78, http://dx.doi.org/10.3390/min10010078

Tschauner O., Navon O., Schmidt C. (2022) Deltanitrogen, IMA 2019-067b. In *CNMNC Newsletter 69, European Journal of Mineralogy*, Vol. 34, No. 5, p. 467, http://dx.doi.org/10.5194/Ejm-34-463-2022

Tutton A.E.H. (1921) The structure of adularia and moonstone. *Nature*, Vol. 108, No. 2715, pp. 352–353, http://dx.doi.org/10.1038/108352a0

van Roermund H.L.M., Drury M.R., Barnhoorn A., De Ronde A. (2000) Non-silicate inclusions in garnet from an ultra-deep orogenic peridotite. *Geological Journal*, Vol. 35, No. 3-4, pp. 209–229, http://dx.doi.org/10.1002/gj.858

Vaughan D.J., Tossell J.A., Stanley C.J. (1987) The surface properties of bornite. *Mineralogical Magazine*, Vol. 51, No. 360, pp. 285–293, http://dx.doi.org/10.1180/minmag.1987.051.360.11

Vertriest W., Bruce-Lockhart S. (2018) Gem News International: Twelve-rayed star sapphire from Thailand. *G&G*, Vol. 54, No. 2, p. 238.

Viti C., Ferrari M. (2006) The nature of Ti-rich inclusions responsible for asterism in Verneuil-grown corundums. *European Journal of Mineralogy*, Vol. 18, No. 6, pp. 823–834, http://dx.doi.org/10.1127/0935-1221/2006/0018-0823

von Vultée J. (1955) Über die orientierten Verwachsungen von Rutil in Quarz. *Neues Jahrbuch für Mineralogie Abhandlungen*, Vol. 87, No. 3, pp. 389–415.

——— (1956) Die Verwachsungsgesetze der orientierten Einlagerungen von Rutil in Quarz. *Zeitschrift für Kristallographie*, Vol. 107, No. 1-2, pp. 1–17, http://dx.doi.org/10.1524/zkri.1956.107.1-2.1

Walcott A.J. (1937) Asterism in garnet, spinel, quartz and sapphire. *Geological Series of Field Museum of Natural History*, Vol 7, No. 3, pp. 39–57.

Wang C., Shen A.H., Heaney P.J., Palke A., Wang K., Wang H., Kiefert L. (2025) Cu nanoparticle geometry as the key to bicolor behavior in Oregon sunstones: An application of LSPR theory in nanomineralogy. *American Mineralogist*, Vol. 110, No. 2, pp. 293–305, http://dx.doi.org/10.2138/am-2023-9141

Wang C.-M., Thevuthasan S., Gao F., McCready D.E., Chambers S.A. (2002) The characteristics of interface misfit dislocations for epitaxial α-Fe_2O_3 on α-Al_2O_3(0001). *Thin Solid Films*, Vol. 414, No. 1, pp. 31–38, http://dx.doi.org/10.1016/S0040-6090(02)00452-2

Watts E.A. (2021) Lab Notes: Asterism in natural diamond cabochons. *G&G*, Vol. 57, No. 1, pp. 52–53.

Weibel M., Wessicken R. (1981) Haemetit als Einschluss im schwarzen Sternsaphir. *Gemmologie: Zeitschrift der Deutschen Gemmologischen Gesellschaft*, Vol. 30, No. 3-4, pp. 170–176.

Weibel M., Wessicken R., Woensdregt C.F., Wüthrich A. (1980) Sternsaphir und sternquarz. *Schweizerische Mineralogische und Petrographische Mitteilungen*, Vol. 60, No. 2-3, pp. 133–136, http://dx.doi.org/10.5169/seals-46663

Weidlich A., Wilkie A. (2009) Rendering the effect of labradorescence. In *Proceedings of Graphics Interface 2009*, Canadian Information Processing Society, pp. 79–85.

White J.S. (2015) Mineral mysteries: Star rose quartz. *Rocks & Minerals*, Vol. 90, No. 3, pp. 282–284, http://dx.doi.org/10.1080/00357529.2015.1012960

Wibel F. (1873) Der faserquarz vom Cap - Eine pseudomorphose nach krokydolith. *Neues Jahrbuch für Mineralogie, Geologie und Palaeontologie*, pp. 367–380.

Win W.L., Moe K.S. (2012) Gem News International: Rainbow moonstone from Zambia. *G&G*, Vol. 48, No. 2, pp. 146–147.

Woensdregt C.F., Weibel M., Wessicken R. (1980) Star quartz asterism caused by sillimanite. *Schweizerische Mineralogische und Petrographische Mitteilungen*, Vol. 60, No. 2-3, pp. 129–132, http://dx.doi.org/10.5169/SEALS-46662

Wüthrich A., Weibel M. (1981) Optical theory of asterism. *Physics and Chemistry of Minerals*, Vol. 7, No. 1, pp. 53–54, http://dx.doi.org/10.1007/BF00308202

Wüthrich A., Weibel M., Gübelin E.J. (1983) Elucidating the optical theory of chatoyancy and asterism. *Australian Gemmologist*, Vol. 15, No. 1, pp. 3–6.

Xiao S.Q., Dahmen U., Heuer A.H. (1997) Phase transformation of TiO_2 precipitates in sapphire (α-Al_2O_3) induced by the loss of coherency. *Philosophical Magazine A*, Vol. 75, No. 1, pp. 221–238, http://dx.doi.org/10.1080/01418619708210292

Xu H., Hill T.R., Konishi H., Farfan G. (2017) Protoenstatite: A new mineral in Oregon sunstones with "watermelon" colors. *American Mineralogist*, Vol. 102, No. 10, pp. 2146–2149, http://dx.doi.org/10.2138/am-2017-6186

Xu H., Jin S., Lee S., Brown P.E. (2023) Cation ordering, twinning, and pseudo-symmetry in silicate garnet: The study of a birefringent garnet with orthorhombic structure. *American Mineralogist*, Vol. 108, No. 3, pp. 572–583, http://dx.doi.org/10.2138/am-2022-8455

Xu H.J., Wu Y. (2017) Oriented inclusions of pyroxene, amphibole and rutile in garnet from the Lüliangshan garnet peridotite massif, North Qaidam UHPM belt, NW China: An electron backscatter diffraction study. *Journal of Metamorphic Geology*, Vol. 35, No. 1, pp. 1–17, http://dx.doi.org/10.1111/jmg.12208

Yang J., Chen Q., Xu F., Li Y., Liu X. (2023) Gem News Interna-

tional: A newly discovered iridescent andradite from Inner Mongolia, China. *G&G*, Vol. 59, No. 3, pp. 391–394.
Ye X., Qiu Z., Chen C., Zhang Y. (2021) Nondestructive identification of mineral inclusions by Raman mapping: Micro-magnetite inclusions in iridescent scapolite as example. *Spectroscopy and Spectral Analysis*, Vol. 41, No. 7, pp. 2105–2109.
Yund R.A. (1983) Microstructure, kinetics and mechanisms of alkali feldspar exsolution. In P.H. Ribbe, Ed., *Feldspar Mineralogy*. Mineralogical Society of America, Washington, D.C., pp. 177–202, http://dx.doi.org/10.1515/9781501508547-012
——— (1984) Alkali feldspar exsolution: Kinetics and dependence on alkali interdiffusion. In W.L. Brown, Ed., *Feldspars and Feldspathoids: Structures, Properties and Occurrences*, NATO ASI Series. Springer Netherlands, Dordrecht, pp. 281–315, http://dx.doi.org/10.1007/978-94-015-6929-3_8
Zhang J.F., Xu H.J., Liu Q., Green II H.W., Dobrzhinetskaya L.F. (2011) Pyroxene exsolution topotaxy in majoritic garnet from 250 to 300 km depth. *Journal of Metamorphic Geology*, Vol. 29, No. 7, pp. 741–751, http://dx.doi.org/10.1111/j.1525-1314.2011.00939.x
Zhao Q., Zhao S., Xu C. (2022) Hematite exsolutions in corundum from Cenozoic basalts in Changle, Shandong Province, China: Crystallographic orientation relationships and interface characters. *Crystals*, Vol. 12, No. 7, article no. 905, http://dx.doi.org/10.3390/cryst12070905
Zhou Q., Wang C., Shen A.H. (2021) Copper nanoparticles embedded in natural plagioclase mineral crystals: In situ formation and third-order nonlinearity. *Journal of Physical Chemistry C*, Vol. 126, No. 1, pp. 387–395, http://dx.doi.org/10.1021/acs.jpcc.1c09145
Zhou Q., Wang C., Shen A.-H. (2022) Application of high-temperature copper diffusion in surface recoloring of faceted labradorites. *Minerals*, Vol. 12, No. 8, article no. 920, http://dx.doi.org/10.3390/min12080920